Supplementary Materials

Extended Discussion

Extended discussion of candidate loci for positive selection

Recent positive selection in bonobos

In bonobos, the GO category "involved_in sensory perception of sound" shows a significant enrichment in the XP-EHH-based test (Table 1). Bonobos are known for their high-pitched calls, compared to chimpanzees [1], with their inner-ear bone morphology being different from both humans and chimpanzees [2], which might be associated with this finding. Although not passing multiple testing correction, "acts_upstream_of_or_within vocal learning" was also among the significant categories for bonobos (Additional File 2: Table S22), which has to do with auditory ability. Two genes, *MCC*, which is overexpressed in ovary, and *SHROOM3* have been previously described as candidates for this species in multiple studies [3, 4]. A protein-coding change (Additional File 2: Table S3) in the *KHNYN* gene might be associated with immune function [5], as well as another change in *ERAP2* for recent selection [6].

One of the candidate loci with the highest XP-EHH scores in bonobos (Additional File 2: Table S3) might be related to reproduction traits, falling near *DPP10*[7], which is associated to age at menarche in humans and found across all four comparisons involving bonobos (Additional File 2: Table S10). The gene *MRPS11*, associated with the onset of male puberty [8], carries another protein-coding change. *ZNF804A* carries five protein-coding changes in bonobos with a signature of positive selection. This gene is overexpressed in brain regions including hypothalamus, anterior cingulate cortex and nucleus accumbens, and might have neurological functions [9].

A locus near *LRP1B* is found as a candidate for selection (XP-EHH) across all four chimpanzee subspecies tests, a gene which has been previously described as a candidate for reproduction-related bonobo-specific traits [10]. Genes related to the specific biology of bonobos might also be suggested by the categories "involved_in negative regulation of determination of dorsal identity" and "acts_upstream_of_or_within dorsal/ventral pattern formation" (nominally enriched, Additional File 2: Table S22), which could potentially be related to the characteristic ventro-ventral copulation of bonobos based on their anatomical features [11, 12].

Recent positive selection in chimpanzees

In contrast, no GO categories reached significance in the chimpanzee lineage as a whole. Loci with the highest XP-EHH scores (Additional File 2: Table S3) in chimpanzees are possibly involved in hearing loss (*SLC26A4* [13]), or innate immunity (*BIRC2* [14]). Protein-coding changes are found in genes related to various functions such as immune response (*CLECL1* [15] , *MS4A2* [16]), brain development (*KDM7A* [17]), or cell division (*CPAP* [18], *CENPN* [19]). A previously described candidate gene [20] is also involved in spermatogenesis (*CDYL* [21]).

Recurrently supported targets of positive selection [3, 4, 20, 22] are *APBB2*, which might be involved in neuron development [23], and *FAF1* with functions including virus response [24]. However, given the divergence times of chimpanzee subspecies, the methods applied here might be more informative on the subspecies level, in particular for cross-population analyzes of positive selection.

Recent positive selection in chimpanzee subspecies

The only significant GO category in chimpanzees (Table 1) is for the immunity-related category "involved_in negative regulation of CD8-positive, alpha-beta T cell proliferation" in Nigeria-Cameroon chimpanzees, suggesting recent selective pressures in immune response. A variant in *FUT9*, a gene associated with susceptibility to placental malaria infection [25], shows signatures of selection in comparison to bonobos as well as Nigeria-Cameroon chimpanzees, which is interesting given previously described patterns of selection on malaria in this subspecies [26].

In both western and central chimpanzee subspecies, suggestive evidence for selection on immunity is reflected by various MHC-related categories (Additional File 2: Table S25, nominally enriched). A top candidate locus in western chimpanzees in *SULT1C3* is in a gene involved in xenobiotic metabolic processes [27], which might reflect selection pressures related to novel environments during recent population expansions of this subspecies [28]. A protein-coding change under selection in *NPHS1* might be due to kidney functions of filtering plasma macromolecules [29].

A top candidate locus in central chimpanzees falls in the *EFCAB6* gene, which regulates the androgen receptor and may play a role in spermatogenesis [30], a trait with known differences between great ape species [31]. This subspecies also carries a protein-coding change at a candidate locus (XP-EHH) in *SHOC1*, a gene for which mutations cause azoospermia in humans and mice [32]. Further non-synonymous mutations in *ADAD2*, *CFAP70* or *SUN1* (XP-nSL) might also indicate lineage-specific selection on spermatogenesis [33–35]. Among genes recurrently found across studies [4, 22] are *CENPP*, a spindle protein required for cell division [36], and *CORIN*, which might play a role in female fertility by promoting trophoblast invasion [37].

Protein-coding changes under selection in eastern chimpanzees (XP-EHH) encompass olfactory receptors (*OR2B6*, *OR2B2*), or a bile acid transporter (*SLC51B* [38]) which might be related to dietary adaptation. Other such changes (XP-nSL) occur in genes related to male fertility (*CFAP70* [39], *MOV10L1* [40]). A recurrently found target gene in this subspecies [3, 4, 22] is *GLG1*, a gene which is predicted to

enable fibroblast growth factor binding [41], potentially influencing processes such as chondrocyte differentiation.

Recent positive selection in western gorillas

In western gorillas, a GO category related to response to stilbenoid reached significance using the conservative threshold (0.005%) for the XP-nSL test (Additional File 2: Table S21). Stilbenoids belong to phenolic compounds found in many plant species [42], some of which western gorillas might be able to particularly exploit [43]. Multiple further GO categories related to cholesterol, steroid or lipid metabolism are nominally enriched (Additional File 2: Table S21), which might be related to their dietary components. In contrast, nominally enriched categories associated with the immune system in eastern gorillas (Additional File 2: Table S20) might reflect their history of response to pathogen infections.

Recent positive selection in eastern gorillas

Notably, three out of the seven significant GO categories across lineages and tests were observed in mountain gorillas (Table 1), which might be associated with their unique adaptation to high altitude with a heavily leave-based diet. Two keratin- and intermediate filament-related categories (XP-EHH) are likely linked to their thick hair, and a pantetheine-related category (XP-nSL) is potentially associated with energy metabolism. One gene from this category is among the top 5 scores for mountain gorillas (*KRTAP25-1*) and carries a non-synonymous mutation in mountain gorillas (Ser70Cys, XP-EHH). Moreover, four non-synonymous mutations with a selection signature are observed in *KRTAP27-1*, two in *KRTAP24-1* and one in *KRTAP23-1*.

Apart from those, only two more non-synonymous mutations show a signature of selection in mountain gorillas, both in *VNN1*, a gene upregulated in high-altitude pulmonary hypertension patients, likely due to a role in oxidative stress regulation under hypoxic conditions [44]. Another non-synonymous change in *FN1* (XP-nSL) might potentially have played a role in altitude adaptation as well [45].

Other top candidate loci are in *EDNRB-AS1*, associated to the ABCD syndrome which entails pigmentation and intestinal phenotypes [46], or *MYRIP*, which might regulate insulin secretion [47]. A previously described candidate gene [48] confirmed here is the lipoprotein lipase-coding gene *LPL*, involved in lipid metabolism, hence also potentially involved in pathways related to altitude adaptation [49].

Recent positive selection in Bornean orangutans

Genes under positive selection in Bornean orangutans are nominally enriched for the GO category "involved_in positive regulation of behavioral fear response" (adjusted p-value 0.053, Additional File 2: Table S17, XP-nSL). This is interesting, as Bornean orangutans are known to be less social compared to Sumatran orangutans [50, 51], given that orangutans in general are considered solitary. Furthermore, Bornean Orangutans experienced a more recent decline due to human impact [52].

Non-synonymous mutations putatively under selection in Bornean orangutans occur in the collagen-encoding gene *COL11A1*, which might possibly be related to

differences in hair and skin morphology [53], and in *MGAM*, encoding for a starch digestion-related enzyme that might relate to differences in diet between Orangutan species [54].

Recent positive selection in Sumatran orangutans

In Sumatran orangutans, the GO category "involved_in negative regulation of endocytosis" is enriched for genes under selection (XP-EHH, 0.005% threshold). Being a fundamental cellular process, this could be related to various biological traits, including immune response [55]. Among top candidate loci in this species, we find *COX19*, which is overexpressed in heart and possibly related to cardiomyopathy, which is interesting considering the high prevalence of cardiovascular lesions in captive orangutans [56]. As described above, *NRXN3* has been found as target of selection in humans, while it has been previously described for Sumatran orangutans as well [57].

References

[1] Waal, F.B.M.D.: The Communicative Repertoire of Captive Bonobos (Pan Paniscus), Compared To That of Chimpanzees. Behaviour **106**(3-4), 183–251 (1988) https://doi.org/10.1163/156853988X00269

[2] Stoessel, A., David, R., Bornitz, M., Ossmann, S., Neudert, M.: Auditory thresholds compatible with optimal speech reception likely evolved before the human-chimpanzee split. Scientific Reports **13**(1), 20732 (2023) https://doi.org/10.1038/s41598-023-47778-2

[3] Cagan, A., Theunert, C., Laayouni, H., Santpere, G., Pybus, M., Casals, F., Prüfer, K., Navarro, A., Marques-Bonet, T., Bertranpetit, J., Andres, A.M.: Natural Selection in the Great Apes. Molecular Biology and Evolution **33**(12), 3268–3283 (2016) https://doi.org/10.1093/molbev/msw215

[4] Yoo, D., Rhie, A., Hebbar, P., Antonacci, F., Logsdon, G.A., Solar, S.J., Antipov, D., Pickett, B.D., Safonova, Y., Montinaro, F., Luo, Y., Malukiewicz, J., Storer, J.M., Lin, J., Sequeira, A.N., Mangan, R.J., Hickey, G., Monfort Anez, G., Balachandran, P., Bankevich, A., Beck, C.R., Biddanda, A., Borchers, M., Bouffard, G.G., Brannan, E., Brooks, S.Y., Carbone, L., Carrel, L., Chan, A.P., Crawford, J., Diekhans, M., Engelbrecht, E., Feschotte, C., Formenti, G., Garcia, G.H., Gennaro, L., Gilbert, D., Green, R.E., Guarracino, A., Gupta, I., Haddad, D., Han, J., Harris, R.S., Hartley, G.A., Harvey, W.T., Hiller, M., Hoekzema, K., Houck, M.L., Jeong, H., Kamali, K., Kellis, M., Kille, B., Lee, C., Lee, Y., Lees, W., Lewis, A.P., Li, Q., Loftus, M., Loh, Y.H.E., Loucks, H., Ma, J., Mao, Y., Martinez, J.F.I., Masterson, P., McCoy, R.C., McGrath, B., McKinney, S., Meyer, B.S., Miga, K.H., Mohanty, S.K., Munson, K.M., Pal, K., Pennell, M., Pevzner, P.A., Porubsky, D., Potapova, T., Ringeling, F.R., Rocha, J.L., Ryder, O.A., Sacco, S., Saha, S., Sasaki, T., Schatz, M.C., Schork, N.J., Shanks, C., Smeds, L., Son, D.R., Steiner, C., Sweeten, A.P., Tassia, M.G., Thibaud-Nissen, F., Torres-González, E., Trivedi, M., Wei, W., Wertz, J., Yang, M., Zhang, P., Zhang, S.,

Zhang, Y., Zhang, Z., Zhao, S.A., Zhu, Y., Jarvis, E.D., Gerton, J.L., Rivas-González, I., Paten, B., Szpiech, Z.A., Huber, C.D., Lenz, T.L., Konkel, M.K., Yi, S.V., Canzar, S., Watson, C.T., Sudmant, P.H., Molloy, E., Garrison, E., Lowe, C.B., Ventura, M., O'Neill, R.J., Koren, S., Makova, K.D., Phillippy, A.M., Eichler, E.E.: Complete sequencing of ape genomes. Nature **641**(8062), 401–418 (2025) https://doi.org/10.1038/s41586-025-08816-3

[5] Ficarelli, M., Wilson, H., Pedro Galão, R., Mazzon, M., Antzin-Anduetza, I., Marsh, M., Neil, S.J.D., Swanson, C.M.: KHNYN is essential for the zinc finger antiviral protein (ZAP) to restrict HIV-1 containing clustered CpG dinucleotides. eLife **8**, 46767 (2019) https://doi.org/10.7554/eLife.46767

[6] Saulle, I., Marventano, I., Saresella, M., Vanetti, C., Garziano, M., Fenizia, C., Trabattoni, D., Clerici, M., Biasin, M.: ERAPs Reduce In Vitro HIV Infection by Activating Innate Immune Response. The Journal of Immunology **206**(7), 1609–1617 (2021) https://doi.org/10.4049/jimmunol.2000991

[7] Feng, G.-J., Xu, Q., Zhao, Q.-G., Han, B.-X., Yan, S.-S., Zhu, J., Pei, Y.-F.: The genetic architecture of age at menarche and its causal effects on other traits. Journal of Human Genetics **69**(12), 645–653 (2024) https://doi.org/10.1038/s10038-024-01287-w

[8] Hollis, B., Day, F.R., Busch, A.S., Thompson, D.J., Soares, A.L.G., Timmers, P.R.H.J., Kwong, A., Easton, D.F., Joshi, P.K., Timpson, N.J., Eeles, R.A., Henderson, B.E., Haiman, C.A., Kote-Jarai, Z., Schumacher, F.R., Olama, A.A.A., Benlloch, S., Muir, K., Berndt, S.I., Conti, D.V., Wiklund, F., Chanock, S., Gapstur, S., Stevens, V.L., Tangen, C.M., Batra, J., Clements, J., Tilley, W., Risbridger, G.P., Clements, J., Horvath, L., Taylor, R., Hayes, V., Butler, L., Yeadon, T., Eckert, A., Saunders, P., Haynes, A.-M., Papargiris, M., Srinivasan, S., Kedda, M.-A., Moya, L., Batra, J., Gronberg, H., Pashayan, N., Schleutker, J., Albanes, D., Wolk, A., West, C., Mucci, L., Cancel-Tassin, G., Koutros, S., Sorensen, K.D., Grindedal, E.M., Neal, D.E., Hamdy, F.C., Donovan, J.L., Travis, R.C., Hamilton, R.J., Ingles, S.A., Rosenstein, B.S., Lu, Y.-J., Giles, G.G., Kibel, A.S., Vega, A., Kogevinas, M., Penney, K.L., Park, J.Y., Stanford, J.L., Cybulski, C., Nordestgaard, B.G., Brenner, H., Maier, C., Kim, J., John, E.M., Teixeira, M.R., Neuhausen, S.L., De Ruyck, K., Razack, A., Newcomb, L.F., Lessel, D., Kaneva, R., Usmani, N., Claessens, F., Townsend, P.A., Gago-Dominguez, M., Roobol, M.J., Menegaux, F., Khaw, K.-T., Cannon-Albright, L., Pandha, H., Thibodeau, S.N., Agee, M., Alipanahi, B., Auton, A., Bell, R.K., Bryc, K., Elson, S.L., Fontanillas, P., Furlotte, N.A., Hinds, D.A., Huber, K.E., Kleinman, A., Litterman, N.K., McIntyre, M.H., Mountain, J.L., Noblin, E.S., Northover, C.A.M., Pitts, S.J., Sathirapongsasuti, J.F., Sazonova, O.V., Shelton, J.F., Shringarpure, S., Tian, C., Tung, J.Y., Vacic, V., Wilson, C.H., Ong, K.K., Perry, J.R.B., Consortium, T.P., (APCB), A.P.C.B., Team, a.R.: Genomic analysis of male puberty timing highlights shared genetic basis with hair colour and lifespan. Nature Communications **11**(1), 1536 (2020)

https://doi.org/10.1038/s41467-020-14451-5

[9] Kushima, I., Aleksic, B., Nakatochi, M., Shimamura, T., Okada, T., Uno, Y., Morikawa, M., Ishizuka, K., Shiino, T., Kimura, H., Arioka, Y., Yoshimi, A., Takasaki, Y., Yu, Y., Nakamura, Y., Yamamoto, M., Iidaka, T., Iritani, S., Inada, T., Ogawa, N., Shishido, E., Torii, Y., Kawano, N., Omura, Y., Yoshikawa, T., Uchiyama, T., Yamamoto, T., Ikeda, M., Hashimoto, R., Yamamori, H., Yasuda, Y., Someya, T., Watanabe, Y., Egawa, J., Nunokawa, A., Itokawa, M., Arai, M., Miyashita, M., Kobori, A., Suzuki, M., Takahashi, T., Usami, M., Kodaira, M., Watanabe, K., Sasaki, T., Kuwabara, H., Tochigi, M., Nishimura, F., Yamasue, H., Eriguchi, Y., Benner, S., Kojima, M., Yassin, W., Munesue, T., Yokoyama, S., Kimura, R., Funabiki, Y., Kosaka, H., Ishitobi, M., Ohmori, T., Numata, S., Yoshikawa, T., Toyota, T., Yamakawa, K., Suzuki, T., Inoue, Y., Nakaoka, K., Goto, Y.-i., Inagaki, M., Hashimoto, N., Kusumi, I., Son, S., Murai, T., Ikegame, T., Okada, N., Kasai, K., Kunimoto, S., Mori, D., Iwata, N., Ozaki, N.: Comparative Analyses of Copy-Number Variation in Autism Spectrum Disorder and Schizophrenia Reveal Etiological Overlap and Biological Insights. Cell Reports **24**(11), 2838–2856 (2018) https://doi.org/10.1016/j.celrep.2018.08.022

[10] Han, S., Andrés, A.M., Marques-Bonet, T., Kuhlwilm, M.: Genetic variation in Pan species is shaped by demographic history and harbors lineage-specific functions. Genome Biology and Evolution, 047 (2019) https://doi.org/10.1093/gbe/evz047

[11] Blount, B.G.: Issues in Bonobo (Pan paniscus) Sexual Behavior. American Anthropologist **92**(3), 702–714 (1990) https://doi.org/10.1525/aa.1990.92.3.02a00100

[12] Dahl, J.F.: The external genitalia of female pygmy chimpanzees. The Anatomical Record **211**(1), 24–28 (1985) https://doi.org/10.1002/ar.1092110105

[13] Pourová, R., Janoušek, P., Jurovčík, M., Dvořáková, M., Malíková, M., Rašková, D., Bendová, O., Leonardi, E., Murgia, A., Kabelka, Z., Astl, J., Seeman, P.: Spectrum and Frequency of SLC26A4 Mutations Among Czech Patients with Early Hearing Loss with and without Enlarged Vestibular Aqueduct (EVA). Annals of Human Genetics **74**(4), 299–307 (2010) https://doi.org/10.1111/j.1469-1809.2010.00581.x

[14] Bertrand, M.J.M., Doiron, K., Labbé, K., Korneluk, R.G., Barker, P.A., Saleh, M.: Cellular Inhibitors of Apoptosis cIAP1 and cIAP2 Are Required for Innate Immunity Signaling by the Pattern Recognition Receptors NOD1 and NOD2. Immunity **30**(6), 789–801 (2009) https://doi.org/10.1016/j.immuni.2009.04.011

[15] Ryan, E.J., Marshall, A.J., Magaletti, D., Floyd, H., Draves, K.E., Olson, N.E., Clark, E.A.: Dendritic Cell-Associated Lectin-1: A Novel Dendritic Cell-Associated, C-Type Lectin-Like Molecule Enhances T Cell Secretion of IL-41. The Journal of Immunology **169**(10), 5638–5648 (2002) https://doi.org/10.4049/

jimmunol.169.10.5638

[16] Hill, M.R., Cookson, W.O.C.M.: A New Variant of the β Subunit of the High-Affinity Receptor for Immunoglobulin E (FcϵRI-β E237G): Associations with Measures of Atopy and Bronchial Hyper-Responsiveness. Human Molecular Genetics **5**(7), 959–962 (1996) https://doi.org/10.1093/hmg/5.7.959

[17] Tsukada, Y.-i., Ishitani, T., Nakayama, K.I.: KDM7 is a dual demethylase for histone H3 Lys 9 and Lys 27 and functions in brain development. Genes & Development **24**(5), 432–437 (2010) https://doi.org/10.1101/gad.1864410

[18] Kleylein-Sohn, J., Westendorf, J., Le Clech, M., Habedanck, R., Stierhof, Y.-D., Nigg, E.A.: Plk4-Induced Centriole Biogenesis in Human Cells. Developmental Cell **13**(2), 190–202 (2007) https://doi.org/10.1016/j.devcel.2007.07.002

[19] Carroll, C.W., Silva, M.C.C., Godek, K.M., Jansen, L.E.T., Straight, A.F.: Centromere assembly requires the direct recognition of CENP-A nucleosomes by CENP-N. Nature Cell Biology **11**(7), 896–902 (2009) https://doi.org/10.1038/ncb1899

[20] Zhao, S., Chi, L., Chen, H.: CEGA: a method for inferring natural selection by comparative population genomic analysis across species. Genome Biology **24**(1), 219 (2023) https://doi.org/10.1186/s13059-023-03068-8

[21] Lan, K.-C., Cheng, Y.-H., Chang, Y.-C., Wei, K.-T., Weng, P.-L., Kang, H.-Y.: Interaction between Chromodomain Y-like Protein and Androgen Receptor Signaling in Sertoli Cells Accounts for Spermatogenesis (2024). https://doi.org/10.3390/cells13100851

[22] Nye, J., Mondal, M., Bertranpetit, J., Laayouni, H.: A fully integrated machine learning scan of selection in the chimpanzee genome. NAR Genomics and Bioinformatics **2**(3), 061 (2020) https://doi.org/10.1093/nargab/lqaa061

[23] Haenig, C., Atias, N., Taylor, A.K., Mazza, A., Schaefer, M.H., Russ, J., Riechers, S.-P., Jain, S., Coughlin, M., Fontaine, J.-F., Freibaum, B.D., Brusendorf, L., Zenkner, M., Porras, P., Stroedicke, M., Schnoegl, S., Arnsburg, K., Boeddrich, A., Pigazzini, L., Heutink, P., Taylor, J.P., Kirstein, J., Andrade-Navarro, M.A., Sharan, R., Wanker, E.E.: Interactome Mapping Provides a Network of Neurodegenerative Disease Proteins and Uncovers Widespread Protein Aggregation in Affected Brains. Cell Reports **32**(7) (2020) https://doi.org/10.1016/j.celrep.2020.108050

[24] Dai, T., Wu, L., Wang, S., Wang, J., Xie, F., Zhang, Z., Fang, X., Li, J., Fang, P., Li, F., Jin, K., Dai, J., Yang, B., Zhou, F., Dam, H., Cai, D., Huang, H., Zhang, L.: FAF1 Regulates Antiviral Immunity by Inhibiting MAVS but Is Antagonized by Phosphorylation upon Viral Infection. Cell Host & Microbe **24**(6), 776–790 (2018) https://doi.org/10.1016/j.chom.2018.10.006

[25] Sikora, M., Ferrer-Admetlla, A., Laayouni, H., Menendez, C., Mayor, A., Bardaji, A., Sigauque, B., Mandomando, I., Alonso, P.L., Bertranpetit, J., Casals, F.: A variant in the gene FUT9 is associated with susceptibility to placental malaria infection. Human Molecular Genetics **18**(16), 3136–3144 (2009) https://doi.org/10.1093/hmg/ddp240

[26] Ostridge, H.J., Fontsere, C., Lizano, E., Soto, D.C., Schmidt, J.M., Saxena, V., Alvarez-Estape, M., Barratt, C.D., Gratton, P., Bocksberger, G., Lester, J.D., Dieguez, P., Agbor, A., Angedakin, S., Assumang, A.K., Bailey, E., Barubiyo, D., Bessone, M., Brazzola, G., Chancellor, R., Cohen, H., Coupland, ., Danquah, E., Deschner, T., Dotras, L., Dupain, J., Egbe, V.E., Granjon, A.-C., Head, J., Hedwig, D., Hermans, V., Hernandez-Aguilar, R.A., Jeffery, K.J., Jones, S., Junker, J., Kadam, P., Kaiser, M., Kalan, A.K., Kambere, M., Kienast, I., Kujirakwinja, D., Langergraber, K.E., Lapuente, J., Larson, B., Laudisoit, A., Lee, K.C., Llana, M., Maretti, G., Martín, R., Meier, A.C., Morgan, D., Neil, E., Nicholl, S., Nixon, S., Normand, E., Orbell, C., Ormsby, L.J., Orume, R., Pacheco, L., Preece, J., Regnaut, S., Robbins, M.M., Rundus, A., Sanz, C., Sciaky, L., Sommer, V., Stewart, F.A., Tagg, N., Tédonzong, L.R., Schijndel, J., Vendras, E., Wessling, E.G., Willie, J., Wittig, R.M., Yuh, Y.G., Yurkiw, K., Vigilant, L., Piel, A.K., Boesch, C., Kühl, H.S., Dennis, M.Y., Marques-Bonet, T., Arandjelovic, M., Andrés, A.M.: Local genetic adaptation to habitat in wild chimpanzees. Science **387**(6730), 7954 (2025) https://doi.org/10.1126/science.adn7954

[27] Kurogi, K., Shimohira, T., Kouriki-Nagatomo, H., Zhang, G., Miller, E.R., Sakakibara, Y., Suiko, M., Liu, M.-C.: Human Cytosolic Sulphotransferase SULT1C3: genomic analysis and functional characterization of splice variant SULT1C3a and SULT1C3d. The Journal of Biochemistry **162**(6), 403–414 (2017) https://doi.org/10.1093/jb/mvx044

[28] Fontsere, C., Kuhlwilm, M., Morcillo-Suarez, C., Alvarez-Estape, M., Lester, J.D., Gratton, P., Schmidt, J.M., Dieguez, P., Aebischer, T., Álvarez-Varona, P., Agbor, A., Angedakin, S., Assumang, A.K., Ayimisin, E.A., Bailey, E., Barubiyo, D., Bessone, M., Carretero-Alonso, A., Chancellor, R., Cohen, H., Danquah, E., Deschner, T., Dunn, A., Dupain, J., Egbe, V.E., Feliu, O., Goedmakers, A., Granjon, A.-C., Head, J., Hedwig, D., Hermans, V., Hernandez-Aguilar, R.A., Imong, I., Jones, S., Junker, J., Kadam, P., Kaiser, M., Kambere, M., Kambale, M.V., Kalan, A.K., Kienast, I., Kujirakwinja, D., Langergraber, K., Lapuente, J., Larson, B., Laudisoit, A., Lee, K., Llana, M., Llorente, M., Marrocoli, S., Morgan, D., Mulindahabi, F., Murai, M., Neil, E., Nicholl, S., Nixon, S., Normand, E., Orbell, C., Ormsby, L.J., Pacheco, L., Piel, A., Riera, L., Robbins, M.M., Rundus, A., Sanz, C., Sciaky, L., Sommer, V., Stewart, F.A., Tagg, N., Tédonzong, L.R., Ton, E., Schijndel, J., Vergnes, V., Wessling, E.G., Willie, J., Wittig, R.M., Yuh, Y.G., Yurkiw, K., Zuberbuehler, K., Hecht, J., Vigilant, L., Boesch, C., Andrés, A.M., Hughes, D.A., Kühl, H.S., Lizano, E., Arandjelovic, M., Marques-Bonet, T.: Population dynamics and genetic connectivity in recent chimpanzee history. Cell Genomics **2**(6) (2022) https://doi.org/10.1016/j.xgen.2022.100133

[29] Ruotsalainen, V., Ljungberg, P., Wartiovaara, J., Lenkkeri, U., Kestilä, M., Jalanko, H., Holmberg, C., Tryggvason, K.: Nephrin is specifically located at the slit diaphragm of glomerular podocytes. Proceedings of the National Academy of Sciences **96**(14), 7962–7967 (1999) https://doi.org/10.1073/pnas.96.14.7962

[30] Niki, T., Takahashi-Niki, K., Taira, T., Iguchi-Ariga, S.M.M., Ariga, H.: DJBP: A Novel DJ-1-Binding Protein, Negatively Regulates the Androgen Receptor by Recruiting Histone Deacetylase Complex, and DJ-1 Antagonizes This Inhibition by Abrogation of This Complex. Molecular Cancer Research **1**(4), 247–261 (2003)

[31] Anderson, M.J., Dixson, A.F.: Motility and the midpiece in primates. Nature **416**(6880), 496 (2002) https://doi.org/10.1038/416496a

[32] Wang, W., Meng, L., He, J., Su, L., Li, Y., Tan, C., Xu, X., Nie, H., Zhang, H., Du, J., Lu, G., Luo, M., Lin, G., Tu, C., Tan, Y.-Q.: Bi-allelic variants in SHOC1 cause non-obstructive azoospermia with meiosis arrest in humans and mice. Molecular Human Reproduction **28**(6), 015 (2022) https://doi.org/10.1093/molehr/gaac015

[33] Shi, B., Shah, W., Liu, L., Gong, C., Zhou, J., Abbas, T., Ma, H., Zhang, H., Yang, M., Zhang, Y., Ullah, N., Mahammad, Z., Khan, M., Murtaza, G., Ali, A., Khan, R., Sha, J., Yuan, Y., Shi, Q.: Biallelic mutations in RNA-binding protein ADAD2 cause spermiogenic failure and non-obstructive azoospermia in humans. Human Reproduction Open **2023**(3), 022 (2023) https://doi.org/10.1093/hropen/hoad022

[34] Dacheux, D., Martinez, G., Broster Reix, C.E., Beurois, J., Lores, P., Tounkara, M., Dupuy, J.-W., Robinson, D.R., Loeuillet, C., Lambert, E., Wehbe, Z., Escoffier, J., Amiri-Yekta, A., Daneshipour, A., Hosseini, S.-H., Zouari, R., Mustapha, S.F.B., Halouani, L., Jiang, X., Shen, Y., Liu, C., Thierry-Mieg, N., Septier, A., Bidart, M., Satre, V., Cazin, C., Kherraf, Z.E., Arnoult, C., Ray, P.F., Toure, A., Bonhivers, M., Coutton, C.: Novel axonemal protein ZMYND12 interacts with TTC29 and DNAH1, and is required for male fertility and flagellum function. eLife **12**, 87698 (2023) https://doi.org/10.7554/eLife.87698

[35] Meng, Q., Shao, B., Zhao, D., Fu, X., Wang, J., Li, H., Zhou, Q., Gao, T.: Loss of SUN1 function in spermatocytes disrupts the attachment of telomeres to the nuclear envelope and contributes to non-obstructive azoospermia in humans. Human Genetics **142**(4), 531–541 (2023) https://doi.org/10.1007/s00439-022-02515-z

[36] Okada, M., Cheeseman, I.M., Hori, T., Okawa, K., McLeod, I.X., Yates, J.R., Desai, A., Fukagawa, T.: The CENP-H–I complex is required for the efficient incorporation of newly synthesized CENP-A into centromeres. Nature Cell Biology **8**(5), 446–457 (2006) https://doi.org/10.1038/ncb1396

[37] Cui, Y., Wang, W., Dong, N., Lou, J., Srinivasan, D.K., Cheng, W., Huang,

X., Liu, M., Fang, C., Peng, J., Chen, S., Wu, S., Liu, Z., Dong, L., Zhou, Y., Wu, Q.: Role of corin in trophoblast invasion and uterine spiral artery remodelling in pregnancy. Nature **484**(7393), 246–250 (2012) https://doi.org/10.1038/nature10897

[38] Ballatori, N., Christian, W.V., Lee, J.Y., Dawson, P.A., Soroka, C.J., Boyer, J.L., Madejczyk, M.S., Li, N.: OSTα-OSTβ: A major basolateral bile acid and steroid transporter in human intestinal, renal, and biliary epithelia. Hepatology **42**(6) (2005) https://doi.org/10.1002/hep.20961

[39] Beurois, J., Martinez, G., Cazin, C., Kherraf, Z.-E., Amiri-Yekta, A., Thierry-Mieg, N., Bidart, M., Petre, G., Satre, V., Brouillet, S., Touré, A., Arnoult, C., Ray, P.F., Coutton, C.: CFAP70 mutations lead to male infertility due to severe astheno-teratozoospermia. A case report. Human Reproduction **34**(10), 2071–2079 (2019) https://doi.org/10.1093/humrep/dez166

[40] Sarkardeh, H., Totonchi, M., Asadpour, O., Sadighi Gilani, M.A., Zamani Esteki, M., Almadani, N., Borjian Boroujeni, P., Gourabi, H.: Association of MOV10L1 gene polymorphisms and male infertility in azoospermic men with complete maturation arrest. Journal of Assisted Reproduction and Genetics **31**(7), 865–871 (2014) https://doi.org/10.1007/s10815-014-0240-1

[41] MOURELATOS, Z., GONATAS, J.O., CINATO, E., GONATAS, N.K.: Cloning and Sequence Analysis of the Human MG160, a Fibroblast Growth Factor and E-Selectin Binding Membrane Sialoglycoprotein of the Golgi Apparatus. DNA and Cell Biology **15**(12), 1121–1128 (1996) https://doi.org/10.1089/dna.1996.15.1121

[42] Akinwumi, B.C., Bordun, K.-A.M., Anderson, H.D.: Biological Activities of Stilbenoids. International Journal of Molecular Sciences **19**(3) (2018) https://doi.org/10.3390/ijms19030792

[43] Elizabeth Rogers, M., Maisels, F., Williamson, E.A., Fernandez, M., Tutin, C.E.G.: Gorilla diet in the Lopé Reserve, Gabon:. Oecologia **84**(3), 326–339 (1990) https://doi.org/10.1007/BF00329756

[44] Dan-zeng, Z.-g., Bai-ma, Y.-j., Huang, J., Suo-lang, W.-j., Ge-sang, Q.-z., Suo-na, Y.-z., Wang, Y.-s., Baima, Z.-g., Ge-sang, l.-b.: Integrative proteomics and metabolomics reveal important pathways and potential biomarkers in high-altitude pulmonary hypertension. Scientific Reports **15**(1), 24999 (2025) https://doi.org/10.1038/s41598-025-09477-y

[45] Guo, B.-X., Zhang, Y., Sun, X.-Y., Sun, Y.-X., Lv, W.-J., Xu, S.-X., Yang, G., Ren, W.-H.: Convergent evolution in high-altitude and marine mammals: Molecular adaptations to pulmonary fibrosis and hypoxia . Zoological Research **45**(6), 1209–1220 (2024) https://doi.org/10.24272/j.issn.2095-8137.2024.029

[46] Verheij, J.B.G.M., Kunze, J., Osinga, J., Essen, A.J., Hofstra, R.M.W.: ABCD

syndrome is caused by a homozygous mutation in the EDNRB gene. American Journal of Medical Genetics **108**(3), 223–225 (2002) https://doi.org/10.1002/ajmg.10172

[47] Waselle, L., Coppola, T., Fukuda, M., Iezzi, M., El-Amraoui, A., Petit, C., Regazzi, R.: Involvement of the Rab27 Binding Protein Slac2c/MyRIP in Insulin Exocytosis. Molecular Biology of the Cell **14**(10), 4103–4113 (2003) https://doi.org/10.1091/mbc.e03-01-0022

[48] Valk, T., Jensen, A., Caillaud, D., Guschanski, K.: Comparative genomic analyses provide new insights into evolutionary history and conservation genomics of gorillas. BMC Ecology and Evolution **24**(1), 14 (2024) https://doi.org/10.1186/s12862-023-02195-x

[49] Ge, R.-L., Simonson, T.S., Gordeuk, V., Prchal, J.T., McClain, D.A.: Metabolic aspects of high-altitude adaptation in Tibetans. Experimental Physiology **100**(11), 1247–1255 (2015) https://doi.org/10.1113/EP085292

[50] Noordwijk, M.A., Arora, N., Willems, E.P., Dunkel, L.P., Amda, R.N., Mardianah, N., Ackermann, C., Krützen, M., Schaik, C.P.: Female philopatry and its social benefits among Bornean orangutans. Behavioral Ecology and Sociobiology **66**(6), 823–834 (2012) https://doi.org/10.1007/s00265-012-1330-7

[51] Mörchen, J., Luhn, F., Wassmer, O., Kunz, J.A., Kulik, L., Noordwijk, M.A., Rianti, P., Rahmaeti, T., Utami Atmoko, S.S., Widdig, A., Schuppli, C.: Orangutan males make increased use of social learning opportunities, when resource availability is high. iScience **27**(2) (2024) https://doi.org/10.1016/j.isci.2024.108940

[52] Spehar, S.N., Sheil, D., Harrison, T., Louys, J., Ancrenaz, M., Marshall, A.J., Wich, S.A., Bruford, M.W., Meijaard, E.: Orangutans venture out of the rainforest and into the Anthropocene. Science Advances **4**(6), 1701422 (2026) https://doi.org/10.1126/sciadv.1701422

[53] COURTENAY, J.: Inter- or Intra-Island Variation? An Assessment of the Differences Between Bornean and Sumatran Orang-Utans. Orangutan Biology, 19–29 (1988)

[54] Knott, C.D.: Changes in Orangutan Caloric Intake, Energy Balance, and Ketones in Response to Fluctuating Fruit Availability. International Journal of Primatology **19**(6), 1061–1079 (1998) https://doi.org/10.1023/A:1020330404983

[55] Gleeson, P.A.: The role of endosomes in innate and adaptive immunity. Seminars in Cell & Developmental Biology **31**, 64–72 (2014) https://doi.org/10.1016/j.semcdb.2014.03.002

[56] Besnard, M.-L., Raymond-Letron, I., Jourdan, G., Becker, C., Steinmetz, H.W.:

MORBIDITY AND MORTALITY REVIEW OF THE CAPTIVE EUROPEAN ASSOCIATION OF ZOOS AND AQUARIA EX-SITU PROGRAMME ORANGUTAN (¡i¿PONGO¡/i¿ SPECIES) POPULATION BETWEEN 2000 AND 2018. Journal of Zoo and Wildlife Medicine **56**(2), 237–247 (2025) https://doi.org/10.1638/2022-0137

[57] Mattle-Greminger, M.P., Bilgin Sonay, T., Nater, A., Pybus, M., Desai, T., Valles, G., Casals, F., Scally, A., Bertranpetit, J., Marques-Bonet, T., Schaik, C.P., Anisimova, M., Krützen, M.: Genomes reveal marked differences in the adaptive evolution between orangutan species. Genome Biology **19**(1), 193 (2018) https://doi.org/10.1186/s13059-018-1562-6

Supplementary Figures

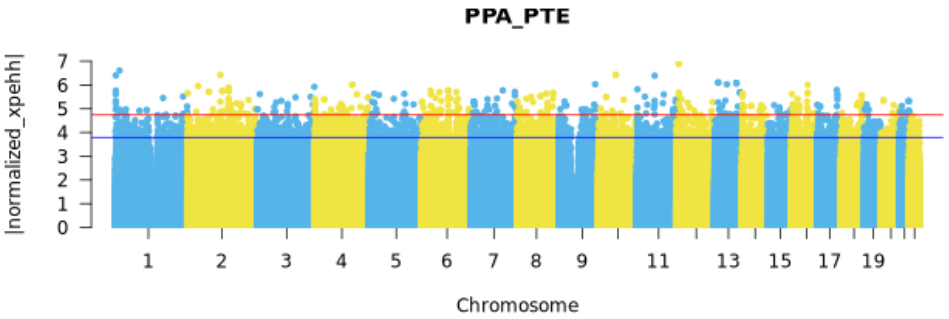

Fig. S1 Genome-wide Manhattan plot of unphased XP-EHH values for PPA vs. PTE. The blue horizontal line marks the top 0.05% cutoff, and the red horizontal line marks the top 0.005% cutoff.

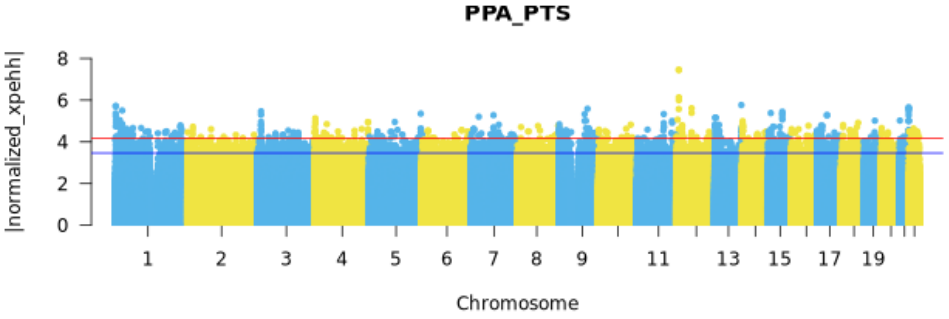

Fig. S2 Genome-wide Manhattan plot of unphased XP-EHH values for PPA vs. PTS. The blue horizontal line indicates the top 0.05% cutoff, and the red horizontal line indicates the top 0.005% cutoff.

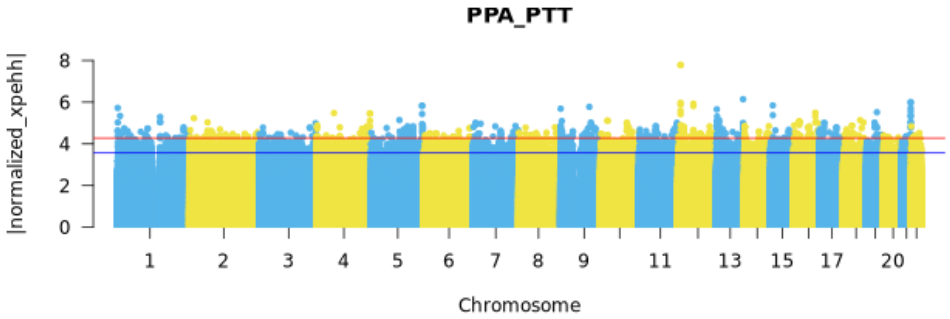

Fig. S3 Genome-wide Manhattan plot of unphased XP-EHH values for PPA vs. PTT. The blue horizontal line marks the top 0.05% cutoff, and the red horizontal line marks the top 0.005% cutoff.

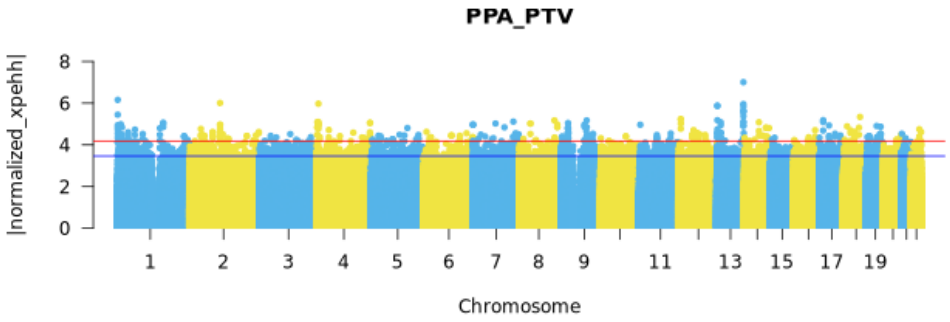

Fig. S4 Genome-wide Manhattan plot of unphased XP-EHH values for PPA vs. PTV. The blue horizontal line marks the top 0.05% cutoff, and the red horizontal line marks the top 0.005% cutoff.

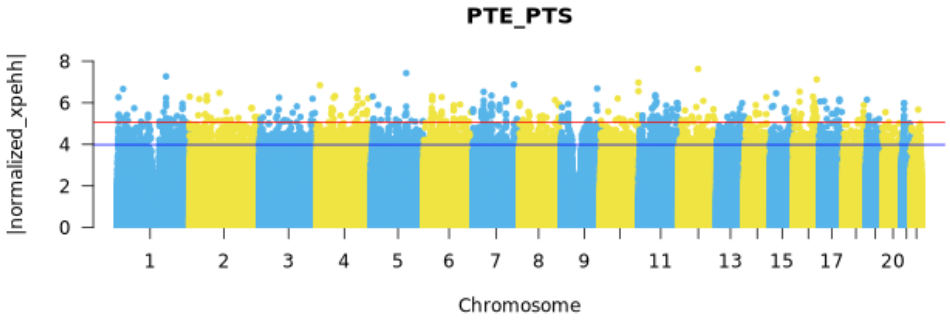

Fig. S5 Genome-wide Manhattan plot of unphased XP-EHH values for PTE vs. PTS. The blue horizontal line marks the top 0.05% cutoff, and the red horizontal line marks the top 0.005% cutoff.

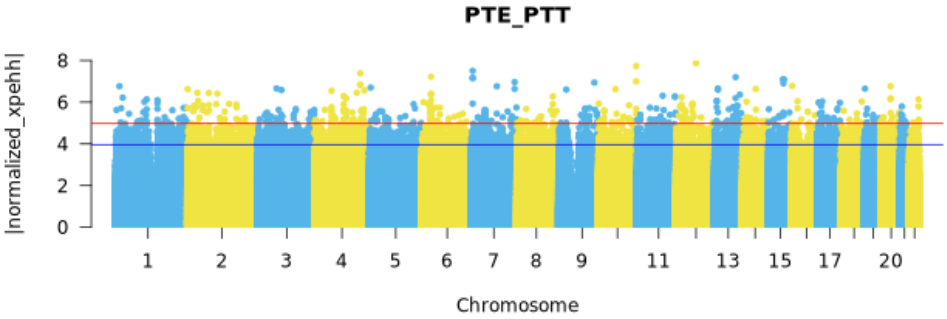

Fig. S6 Genome-wide Manhattan plot of unphased XP-EHH values for PTE vs. PTT. The blue horizontal line marks the top 0.05% cutoff, and the red horizontal line marks the top 0.005% cutoff.

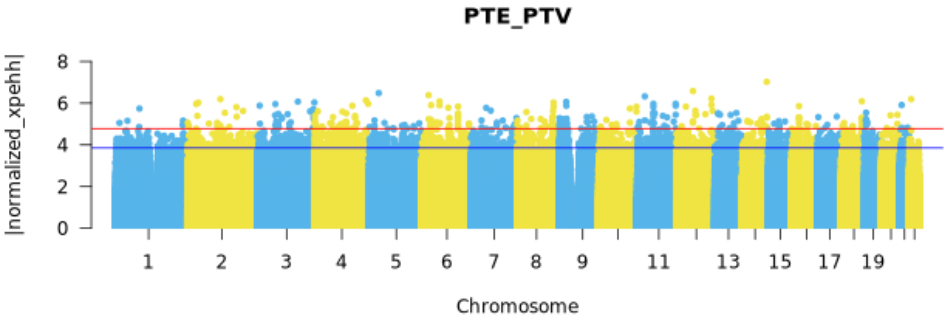

Fig. S7 Genome-wide Manhattan plot of unphased XP-EHH values for PTE vs. PTV. The blue horizontal line marks the top 0.05% cutoff, and the red horizontal line marks the top 0.005% cutoff.

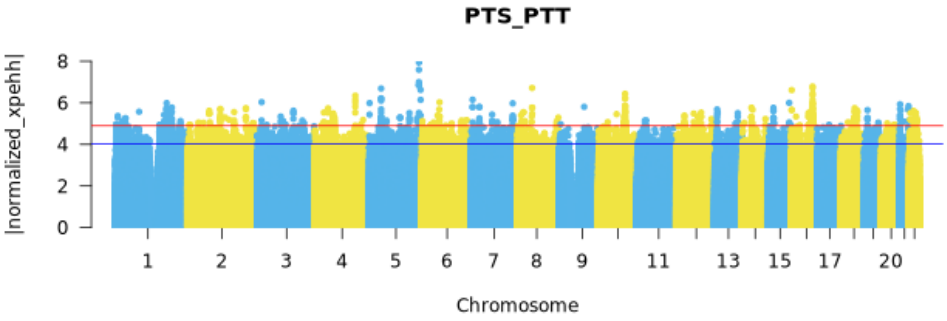

Fig. S8 Genome-wide Manhattan plot of unphased XP-EHH values for PTS vs. PTT. The blue horizontal line marks the top 0.05% cutoff, and the red horizontal line marks the top 0.005% cutoff.

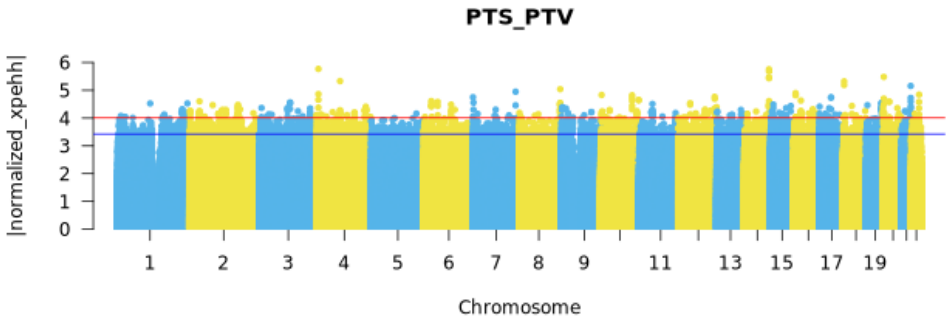

Fig. S9 Genome-wide Manhattan plot of unphased XP-EHH values for PTS vs. PTV. The blue horizontal line marks the top 0.05% cutoff, and the red horizontal line marks the top 0.005% cutoff.

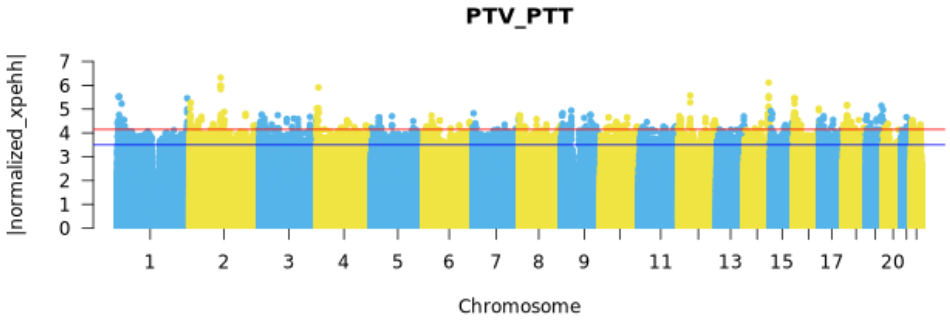

Fig. S10 Genome-wide Manhattan plot of unphased XP-EHH values for PTV vs. PTT. The blue horizontal line marks the top 0.05% cutoff, and the red horizontal line marks the top 0.005% cutoff.

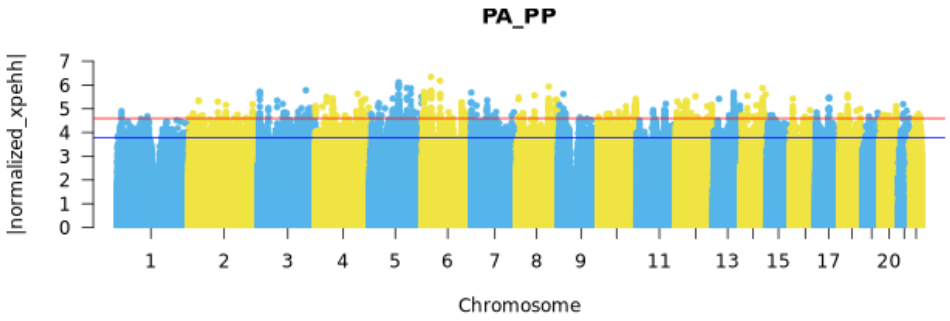

Fig. S11 Genome-wide Manhattan plot of unphased XP-EHH values for PA vs. PP. The blue horizontal line marks the top 0.05% cutoff, and the red horizontal line marks the top 0.005% cutoff.

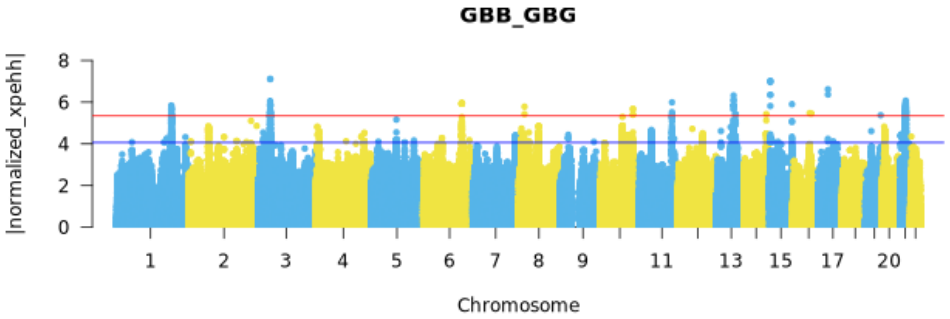

Fig. S12 Genome-wide Manhattan plot of unphased XP-EHH values for GBB vs. GBG. The blue horizontal line marks the top 0.05% cutoff, and the red horizontal line marks the top 0.005% cutoff.

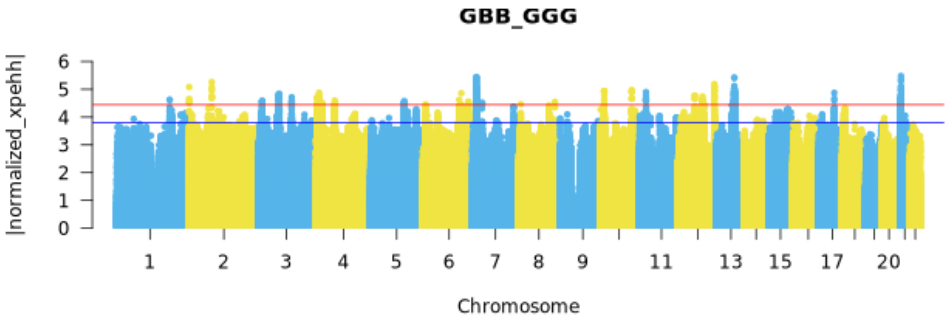

Fig. S13 Genome-wide Manhattan plot of unphased XP-EHH values for GBB vs. GGG. The blue horizontal line marks the top 0.05% cutoff, and the red horizontal line marks the top 0.005% cutoff.

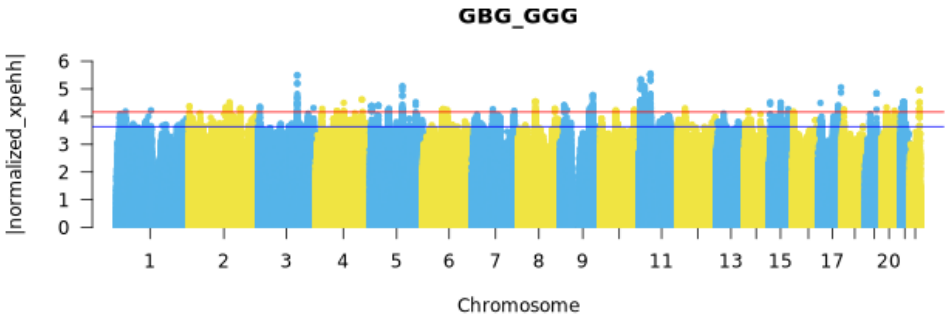

Fig. S14 Genome-wide Manhattan plot of unphased XP-EHH values for GBG vs. GGG. The blue horizontal line marks the top 0.05% cutoff, and the red horizontal line marks the top 0.005% cutoff.

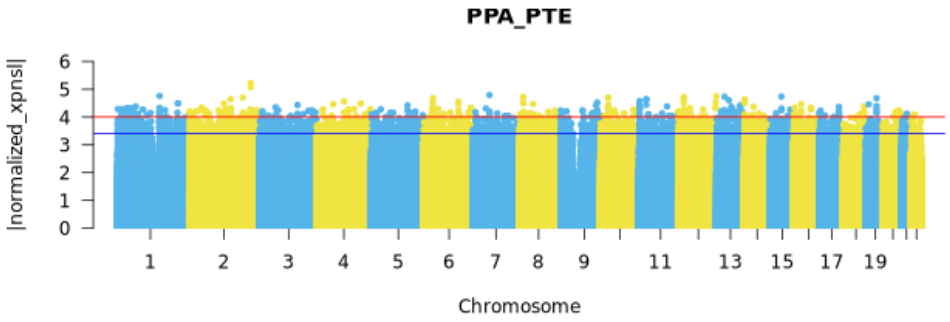

Fig. S15 Genome-wide Manhattan plot of unphased XP-nSL values for PPA vs. PTE. The blue horizontal line marks the top 0.05% cutoff, and the red horizontal line marks the top 0.005% cutoff.

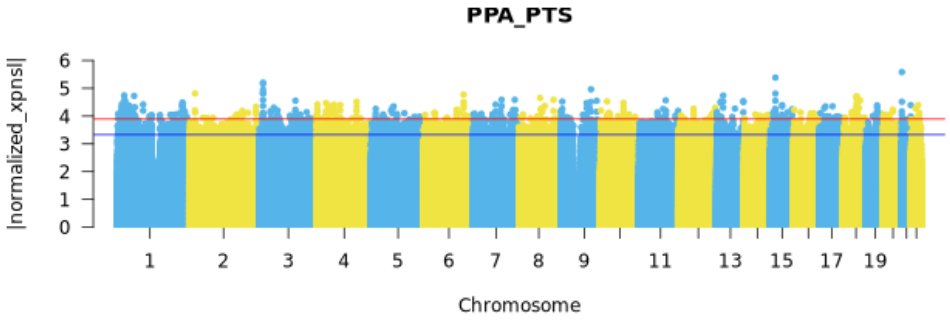

Fig. S16 Genome-wide Manhattan plot of unphased XP-nSL values for PPA vs. PTS. The blue horizontal line indicates the top 0.05% cutoff, and the red horizontal line indicates the top 0.005% cutoff.

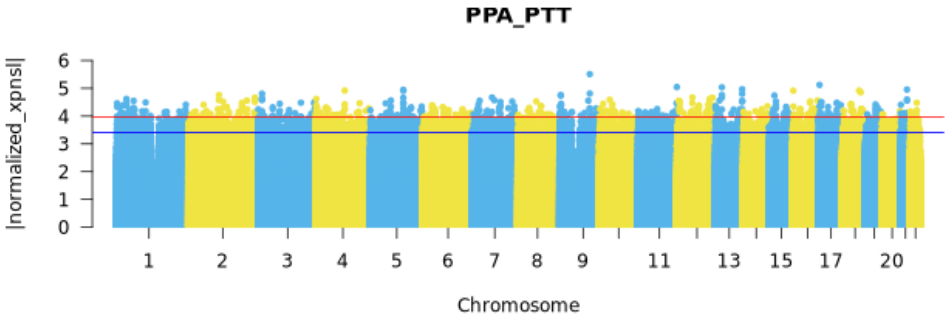

Fig. S17 Genome-wide Manhattan plot of unphased XP-nSL values for PPA vs. PTT. The blue horizontal line marks the top 0.05% cutoff, and the red horizontal line marks the top 0.005% cutoff.

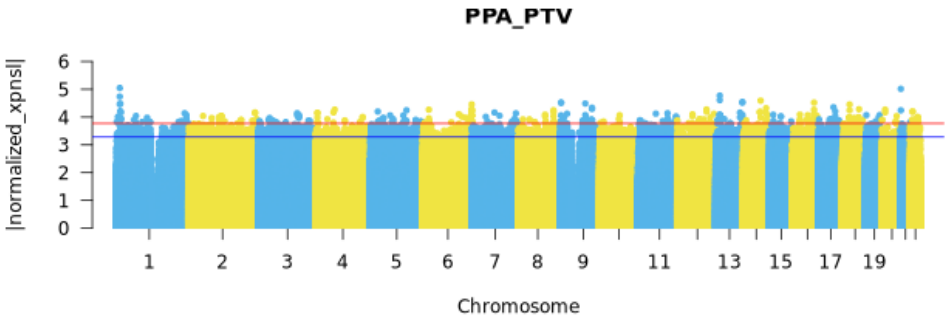

Fig. S18 Genome-wide Manhattan plot of unphased XP-nSL values for PPA vs. PTV. The blue horizontal line marks the top 0.05% cutoff, and the red horizontal line marks the top 0.005% cutoff.

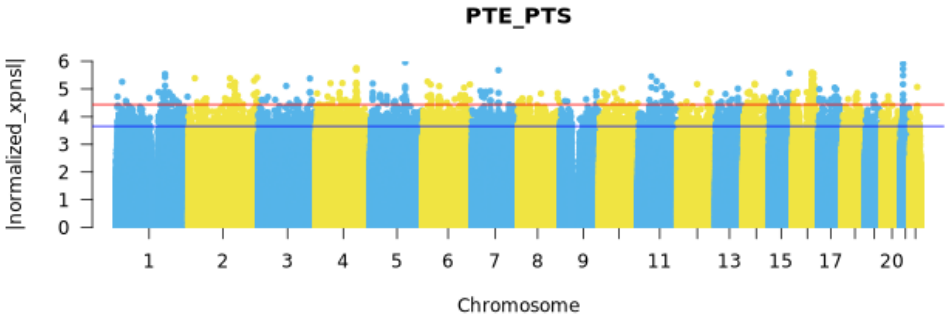

Fig. S19 Genome-wide Manhattan plot of unphased XP-nSL values for PTE vs. PTS. The blue horizontal line marks the top 0.05% cutoff, and the red horizontal line marks the top 0.005% cutoff.

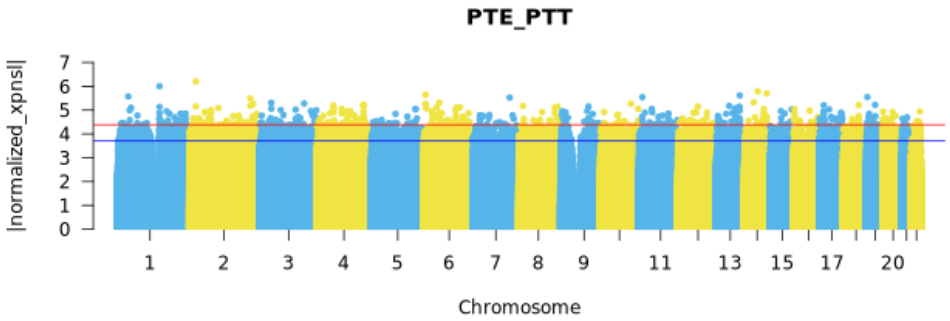

Fig. S20 Genome-wide Manhattan plot of unphased XP-nSL values for PTE vs. PTT. The blue horizontal line marks the top 0.05% cutoff, and the red horizontal line marks the top 0.005% cutoff.

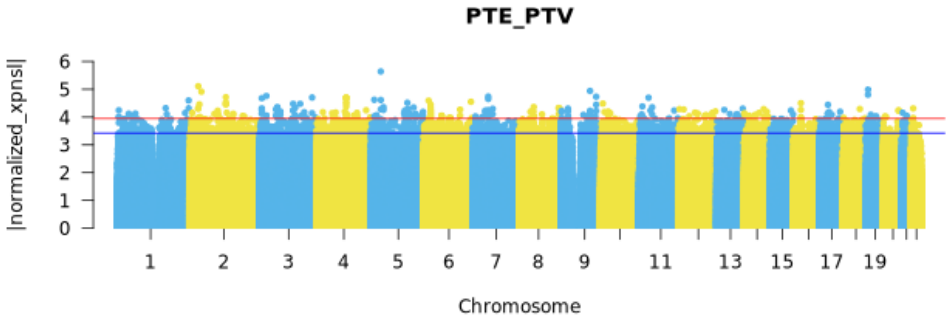

Fig. S21 Genome-wide Manhattan plot of unphased XP-nSL values for PTE vs. PTV. The blue horizontal line marks the top 0.05% cutoff, and the red horizontal line marks the top 0.005% cutoff.

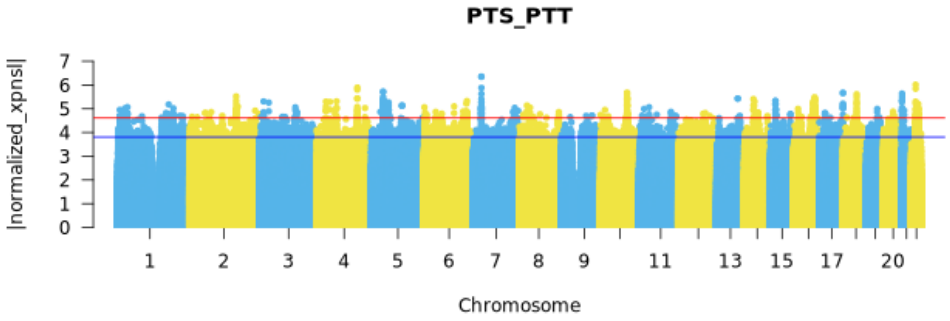

Fig. S22 Genome-wide Manhattan plot of unphased XP-nSL values for PTS vs. PTT. The blue horizontal line marks the top 0.05% cutoff, and the red horizontal line marks the top 0.005% cutoff.

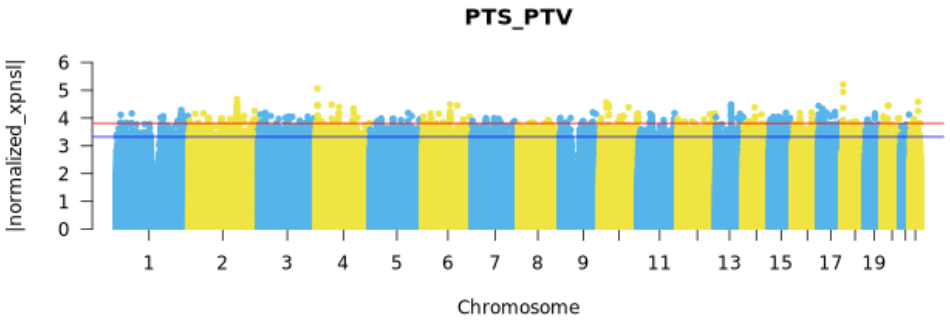

Fig. S23 Genome-wide Manhattan plot of unphased XP-nSL values for PTS vs. PTV. The blue horizontal line marks the top 0.05% cutoff, and the red horizontal line marks the top 0.005% cutoff.

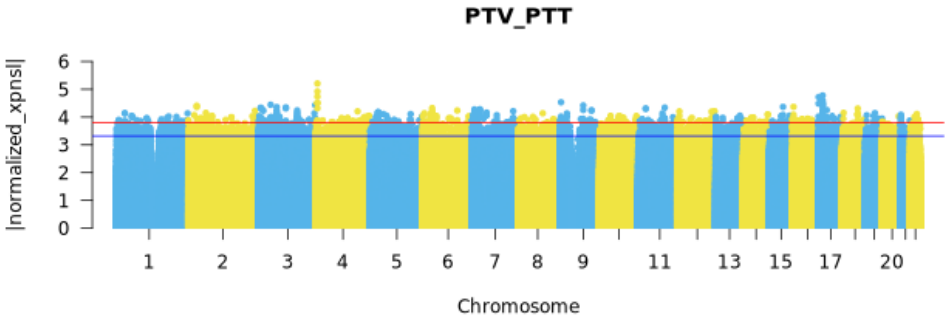

Fig. S24 Genome-wide Manhattan plot of unphased XP-nSL values for PTV vs. PTT. The blue horizontal line marks the top 0.05% cutoff, and the red horizontal line marks the top 0.005% cutoff.

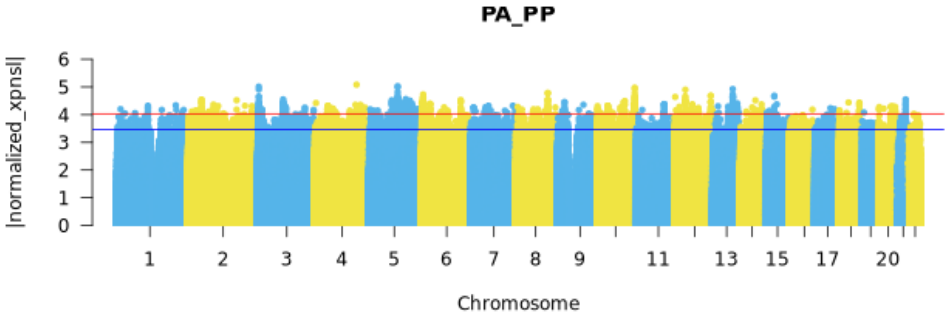

Fig. S25 Genome-wide Manhattan plot of unphased XP-nSL values for PA vs. PP. The blue horizontal line marks the top 0.05% cutoff, and the red horizontal line marks the top 0.005% cutoff.

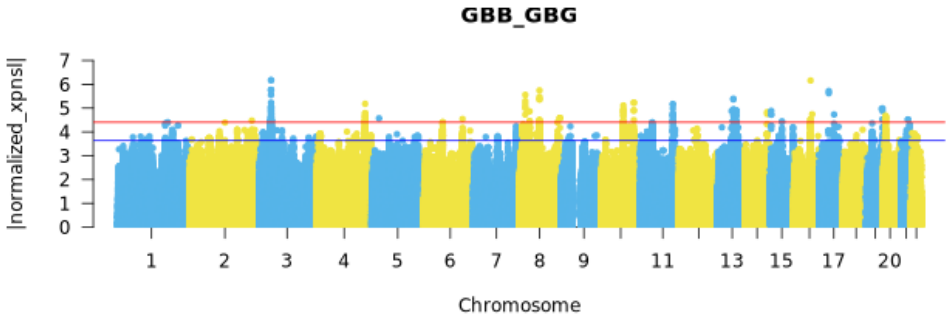

Fig. S26 Genome-wide Manhattan plot of unphased XP-nSL values for GBB vs. GBG. The blue horizontal line marks the top 0.05% cutoff, and the red horizontal line marks the top 0.005% cutoff.

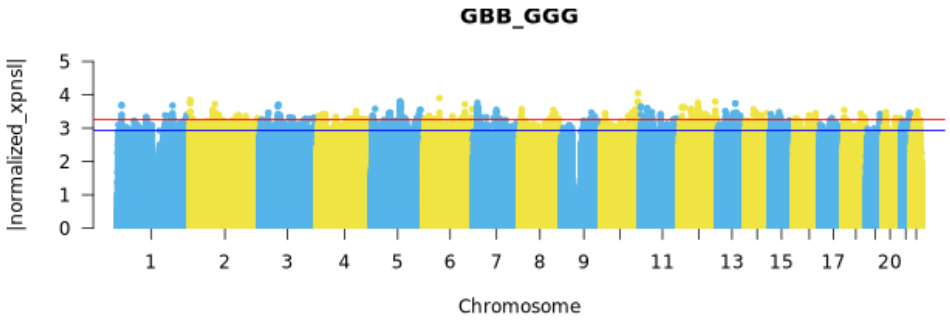

Fig. S27 Genome-wide Manhattan plot of unphased XP-nSL values for GBB vs. GGG. The blue horizontal line marks the top 0.05% cutoff, and the red horizontal line marks the top 0.005% cutoff.

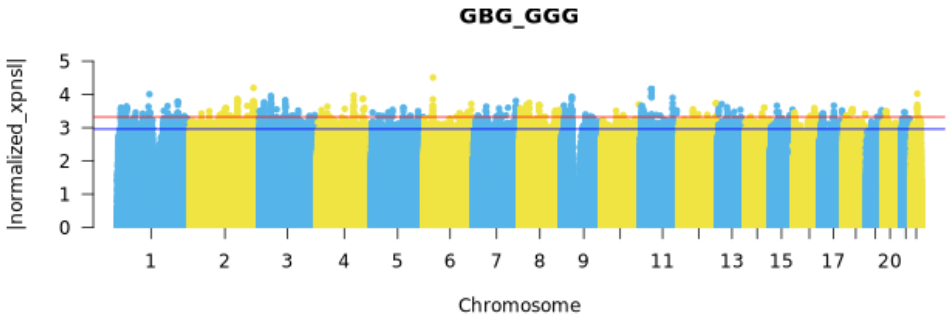

Fig. S28 Genome-wide Manhattan plot of unphased XP-EHH values for GBG vs. GGG. The blue horizontal line marks the top 0.05% cutoff, and the red horizontal line marks the top 0.005% cutoff.

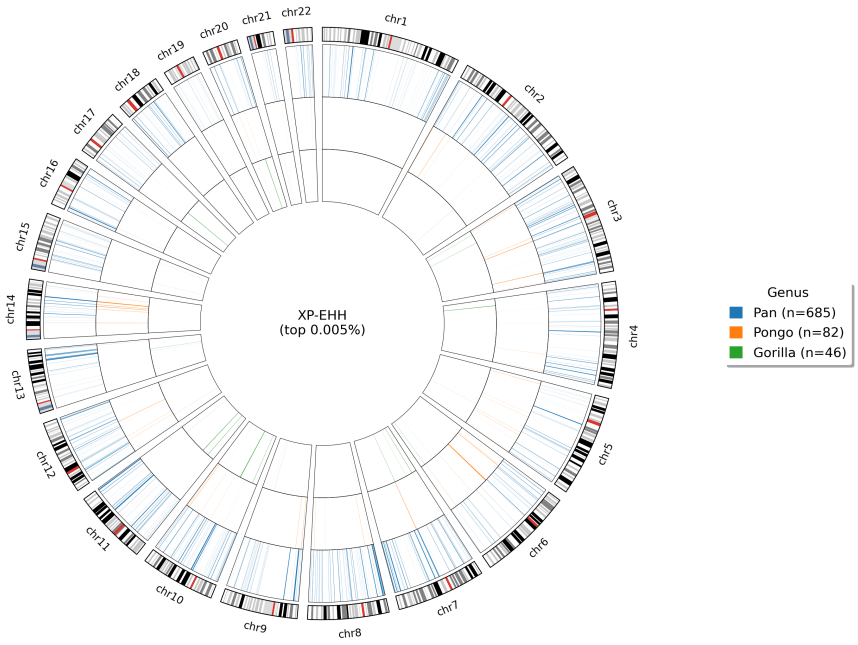

Fig. S29 Genes overlapping top 0.005% unphased XP-EHH outlier sites in *Pan*, *Pongo*, and *Gorilla*.

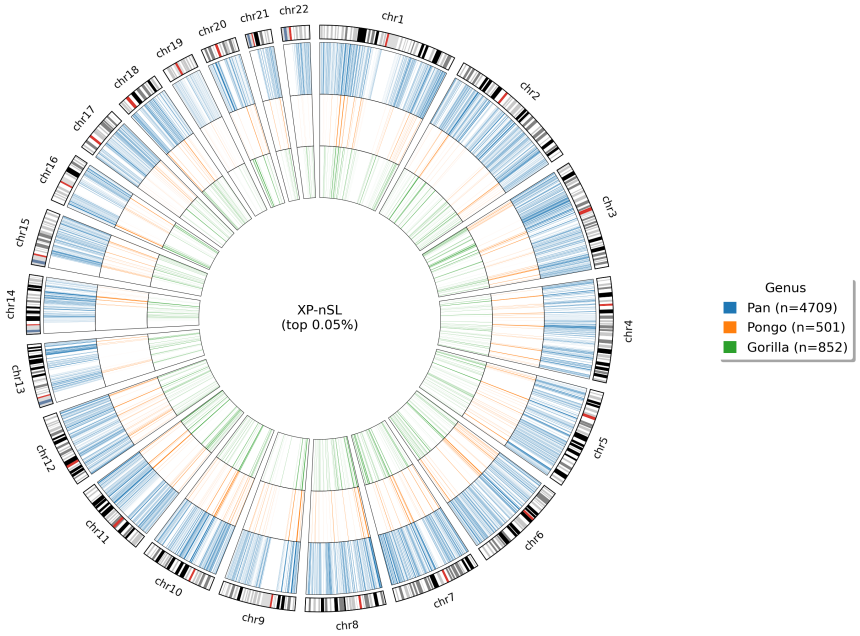

Fig. S30 Genes overlapping top 0.05% unphased XP-nSL outlier sites in *Pan*, *Pongo*, and *Gorilla*.

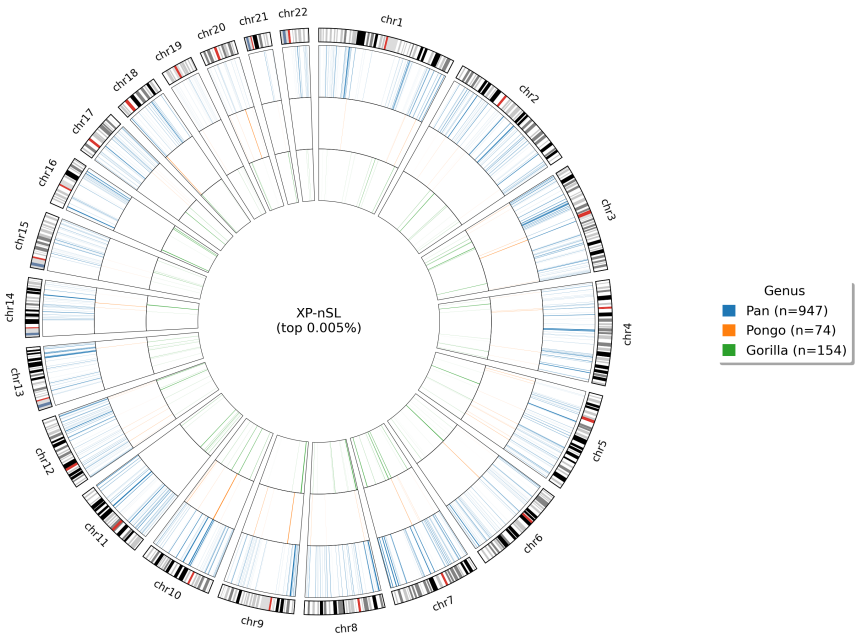

Fig. S31 Genes overlapping top 0.005% unphased XP-nSL outlier sites in *Pan*, *Pongo*, and *Gorilla*.

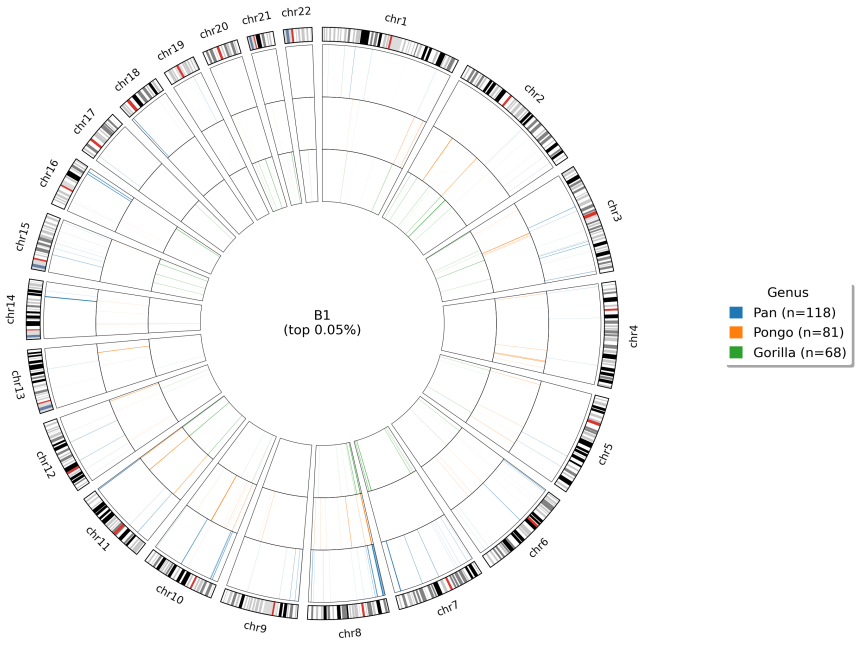

Fig. S32 Genes overlapping top 0.05% unfolded $\beta^{(1)}$ outlier sites in *Pan*, *Pongo*, and *Gorilla*.

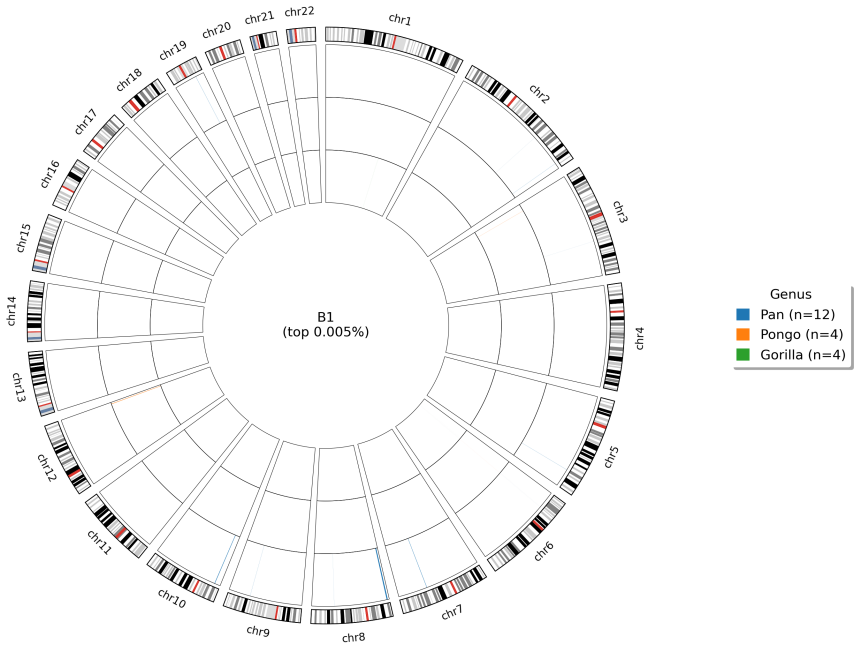

Fig. S33 Genes overlapping top 0.005% unfolded $\beta^{(1)}$ outlier sites in *Pan*, *Pongo*, and *Gorilla*.

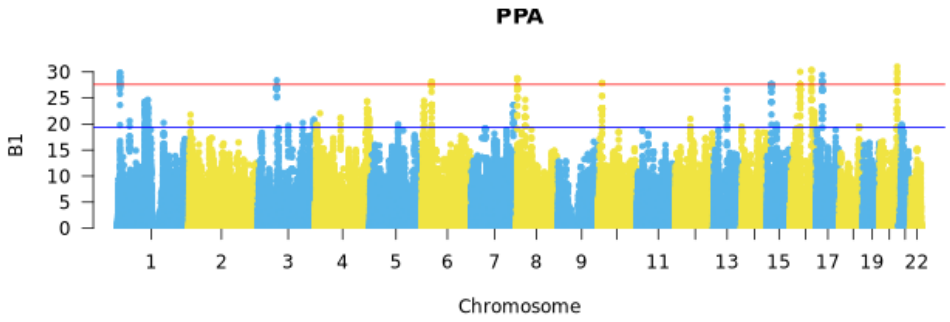

Fig. S34 Genome-wide Manhattan plot of $\beta^{(1)}$ values for PPA. The blue horizontal line marks the top 0.05% cutoff, and the red horizontal line marks the top 0.005% cutoff.

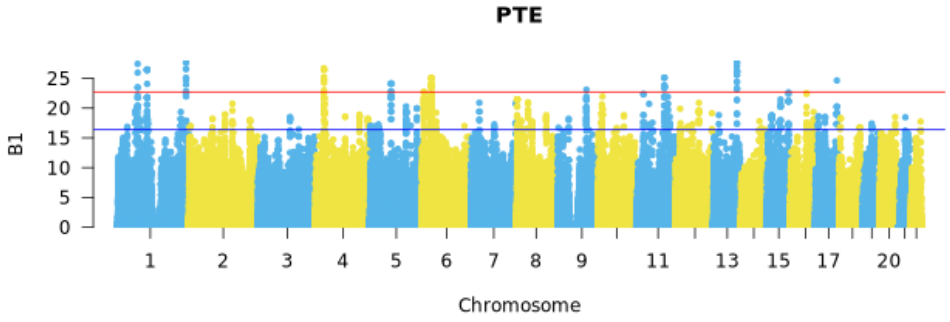

Fig. S35 Genome-wide Manhattan plot of $\beta^{(1)}$ values for PTE. The blue horizontal line indicates the top 0.05% cutoff, and the red horizontal line indicates the top 0.005% cutoff.

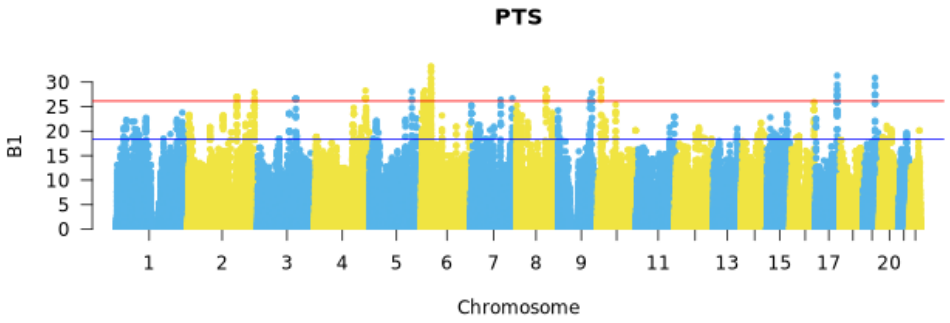

Fig. S36 Genome-wide Manhattan plot of $\beta^{(1)}$ values for PTS. The blue horizontal line marks the top 0.05% cutoff, and the red horizontal line marks the top 0.005% cutoff.

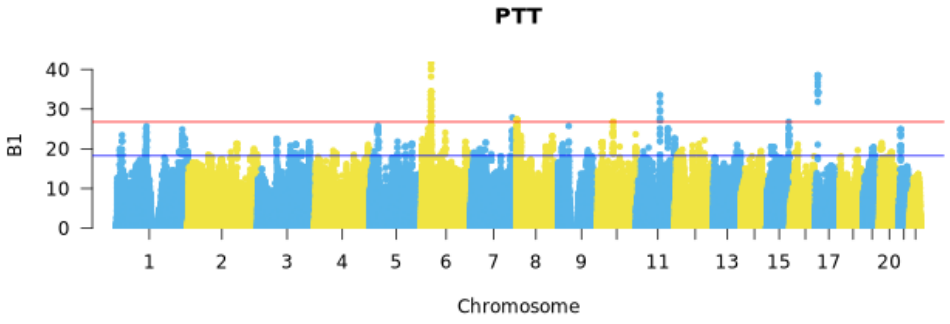

Fig. S37 Genome-wide Manhattan plot of $\beta^{(1)}$ values for PTT. The blue horizontal line marks the top 0.05% cutoff, and the red horizontal line marks the top 0.005% cutoff.

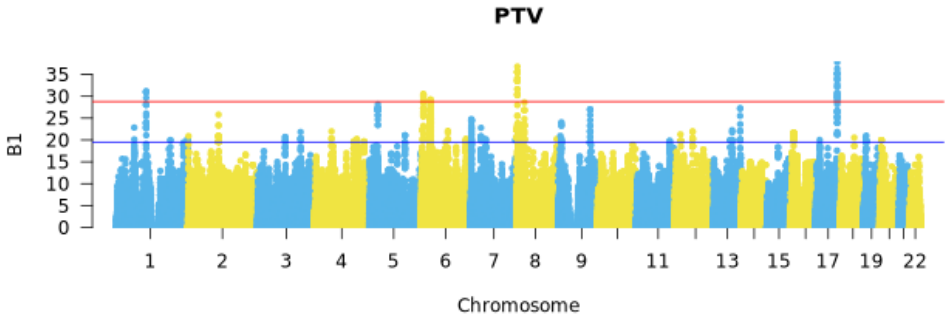

Fig. S38 Genome-wide Manhattan plot of $\beta^{(1)}$ values for PTV. The blue horizontal line marks the top 0.05% cutoff, and the red horizontal line marks the top 0.005% cutoff.

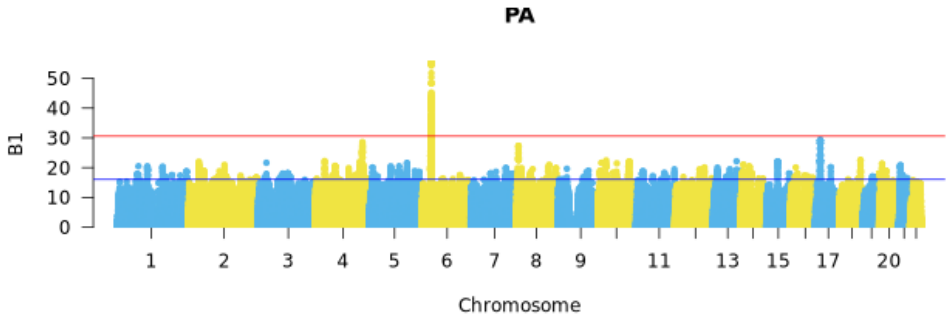

Fig. S39 Genome-wide Manhattan plot of $\beta^{(1)}$ values for PA. The blue horizontal line marks the top 0.05% cutoff, and the red horizontal line marks the top 0.005% cutoff.

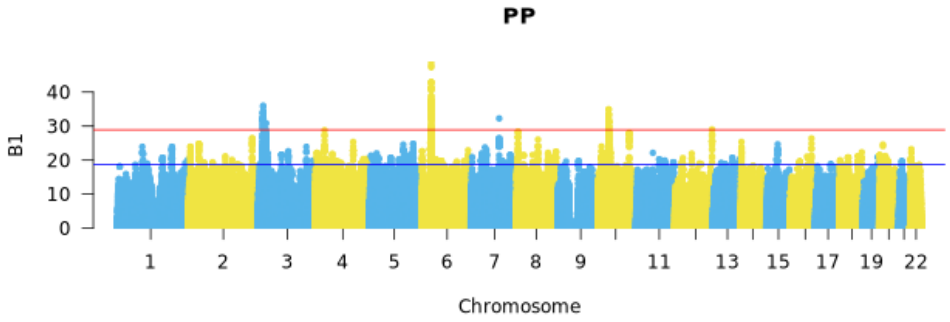

Fig. S40 Genome-wide Manhattan plot of $\beta^{(1)}$ values for PP. The blue horizontal line marks the top 0.05% cutoff, and the red horizontal line marks the top 0.005% cutoff.

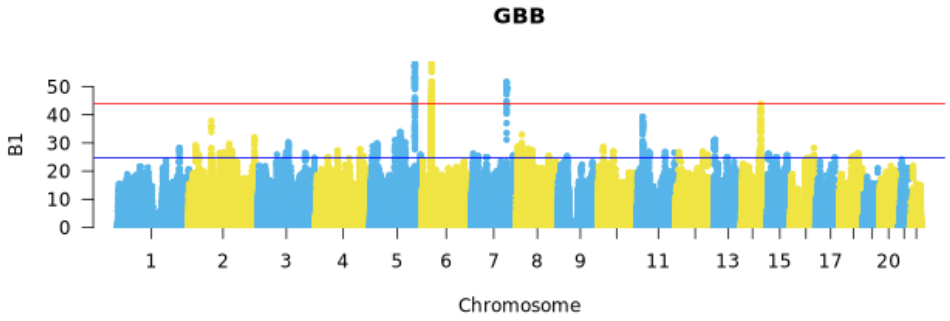

Fig. S41 Genome-wide Manhattan plot of $\beta^{(1)}$ values for GBB. The blue horizontal line marks the top 0.05% cutoff, and the red horizontal line marks the top 0.005% cutoff.

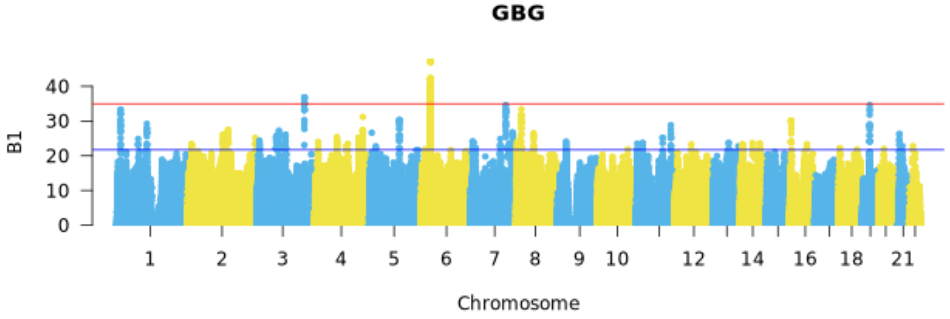

Fig. S42 Genome-wide Manhattan plot of $\beta^{(1)}$ values for GBG. The blue horizontal line marks the top 0.05% cutoff, and the red horizontal line marks the top 0.005% cutoff.

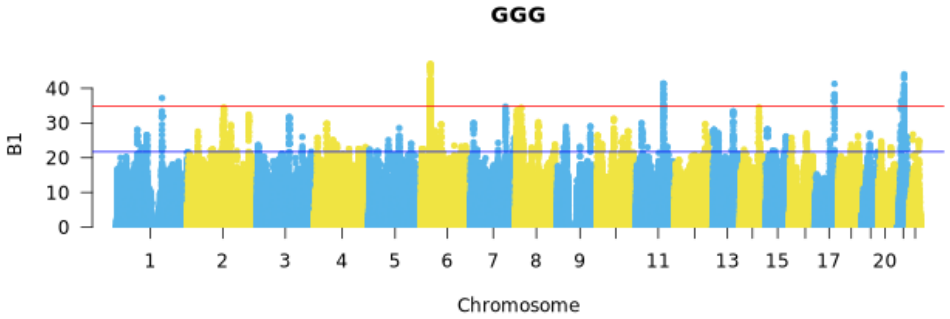

Fig. S43 Genome-wide Manhattan plot of $\beta^{(1)}$ values for GGG. The blue horizontal line marks the top 0.05% cutoff, and the red horizontal line marks the top 0.005% cutoff.

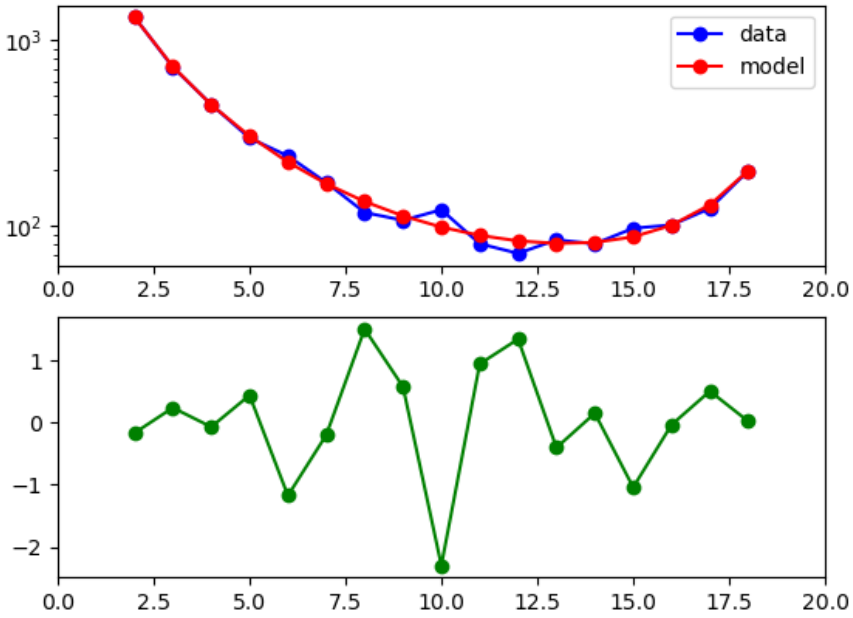

Fig. S44 Model fit to the AFS using synonymous SNPs from PPA. The blue line shows the observed AFS from the data, the red line shows the inferred AFS based on the maximum likelihood estimates in Additional File 2: Table S88, and the green line shows the residual between the observed and model AFS.

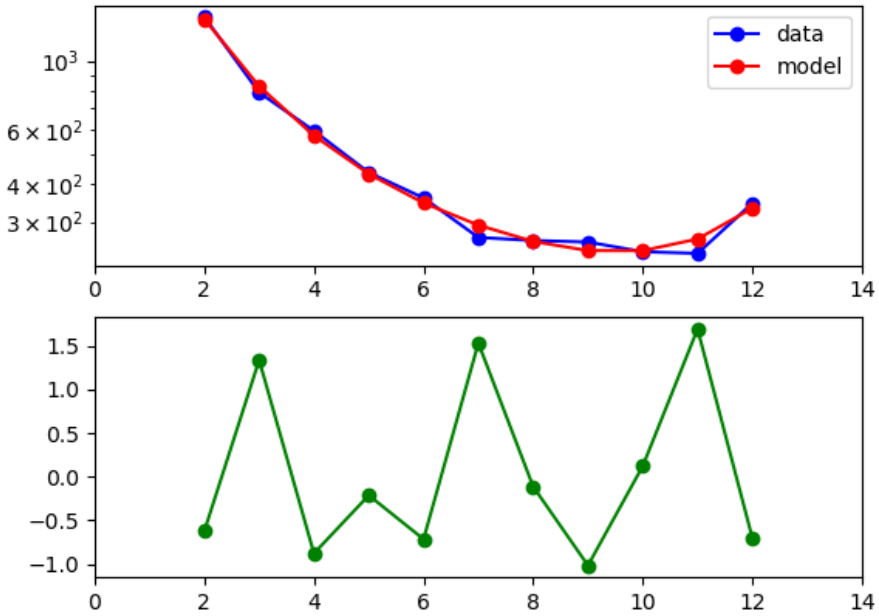

Fig. S45 Model fit to the AFS using synonymous SNPs from PTE. The blue line shows the observed AFS from the data, the red line shows the inferred AFS based on the maximum likelihood estimates in Additional File 2: Table S88, and the green line shows the residual between the observed and model AFS.

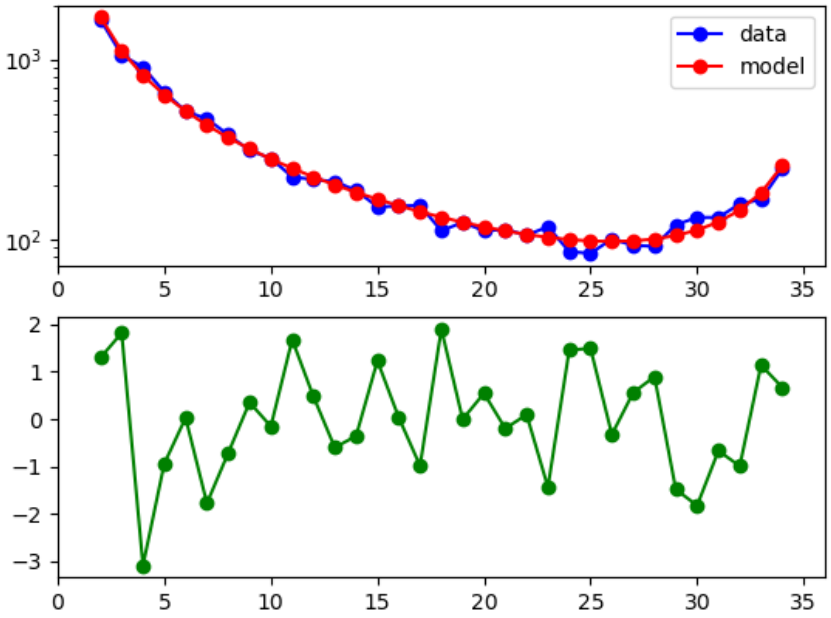

Fig. S46 Model fit to the AFS using synonymous SNPs from PTE. The blue line shows the observed AFS from the data, the red line shows the inferred AFS based on the maximum likelihood estimates in Additional File 2: Table S88, and the green line shows the residual between the observed and model AFS.

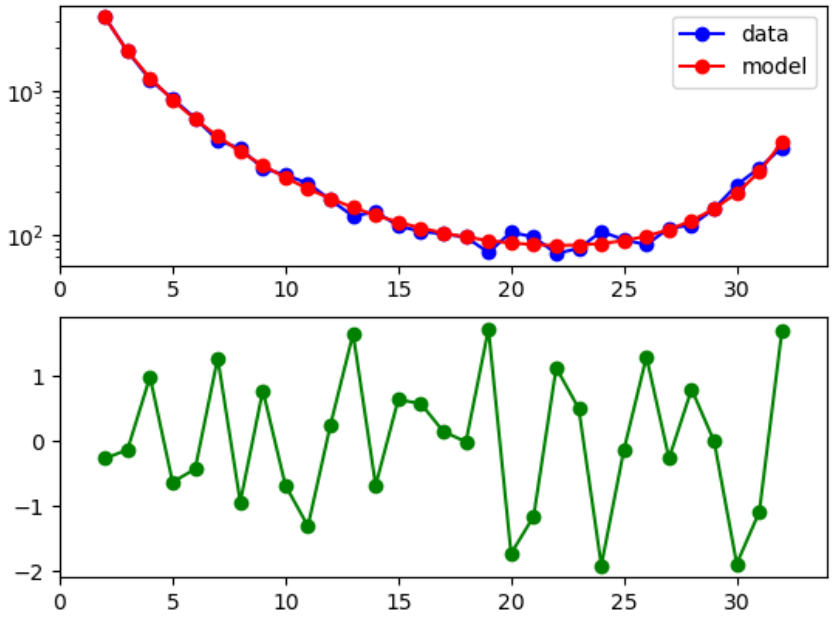

Fig. S47 Model fit to the AFS using synonymous SNPs from PTT. The blue line shows the observed AFS from the data, the red line shows the inferred AFS based on the maximum likelihood estimates in Additional File 2: Table S88, and the green line shows the residual between the observed and model AFS.

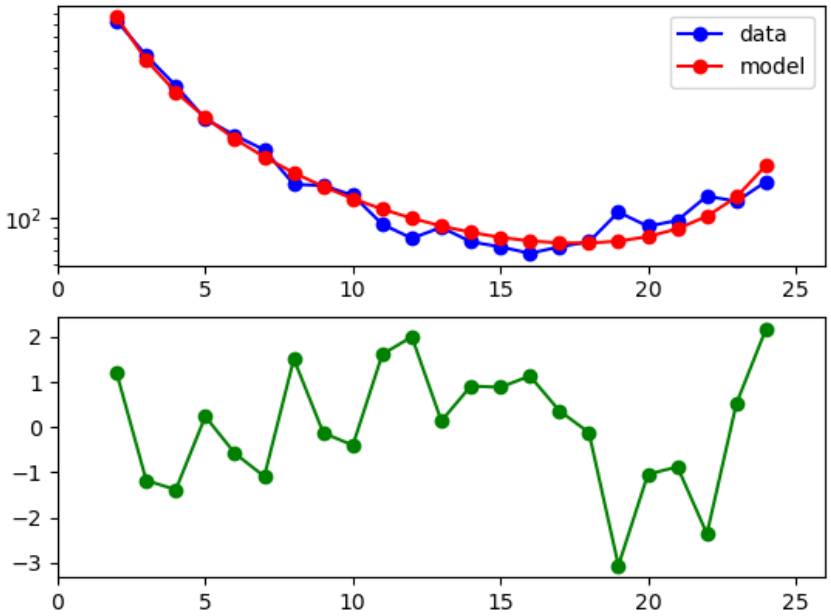

Fig. S48 Model fit to the AFS using synonymous SNPs from PTV. The blue line shows the observed AFS from the data, the red line shows the inferred AFS based on the maximum likelihood estimates in Additional File 2: Table S88, and the green line shows the residual between the observed and model AFS.

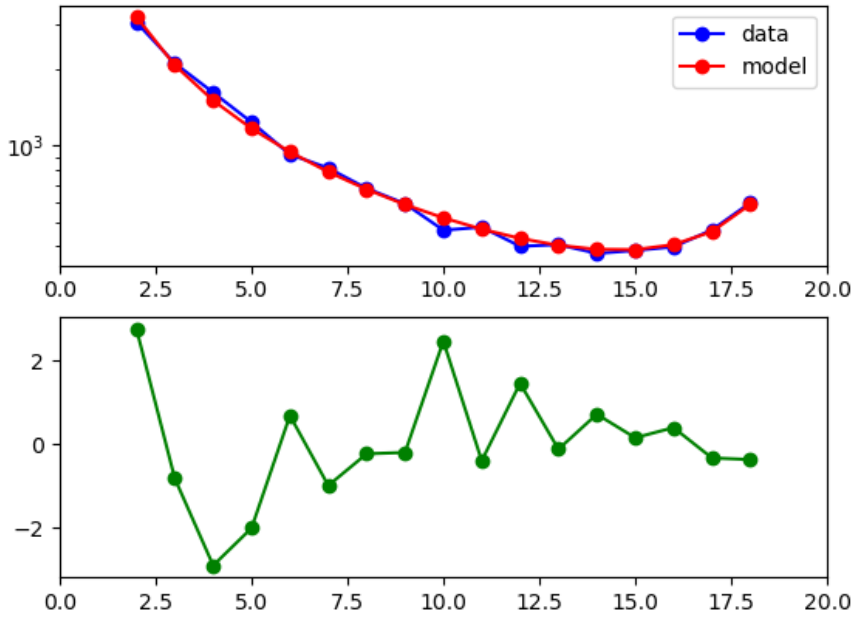

Fig. S49 Model fit to the AFS using synonymous SNPs from PA. The blue line shows the observed AFS from the data, the red line shows the inferred AFS based on the maximum likelihood estimates in Additional File 2: Table S88, and the green line shows the residual between the observed and model AFS.

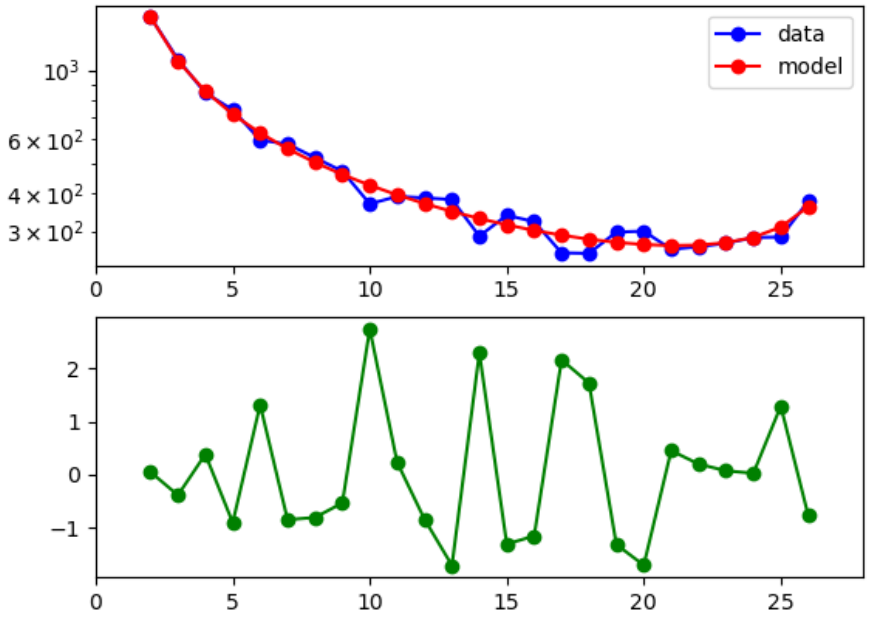

Fig. S50 Model fit to the AFS using synonymous SNPs from PP. The blue line shows the observed AFS from the data, the red line shows the inferred AFS based on the maximum likelihood estimates in Additional File 2: Table S88, and the green line shows the residual between the observed and model AFS.

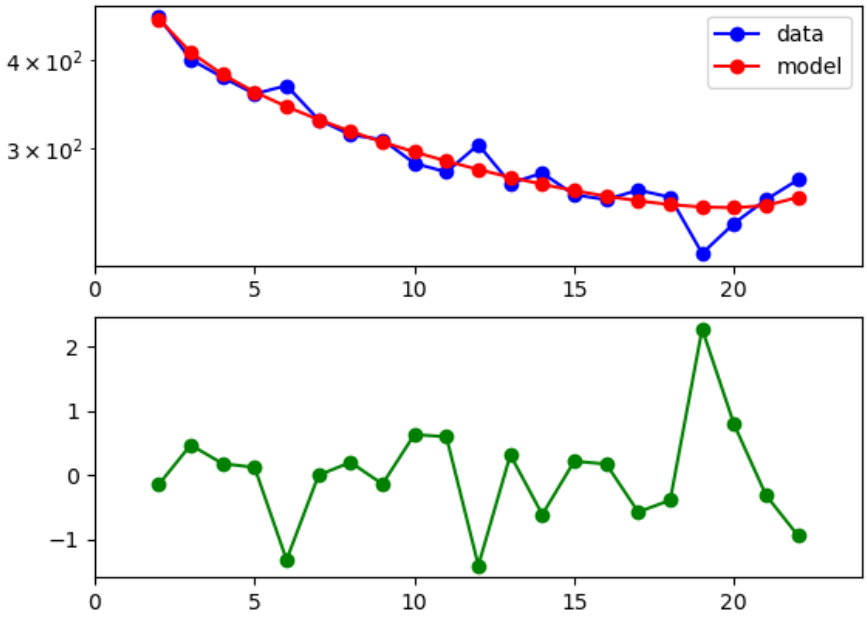

Fig. S51 Model fit to the AFS using synonymous SNPs from GBB. The blue line shows the observed AFS from the data, the red line shows the inferred AFS based on the maximum likelihood estimates in Additional File 2: Table S88, and the green line shows the residual between the observed and model AFS.

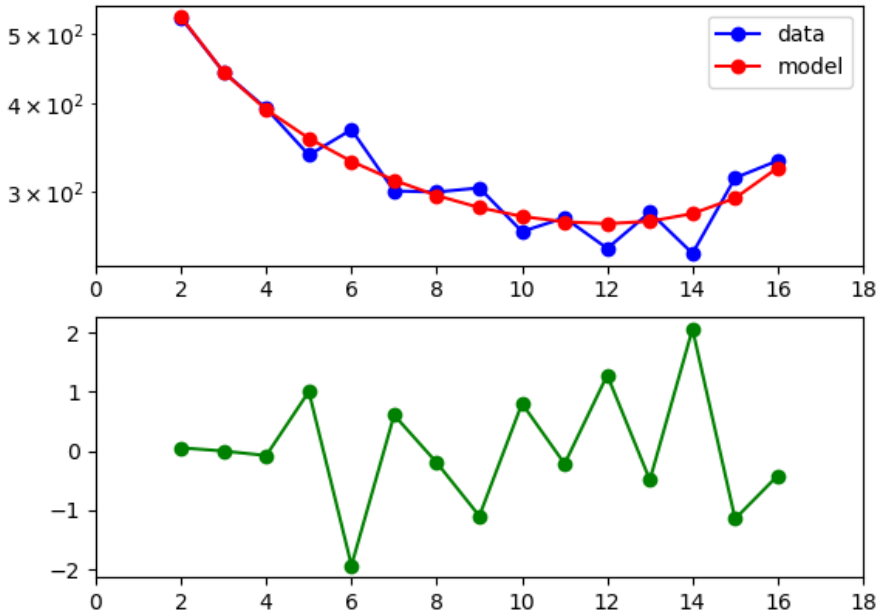

Fig. S52 Model fit to the AFS using synonymous SNPs from GBG. The blue line shows the observed AFS from the data, the red line shows the inferred AFS based on the maximum likelihood estimates in Additional File 2: Table S88, and the green line shows the residual between the observed and model AFS.

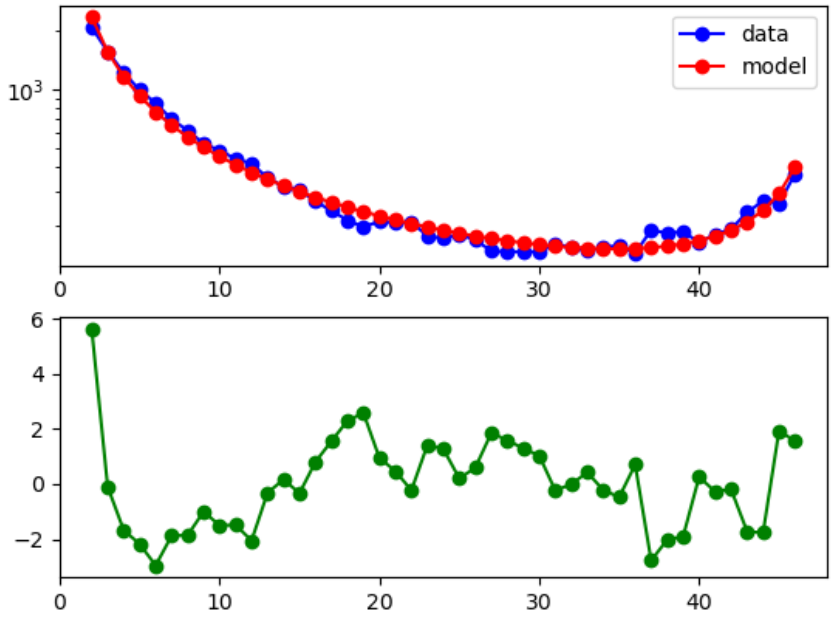

Fig. S53 Model fit to the AFS using synonymous SNPs from GGG. The blue line shows the observed AFS from the data, the red line shows the inferred AFS based on the maximum likelihood estimates in Additional File 2: Table S88, and the green line shows the residual between the observed and model AFS.

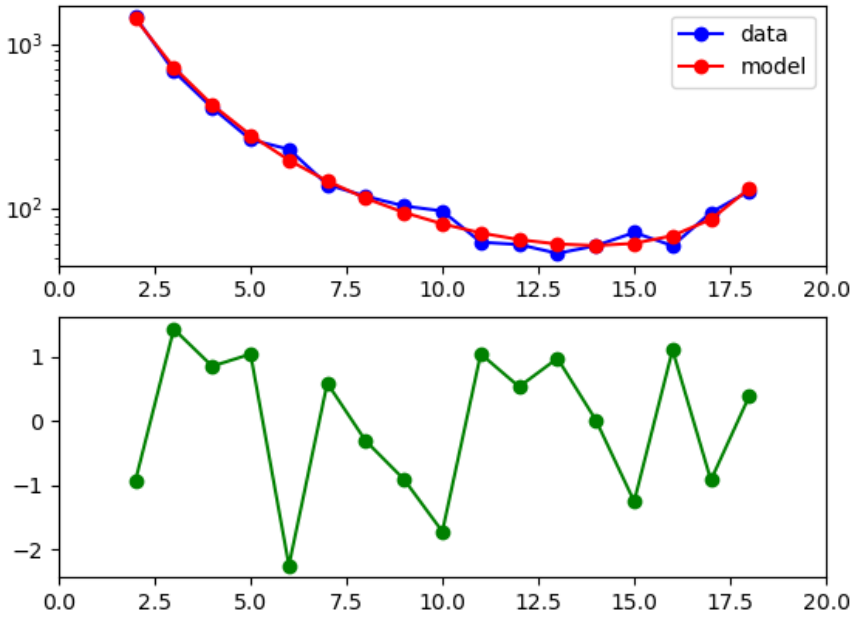

Fig. S54 Model fit to the AFS using non-synonymous SNPs from PPA. The blue line shows the observed AFS from the data, the red line shows the inferred AFS based on the maximum likelihood estimates in Fig. 3 and Additional File 2: Table S88, and the green line shows the residual between the observed and model AFS.

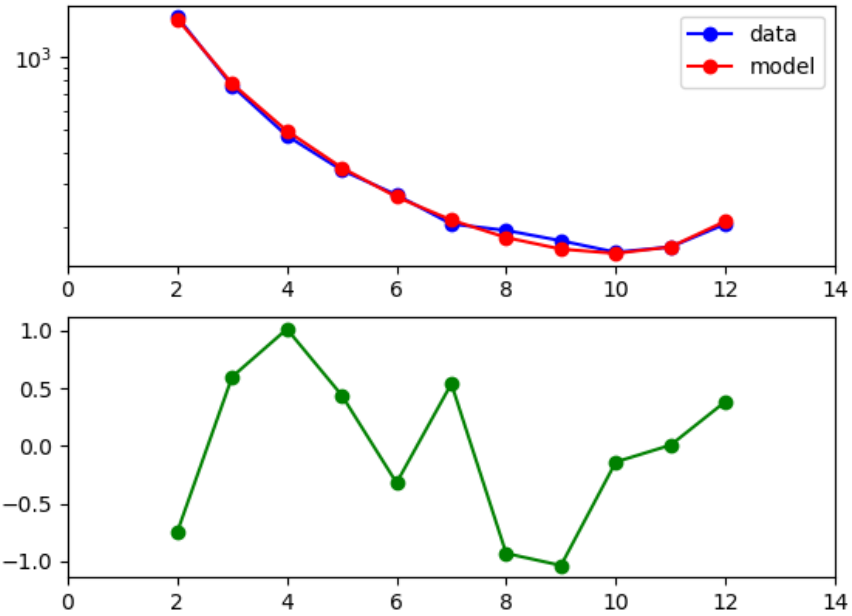

Fig. S55 Model fit to the AFS using non-synonymous SNPs from PTE. The blue line shows the observed AFS from the data, the red line shows the inferred AFS based on the maximum likelihood estimates in Fig. 3 and Additional File 2: Table S88, and the green line shows the residual between the observed and model AFS.

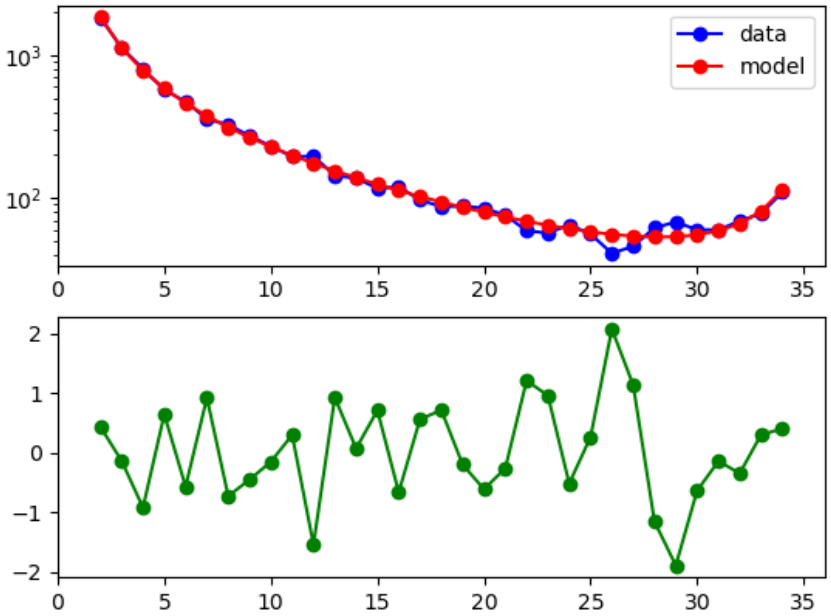

Fig. S56 Model fit to the AFS using non-synonymous SNPs from PTS. The blue line shows the observed AFS from the data, the red line shows the inferred AFS based on the maximum likelihood estimates in Fig. 3 and Additional File 2: Table S88, and the green line shows the residual between the observed and model AFS.

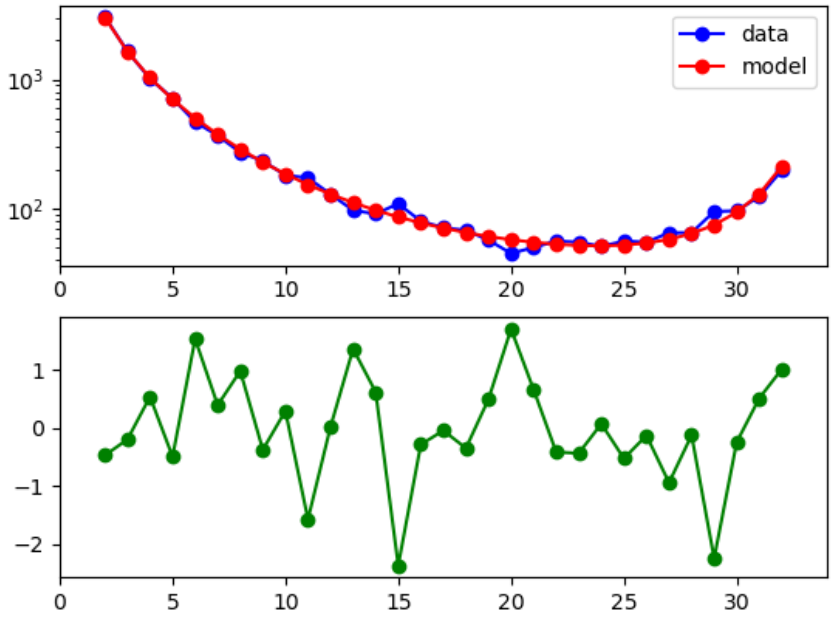

Fig. S57 Model fit to the AFS using non-synonymous SNPs from PTT. The blue line shows the observed AFS from the data, the red line shows the inferred AFS based on the maximum likelihood estimates in Fig. 3 and Additional File 2: Table S88, and the green line shows the residual between the observed and model AFS.

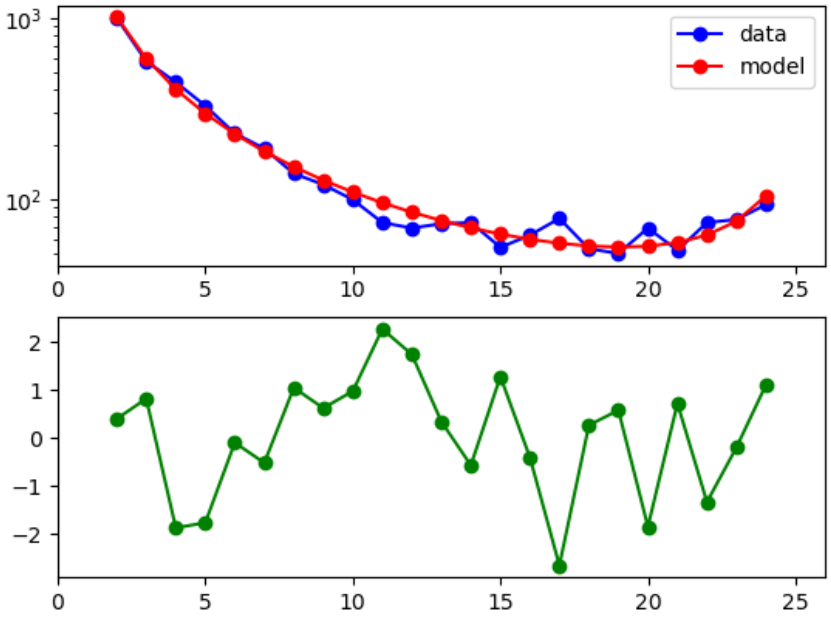

Fig. S58 Model fit to the AFS using non-synonymous SNPs from PTV. The blue line shows the observed AFS from the data, the red line shows the inferred AFS based on the maximum likelihood estimates in Fig. 3 and Additional File 2: Table S88, and the green line shows the residual between the observed and model AFS.

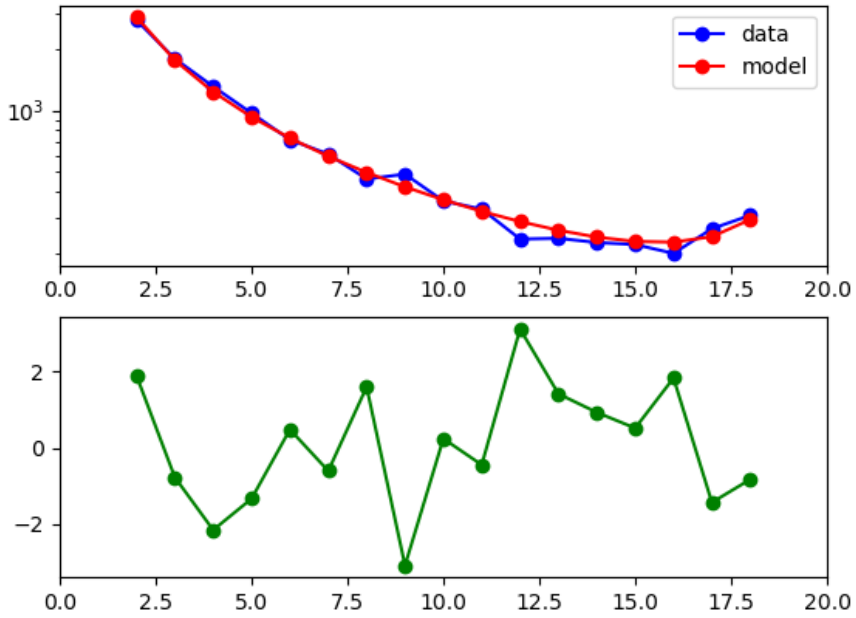

Fig. S59 Model fit to the AFS using non-synonymous SNPs from PA. The blue line shows the observed AFS from the data, the red line shows the inferred AFS based on the maximum likelihood estimates in Fig. 3 and Additional File 2: Table S88, and the green line shows the residual between the observed and model AFS.

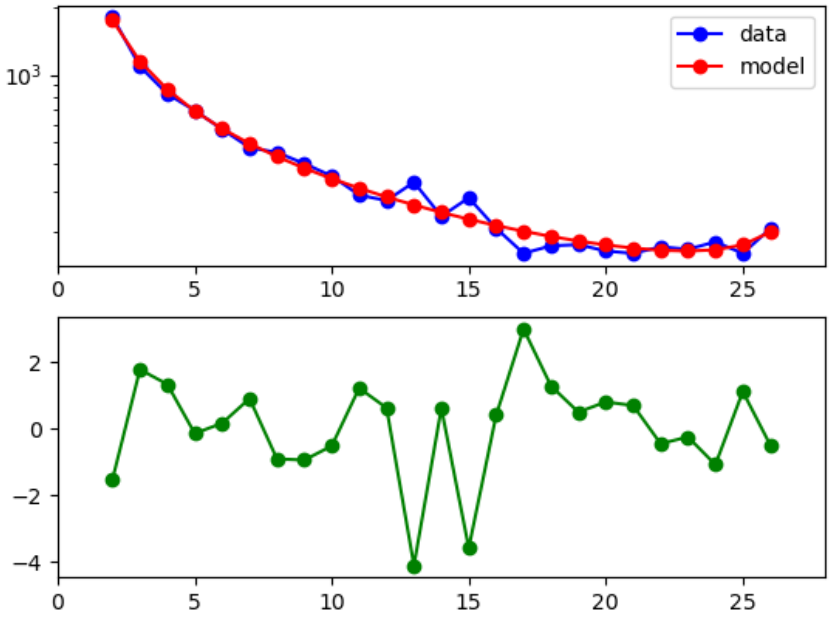

Fig. S60 Model fit to the AFS using non-synonymous SNPs from PP. The blue line shows the observed AFS from the data, the red line shows the inferred AFS based on the maximum likelihood estimates in Fig. 3 and Additional File 2: Table S88, and the green line shows the residual between the observed and model AFS.

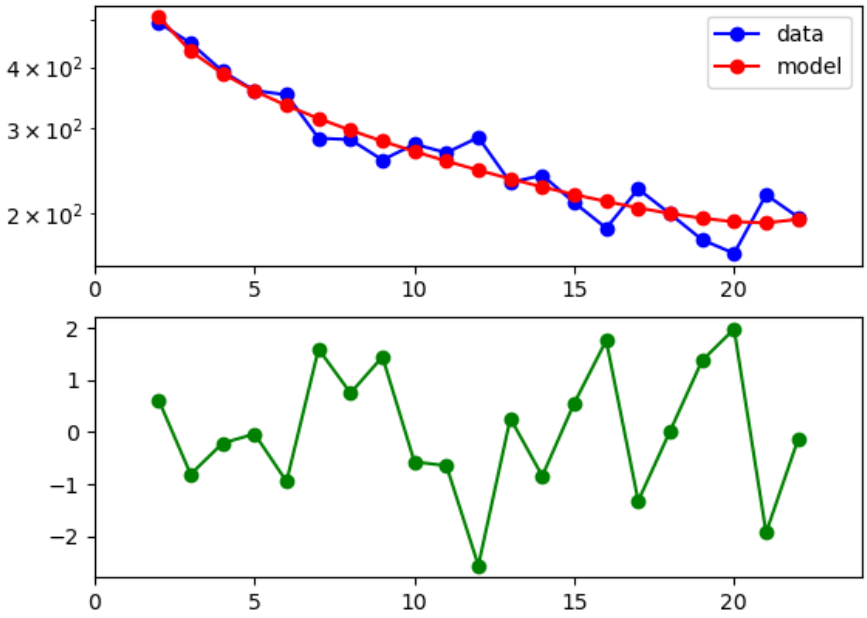

Fig. S61 Model fit to the AFS using non-synonymous SNPs from GBB. The blue line shows the observed AFS from the data, the red line shows the inferred AFS based on the maximum likelihood estimates in Fig. 3 and Additional File 2: Table S88, and the green line shows the residual between the observed and model AFS.

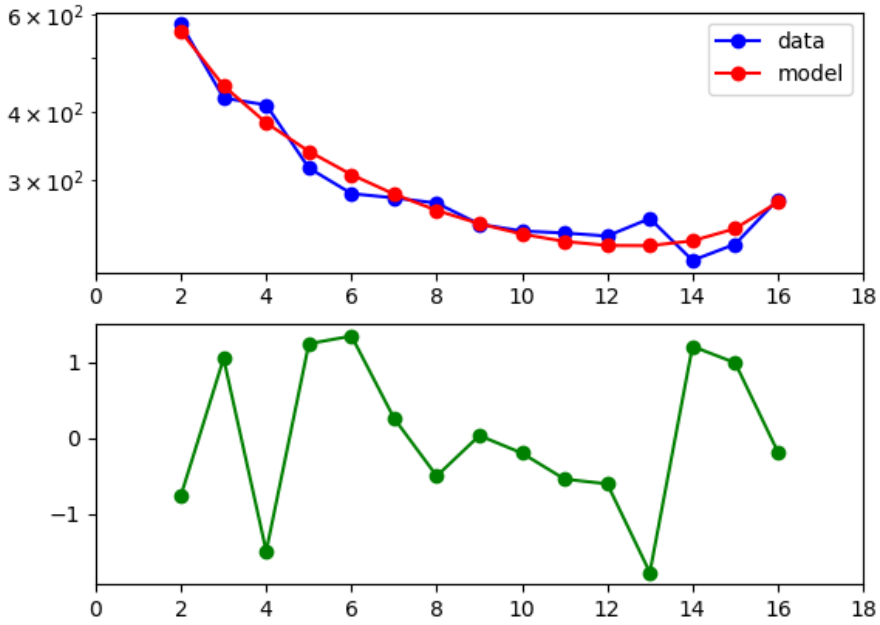

Fig. S62 Model fit to the AFS using non-synonymous SNPs from GBG. The blue line shows the observed AFS from the data, the red line shows the inferred AFS based on the maximum likelihood estimates in Fig. 3 and Additional File 2: Table S88, and the green line shows the residual between the observed and model AFS.

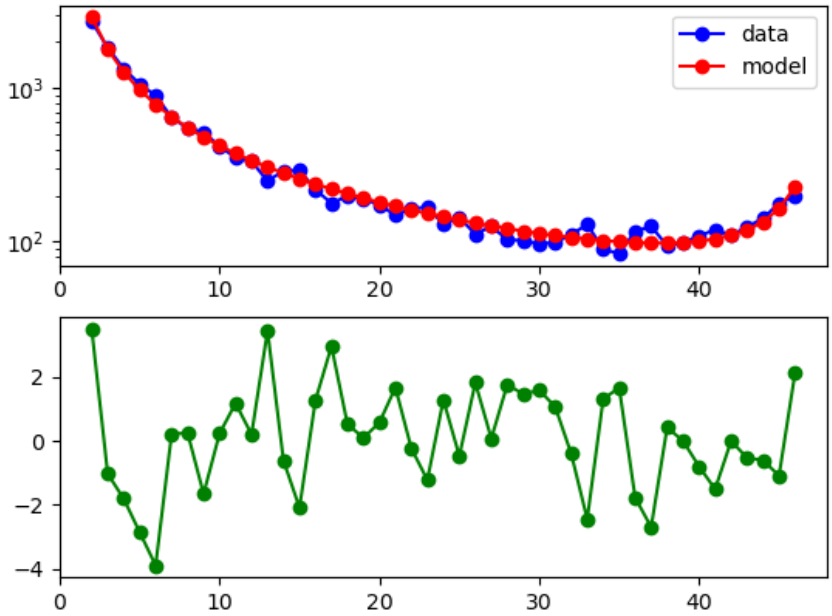

Fig. S63 Model fit to the AFS using non-synonymous SNPs from GGG. The blue line shows the observed AFS from the data, the red line shows the inferred AFS based on the maximum likelihood estimates in Fig. 3 and Additional File 2: Table S88, and the green line shows the residual between the observed and model AFS.

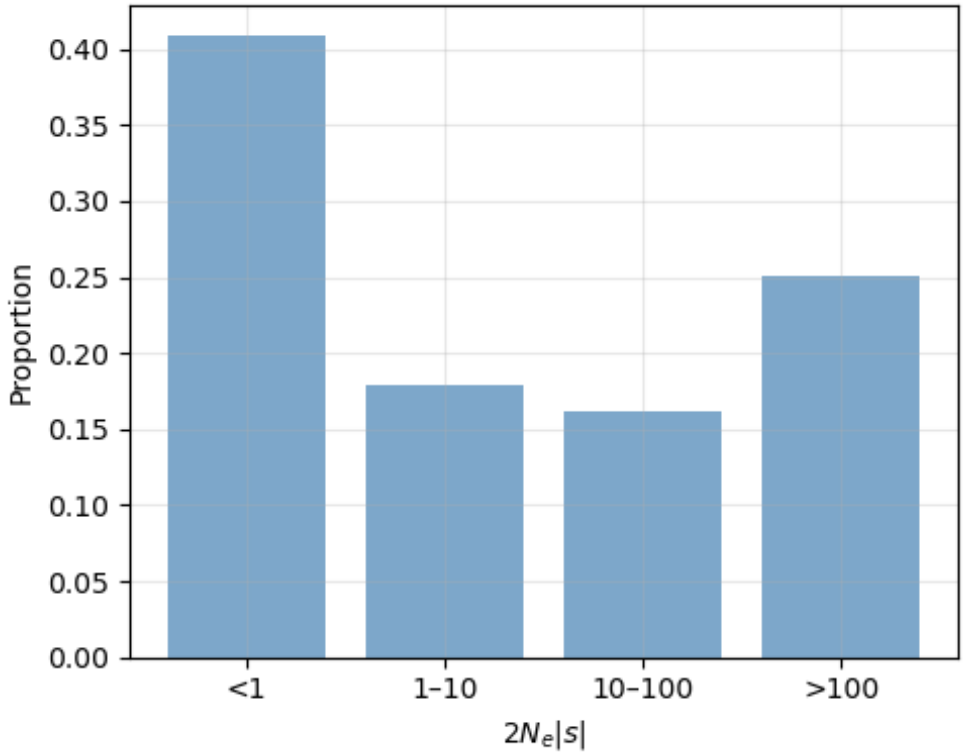

Fig. S64 Proportions of deleterious mutations in PPA, inferred from non-synonymous SNPs using the DFE model based on the maximum likelihood estimates in Fig. 3.

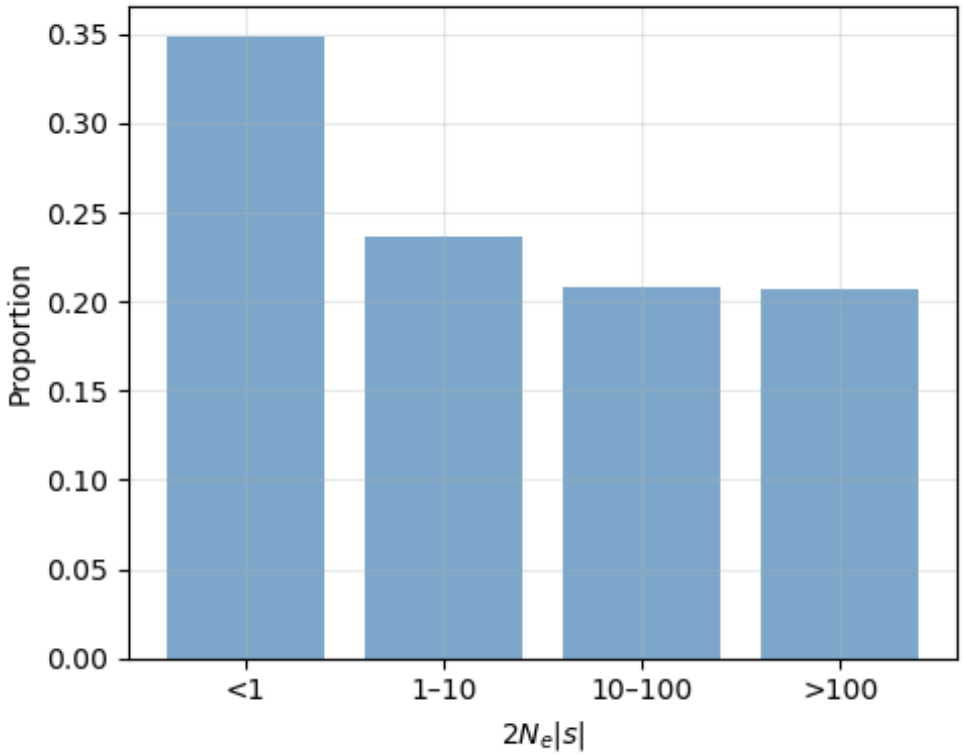

Fig. S65 Proportions of deleterious mutations in PTE, inferred from non-synonymous SNPs using the DFE model based on the maximum likelihood estimates in Fig. 3.

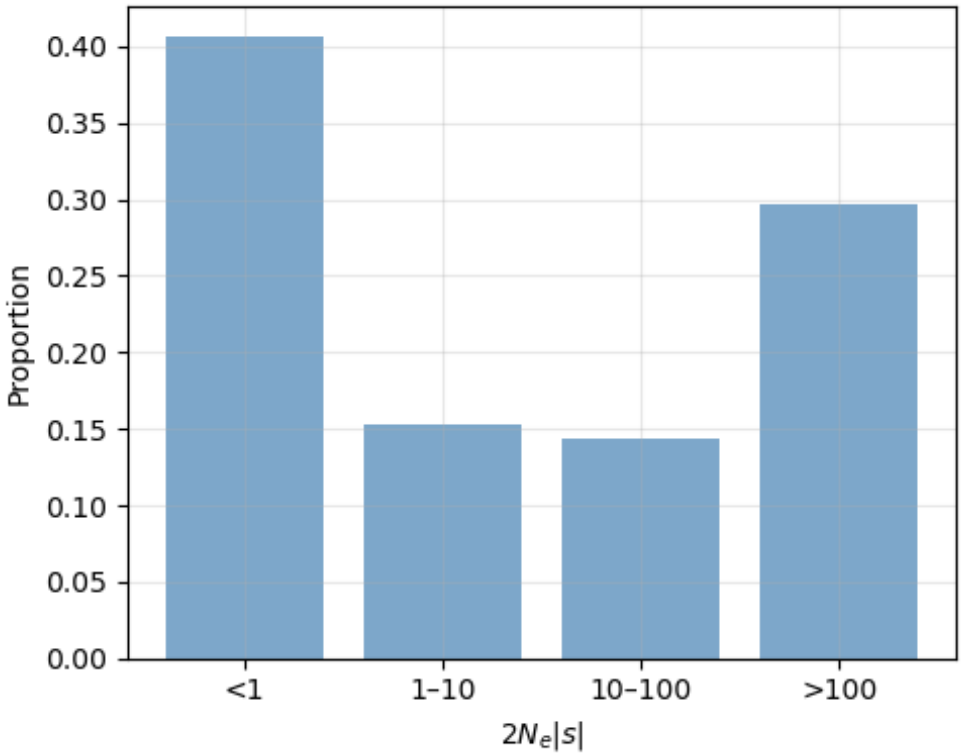

Fig. S66 Proportions of deleterious mutations in PTS, inferred from non-synonymous SNPs using the DFE model based on the maximum likelihood estimates in Fig. 3.

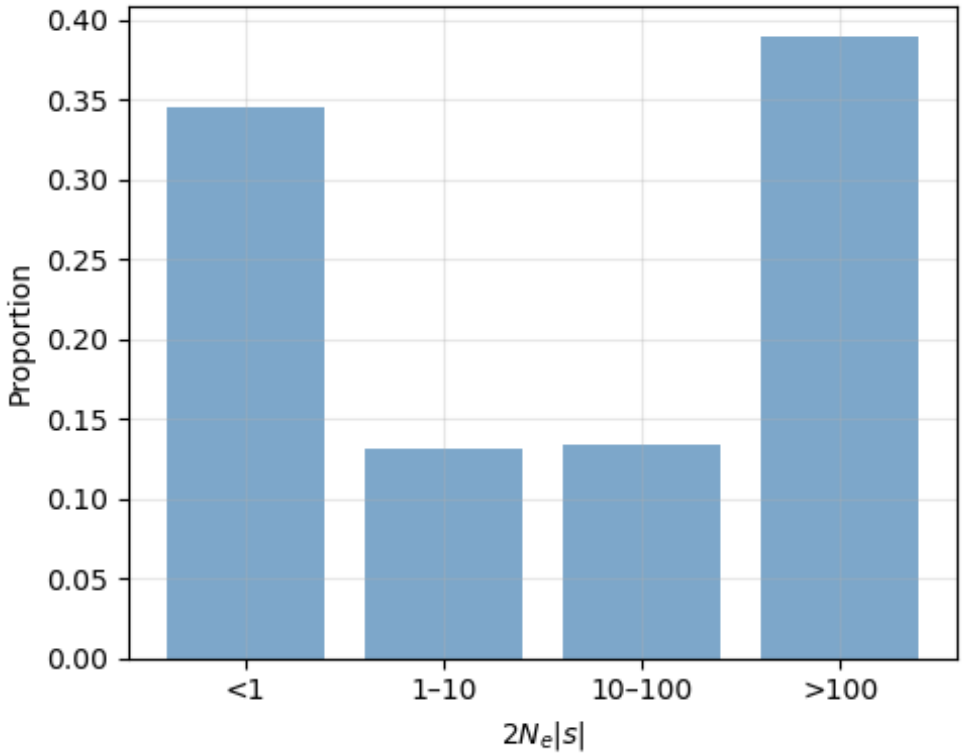

Fig. S67 Proportions of deleterious mutations in PTT, inferred from non-synonymous SNPs using the DFE model based on the maximum likelihood estimates in Fig. 3.

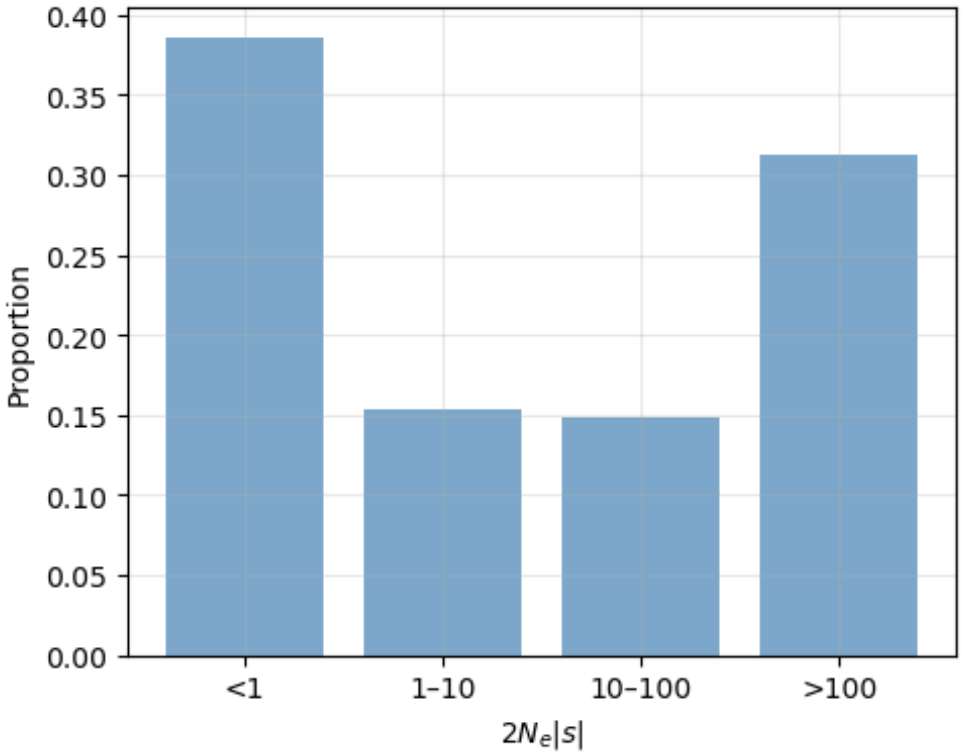

Fig. S68 Proportions of deleterious mutations in PTV, inferred from non-synonymous SNPs using the DFE model based on the maximum likelihood estimates in Fig. 3.

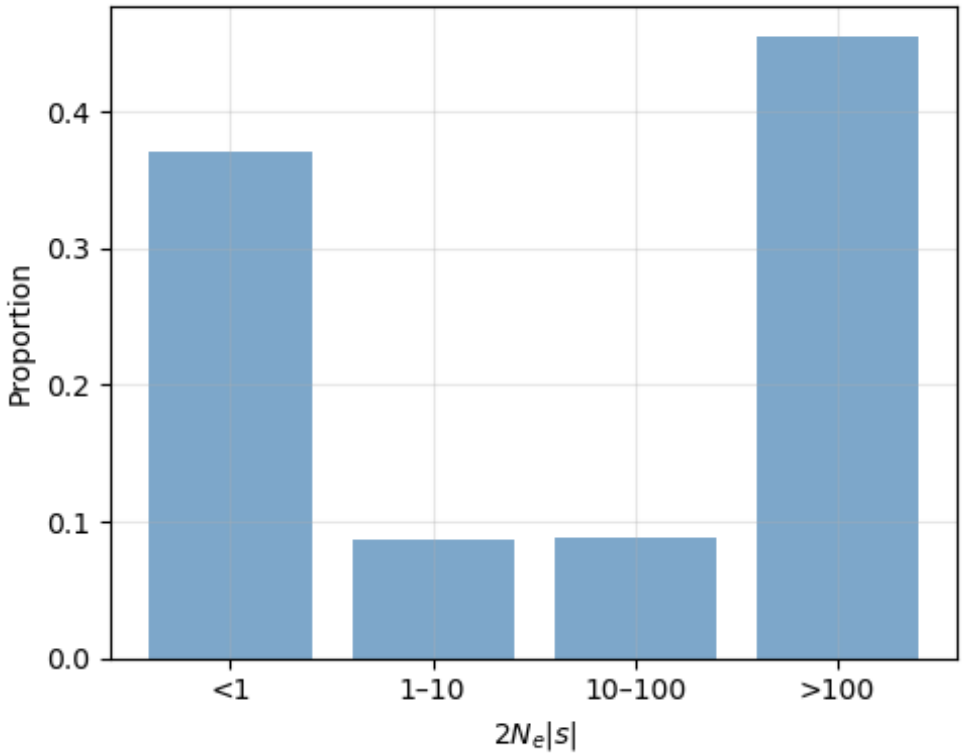

Fig. S69 Proportions of deleterious mutations in PA, inferred from non-synonymous SNPs using the DFE model based on the maximum likelihood estimates in Fig. 3.

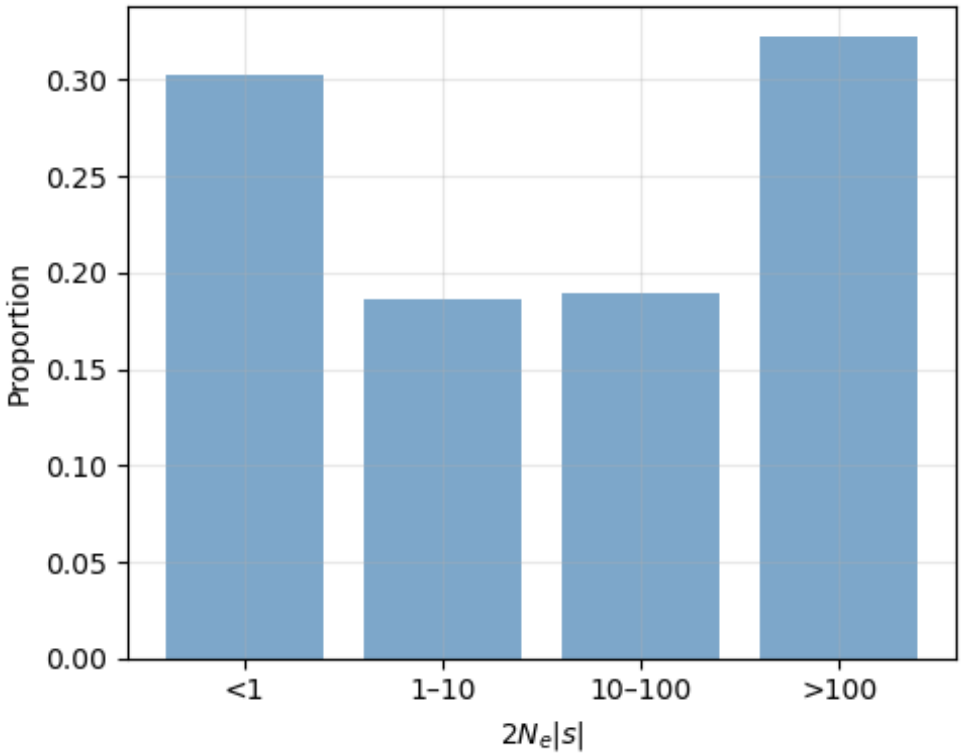

Fig. S70 Proportions of deleterious mutations in PP, inferred from non-synonymous SNPs using the DFE model based on the maximum likelihood estimates in Fig. 3.

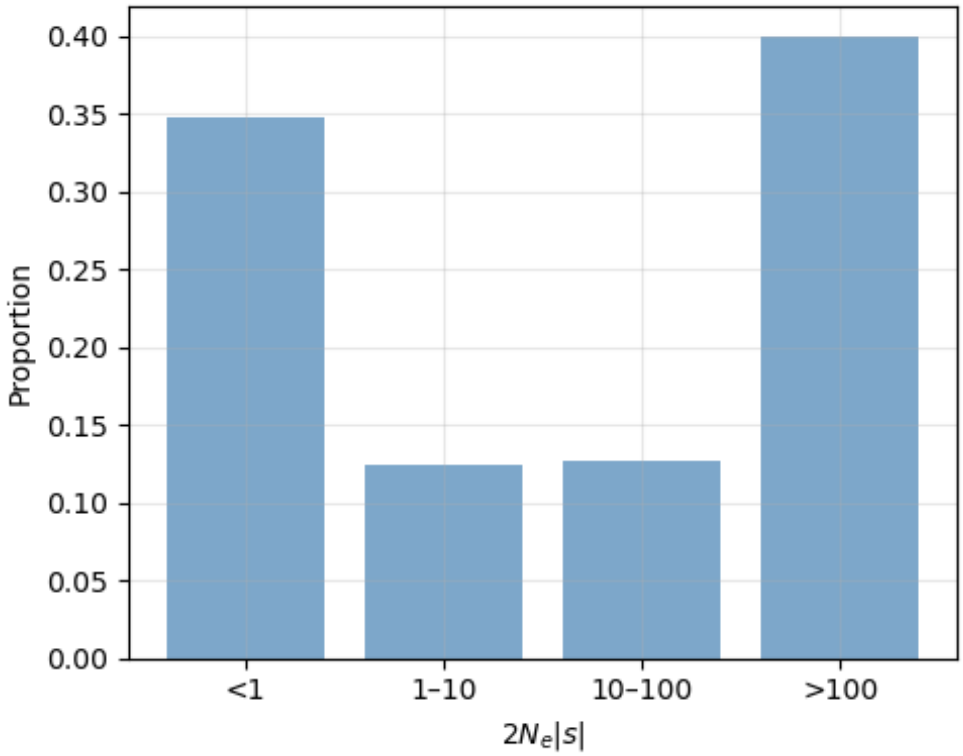

Fig. S71 Proportions of deleterious mutations in GBB, inferred from non-synonymous SNPs using the DFE model based on the maximum likelihood estimates in Fig. 3.

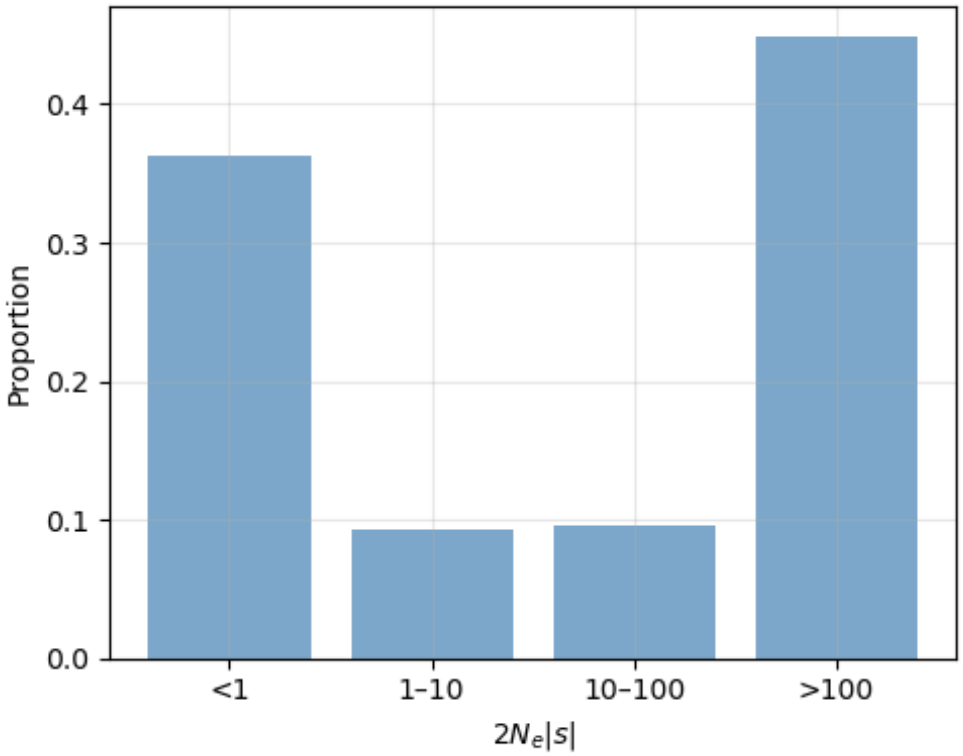

Fig. S72 Proportions of deleterious mutations in GBG, inferred from non-synonymous SNPs using the DFE model based on the maximum likelihood estimates in Fig. 3.

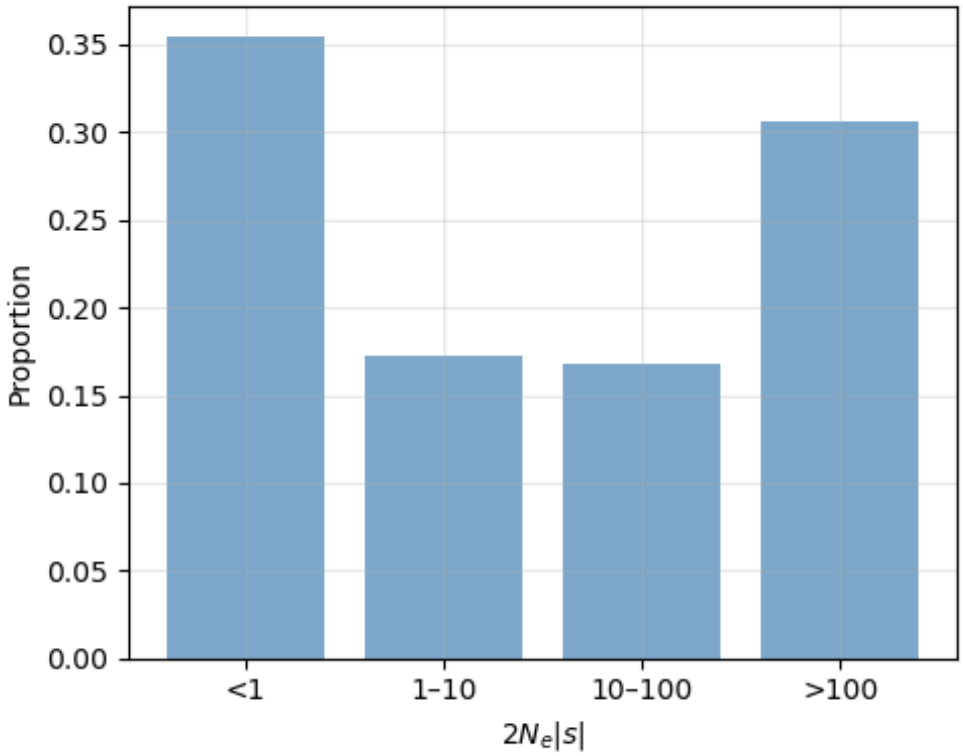

Fig. S73 Proportions of deleterious mutations in GGG, inferred from non-synonymous SNPs using the DFE model based on the maximum likelihood estimates in Fig. 3.

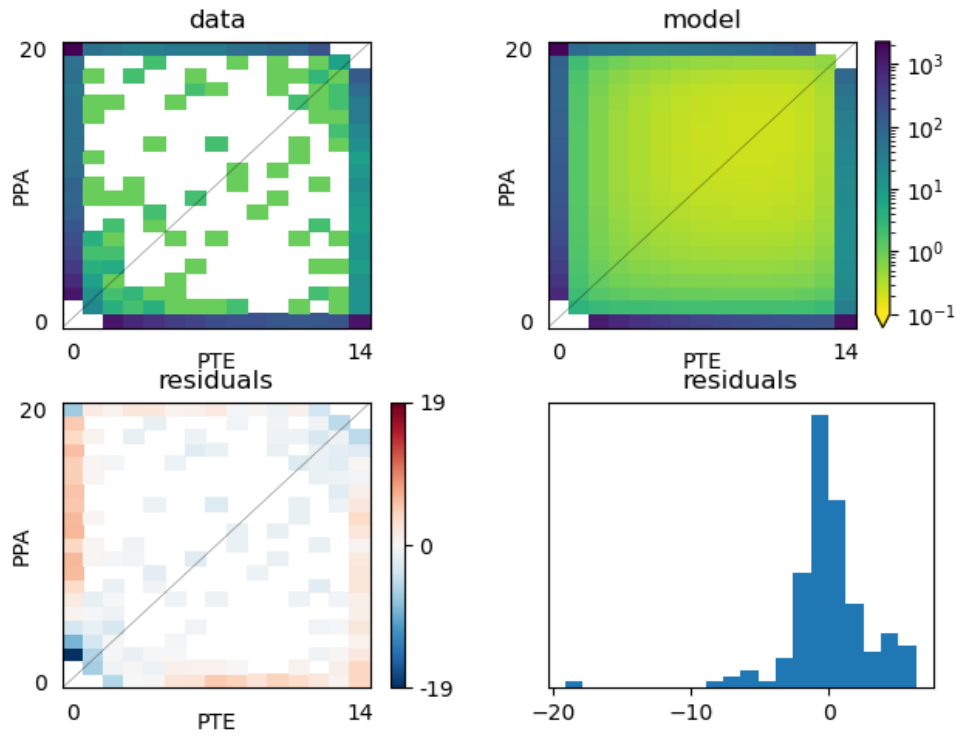

Fig. S74 Model fit to the joint AFS using synonymous SNPs from PPA and PTE. The upper left panel shows the observed joint AFS, the upper right panel shows the inferred AFS based on the maximum likelihood estimates in Additional File 2: Table S89, and the remaining panels show the residuals between the observed and model AFS.

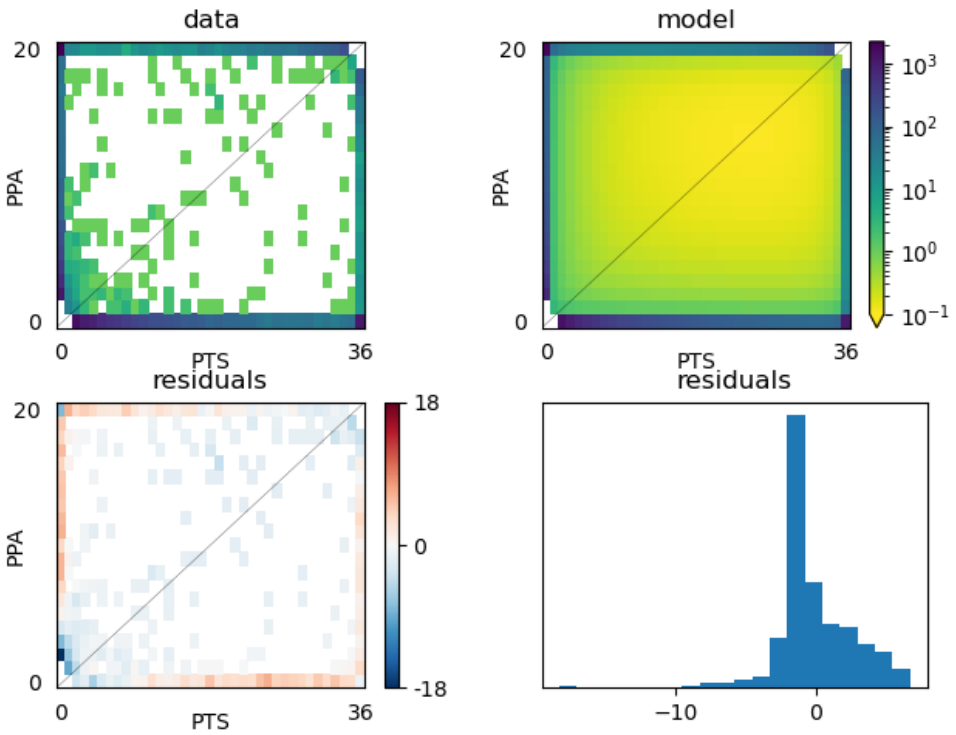

Fig. S75 Model fit to the joint AFS using synonymous SNPs from PPA and PTS. The upper left panel shows the observed joint AFS, the upper right panel shows the inferred AFS based on the maximum likelihood estimates in Additional File 2: Table S89, and the remaining panels show the residuals between the observed and model AFS.

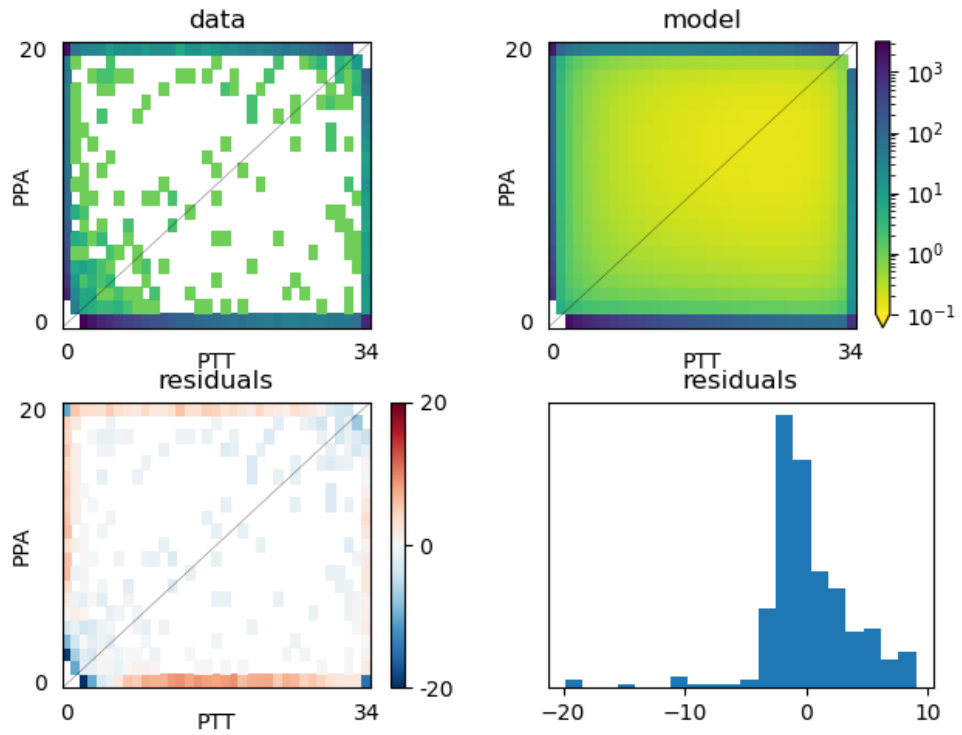

Fig. S76 Model fit to the joint AFS using synonymous SNPs from PPA and PTT. The upper left panel shows the observed joint AFS, the upper right panel shows the inferred AFS based on the maximum likelihood estimates in Additional File 2: Table S89, and the remaining panels show the residuals between the observed and model AFS.

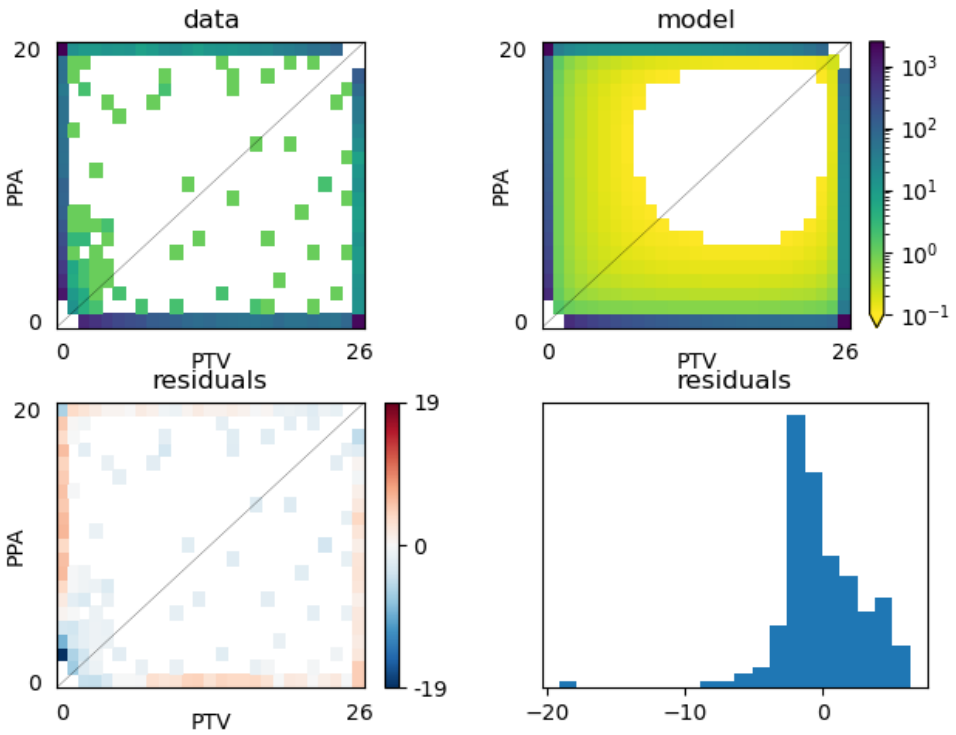

Fig. S77 Model fit to the joint AFS using synonymous SNPs from PPA and PTV. The upper left panel shows the observed joint AFS, the upper right panel shows the inferred AFS based on the maximum likelihood estimates in Additional File 2: Table S89, and the remaining panels show the residuals between the observed and model AFS.

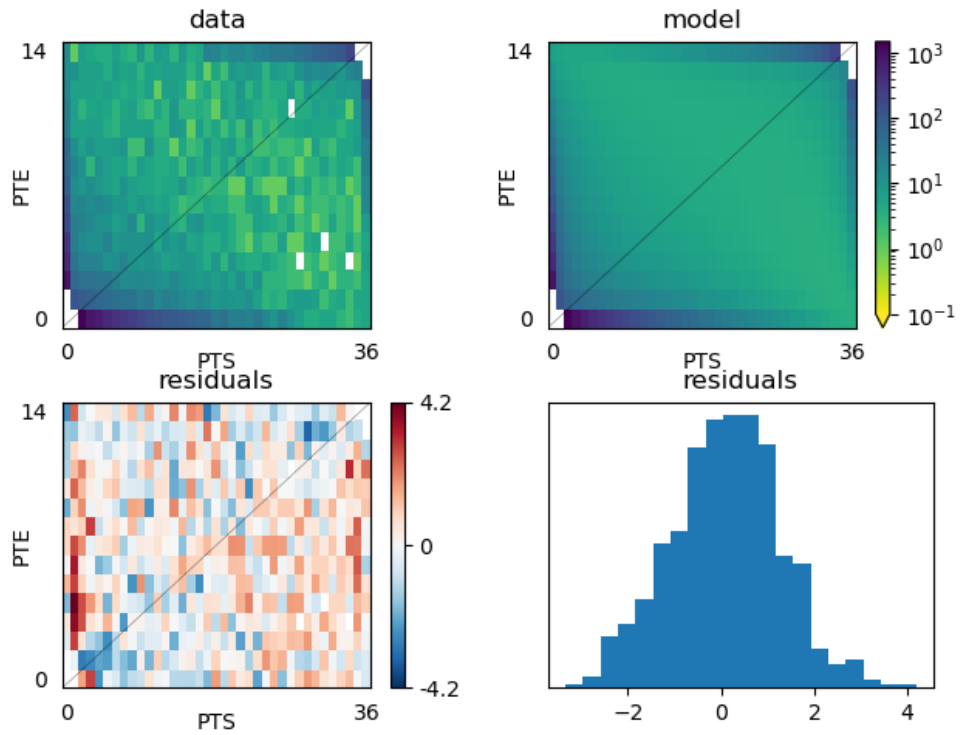

Fig. S78 Model fit to the joint AFS using synonymous SNPs from PTE and PTS. The upper left panel shows the observed joint AFS, the upper right panel shows the inferred AFS based on the maximum likelihood estimates in Additional File 2: Table S89, and the remaining panels show the residuals between the observed and model AFS.

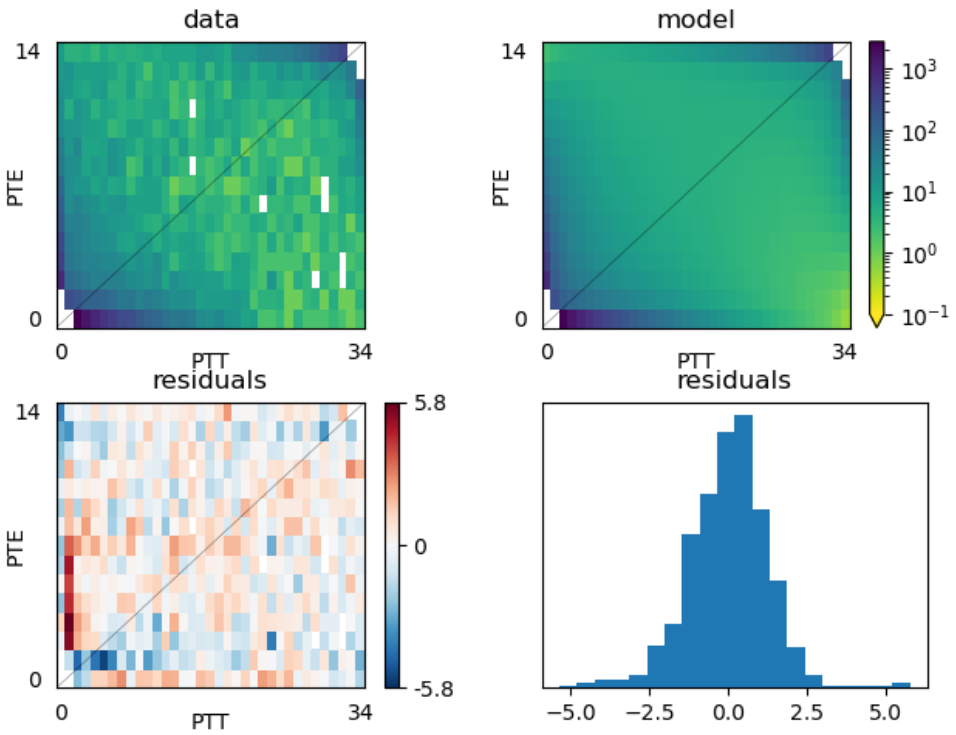

Fig. S79 Model fit to the joint AFS using synonymous SNPs from PTE and PTT. The upper left panel shows the observed joint AFS, the upper right panel shows the inferred AFS based on the maximum likelihood estimates in Additional File 2: Table S89, and the remaining panels show the residuals between the observed and model AFS.

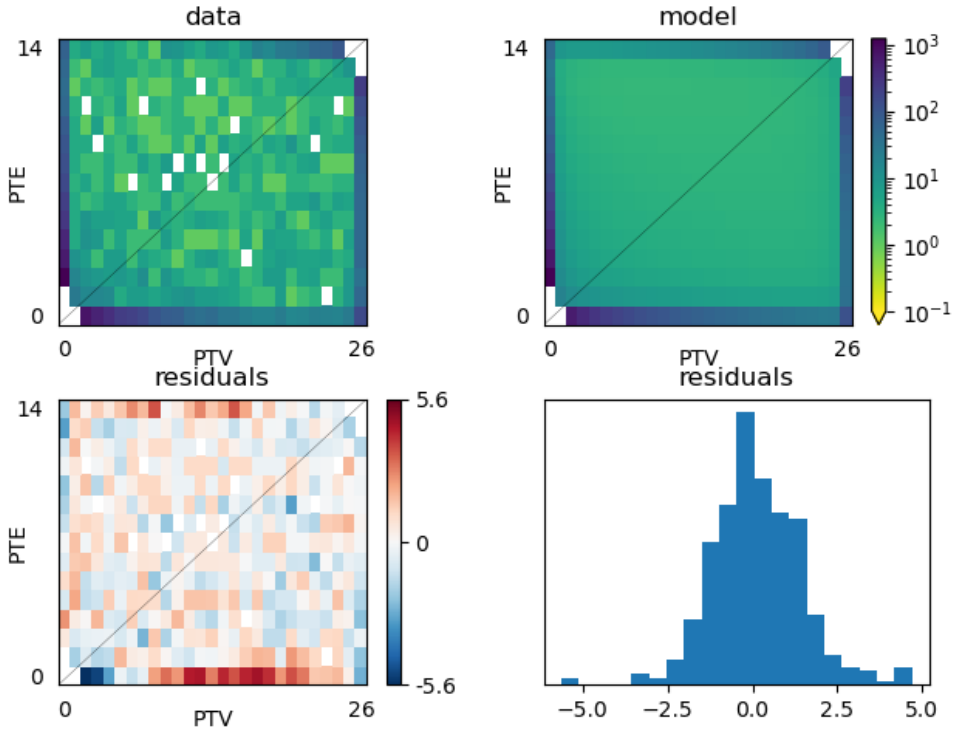

Fig. S80 Model fit to the joint AFS using synonymous SNPs from PTE and PTV. The upper left panel shows the observed joint AFS, the upper right panel shows the inferred AFS based on the maximum likelihood estimates in Additional File 2: Table S89, and the remaining panels show the residuals between the observed and model AFS.

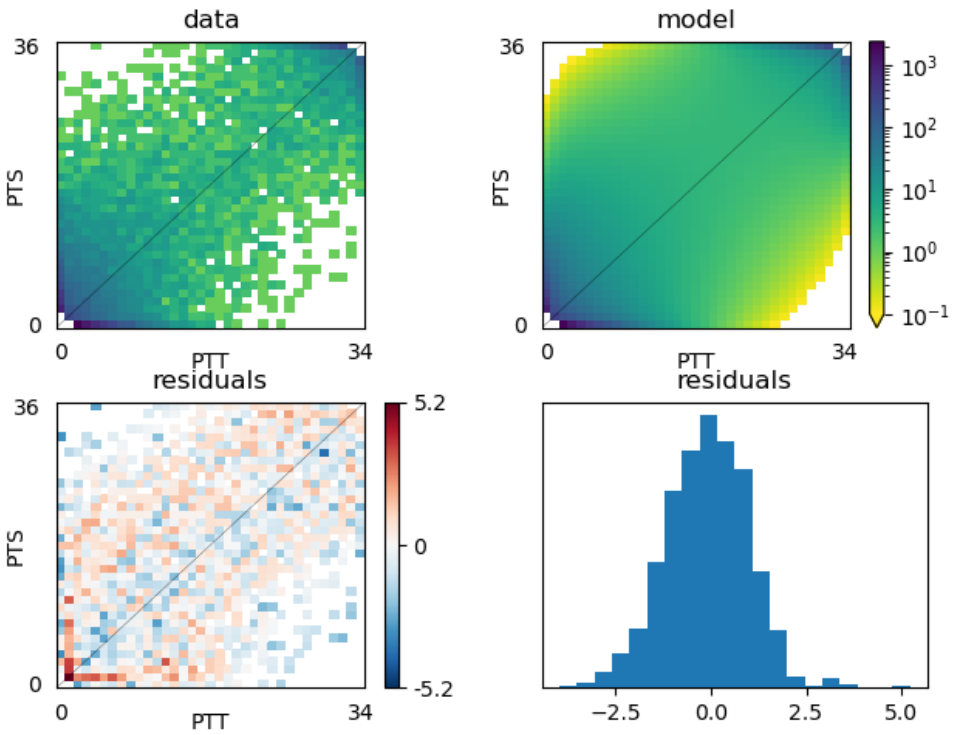

Fig. S81 Model fit to the joint AFS using synonymous SNPs from PTS and PTT. The upper left panel shows the observed joint AFS, the upper right panel shows the inferred AFS based on the maximum likelihood estimates in Additional File 2: Table S89, and the remaining panels show the residuals between the observed and model AFS.

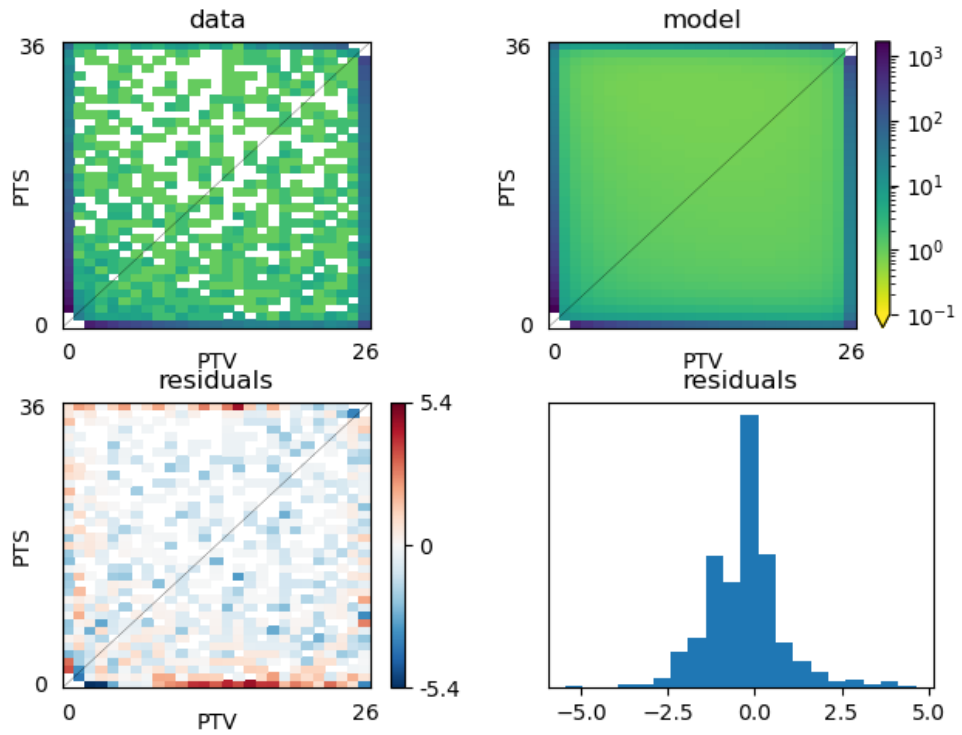

Fig. S82 Model fit to the joint AFS using synonymous SNPs from PTS and PTV. The upper left panel shows the observed joint AFS, the upper right panel shows the inferred AFS based on the maximum likelihood estimates in Additional File 2: Table S89, and the remaining panels show the residuals between the observed and model AFS.

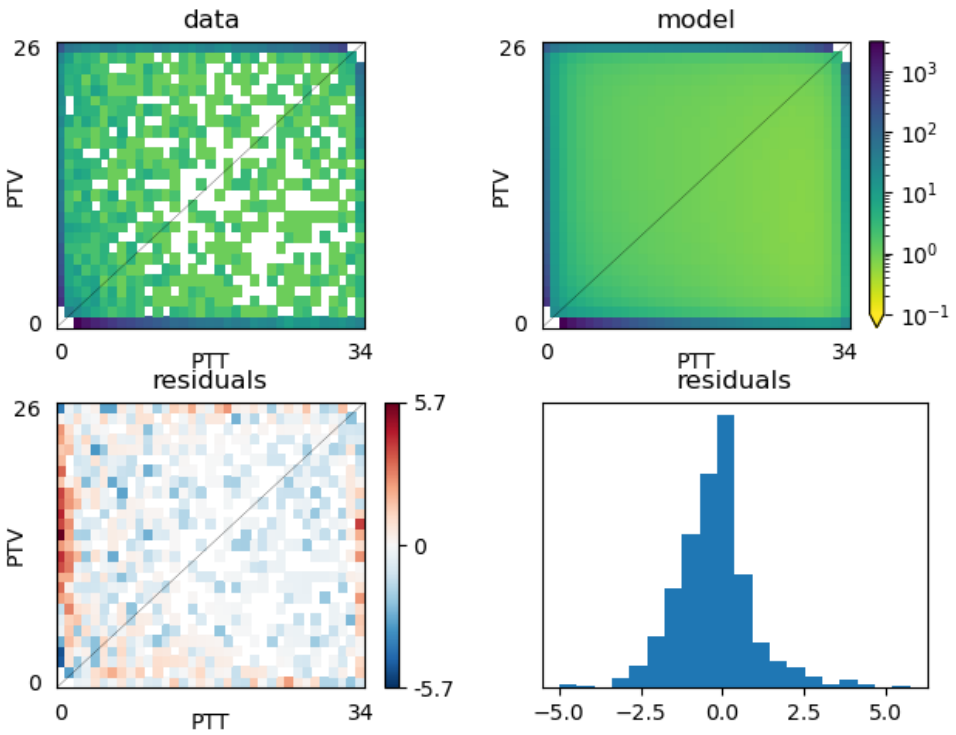

Fig. S83 Model fit to the joint AFS using synonymous SNPs from PTT and PTV. The upper left panel shows the observed joint AFS, the upper right panel shows the inferred AFS based on the maximum likelihood estimates in Additional File 2: Table S89, and the remaining panels show the residuals between the observed and model AFS.

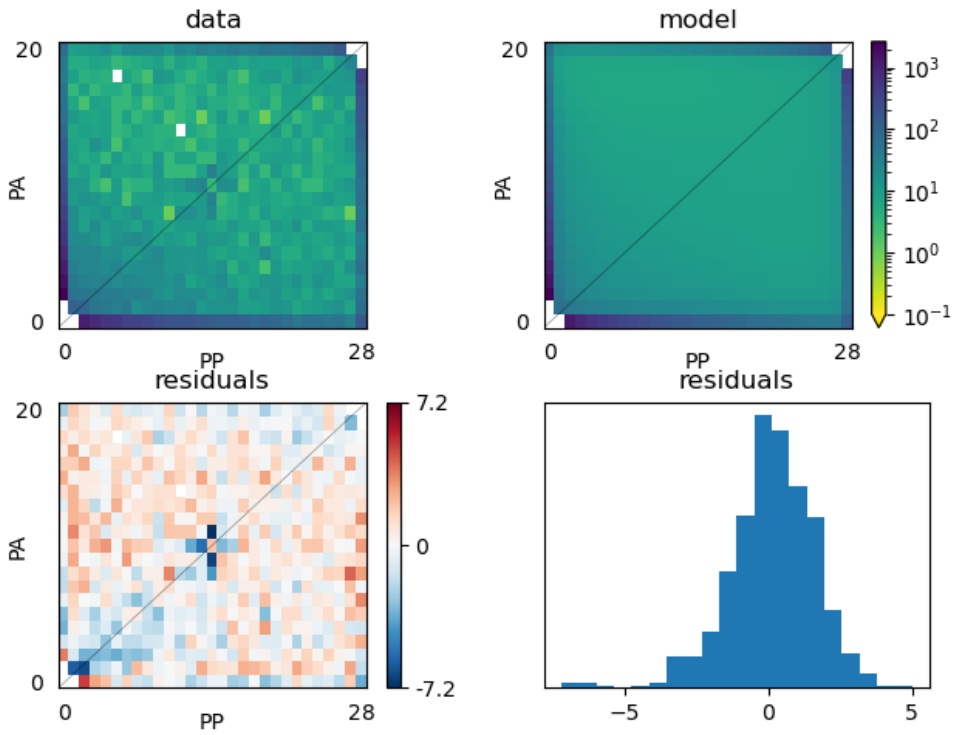

Fig. S84 Model fit to the joint AFS using synonymous SNPs from PA and PP. The upper left panel shows the observed joint AFS, the upper right panel shows the inferred AFS based on the maximum likelihood estimates in Additional File 2: Table S89, and the remaining panels show the residuals between the observed and model AFS.

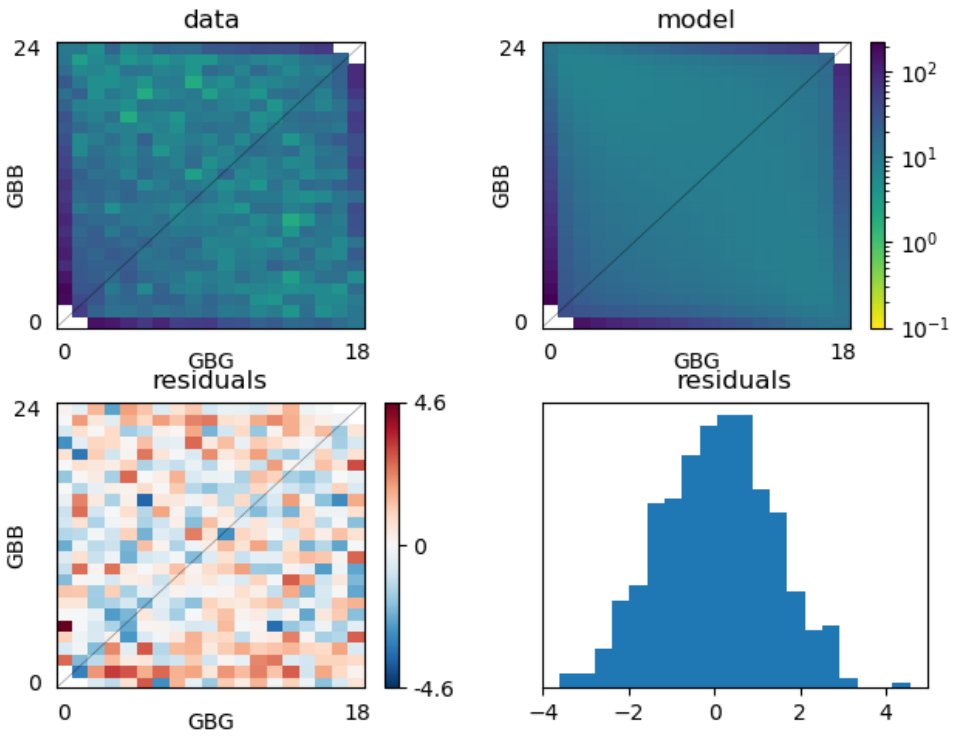

Fig. S85 Model fit to the joint AFS using synonymous SNPs from GBB and GBG. The upper left panel shows the observed joint AFS, the upper right panel shows the inferred AFS based on the maximum likelihood estimates in Additional File 2: Table S89, and the remaining panels show the residuals between the observed and model AFS.

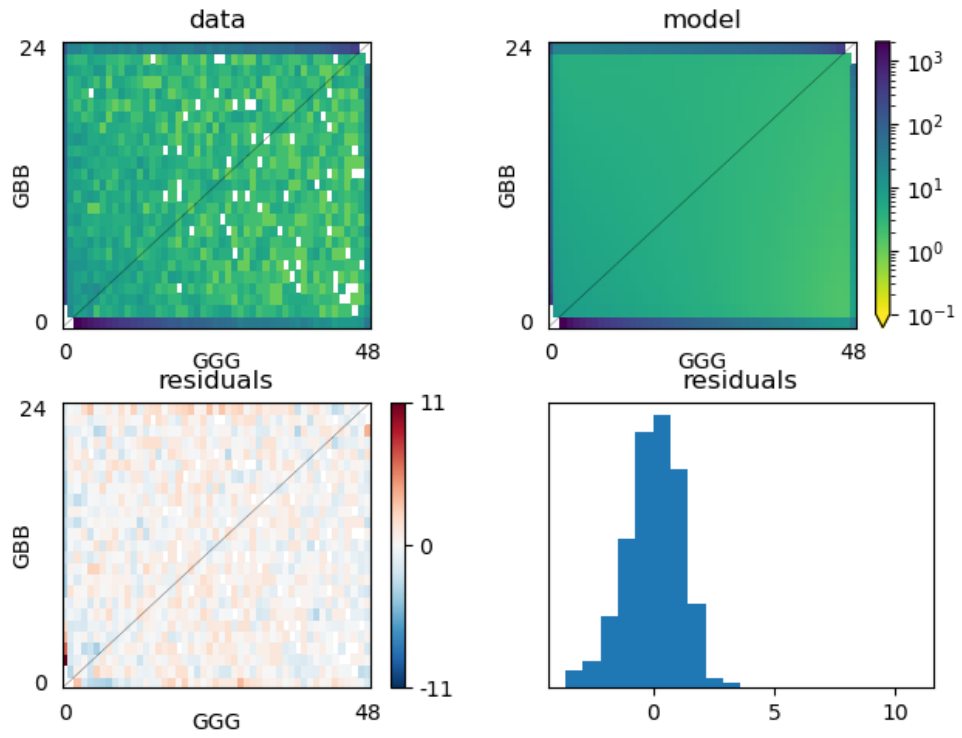

Fig. S86 Model fit to the joint AFS using synonymous SNPs from GBB and GBG. The upper left panel shows the observed joint AFS, the upper right panel shows the inferred AFS based on the maximum likelihood estimates in Additional File 2: Table S89, and the remaining panels show the residuals between the observed and model AFS.

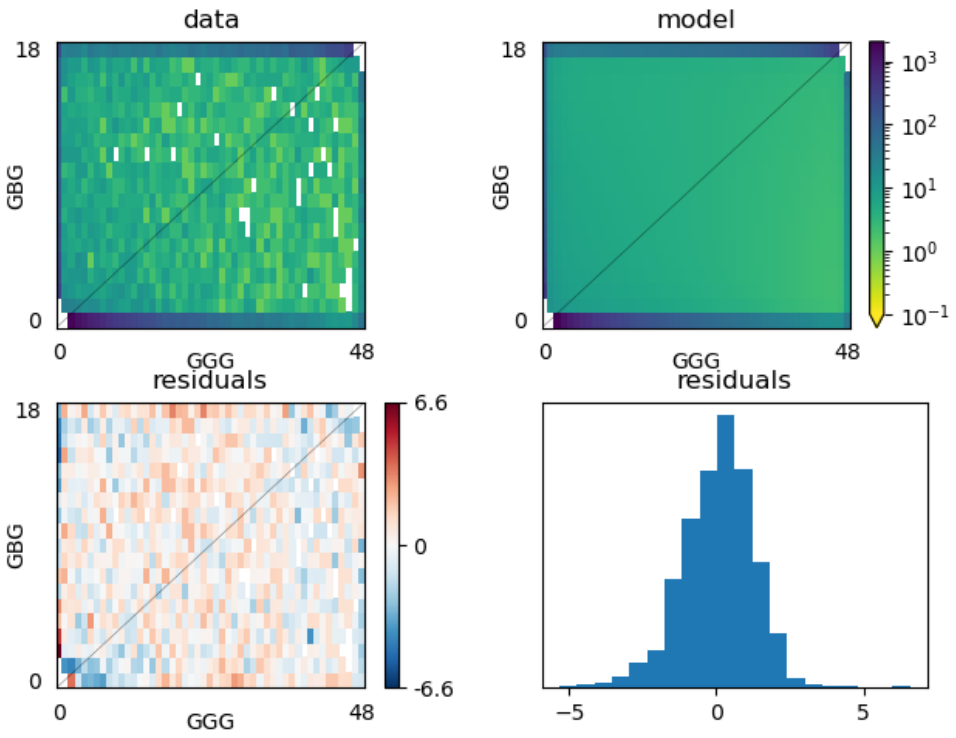

Fig. S87 Model fit to the joint AFS using synonymous SNPs from GBB and GBG. The upper left panel shows the observed joint AFS, the upper right panel shows the inferred AFS based on the maximum likelihood estimates in Additional File 2: Table S89, and the remaining panels show the residuals between the observed and model AFS.

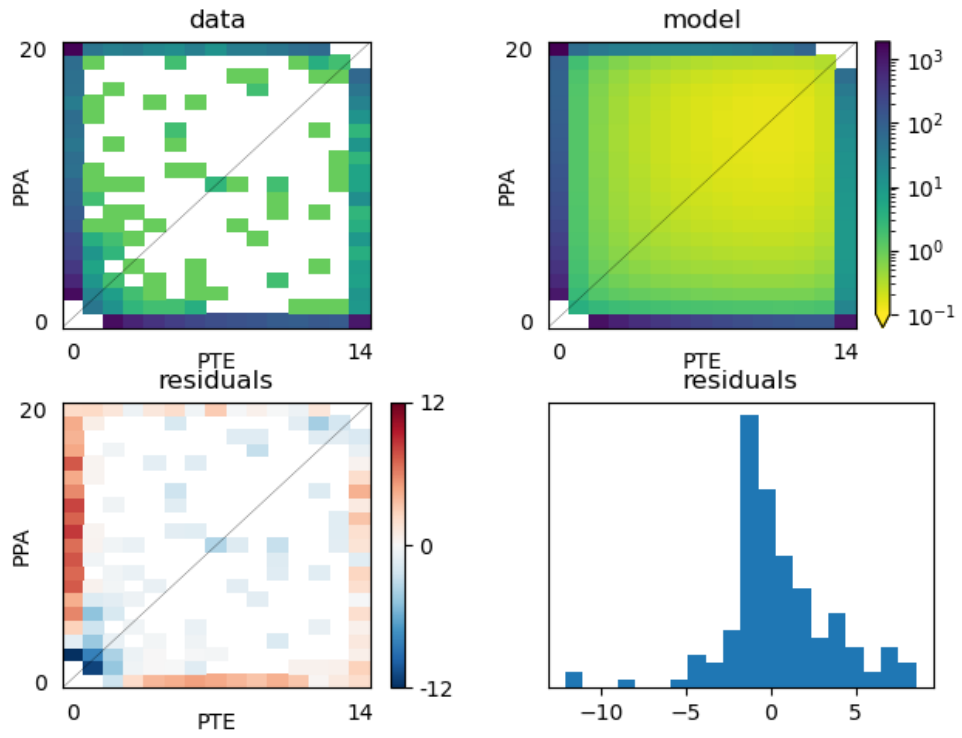

Fig. S88 Model fit to the joint AFS using non-synonymous SNPs from PPA and PTE. The upper left panel shows the observed joint AFS, the upper right panel shows the inferred AFS based on the maximum likelihood estimates in Fig. 3 and Additional File 2: Table S89, and the remaining panels show the residuals between the observed and model AFS.

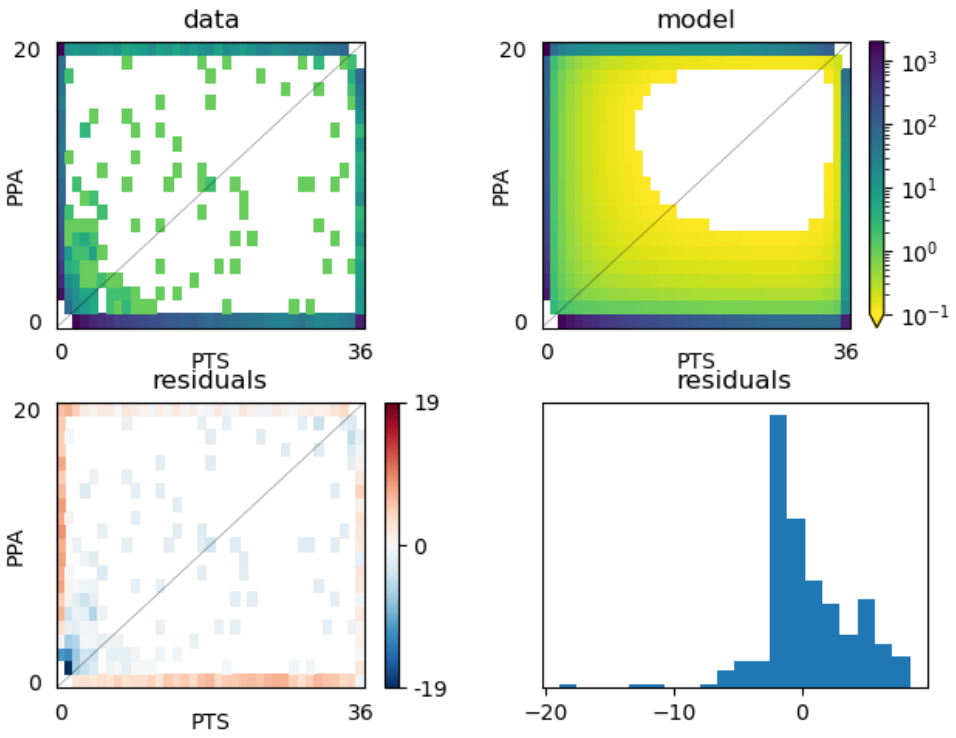

Fig. S89 Model fit to the joint AFS using non-synonymous SNPs from PPA and PTS. The upper left panel shows the observed joint AFS, the upper right panel shows the inferred AFS based on the maximum likelihood estimates in Fig. 3 and Additional File 2: Table S89, and the remaining panels show the residuals between the observed and model AFS.

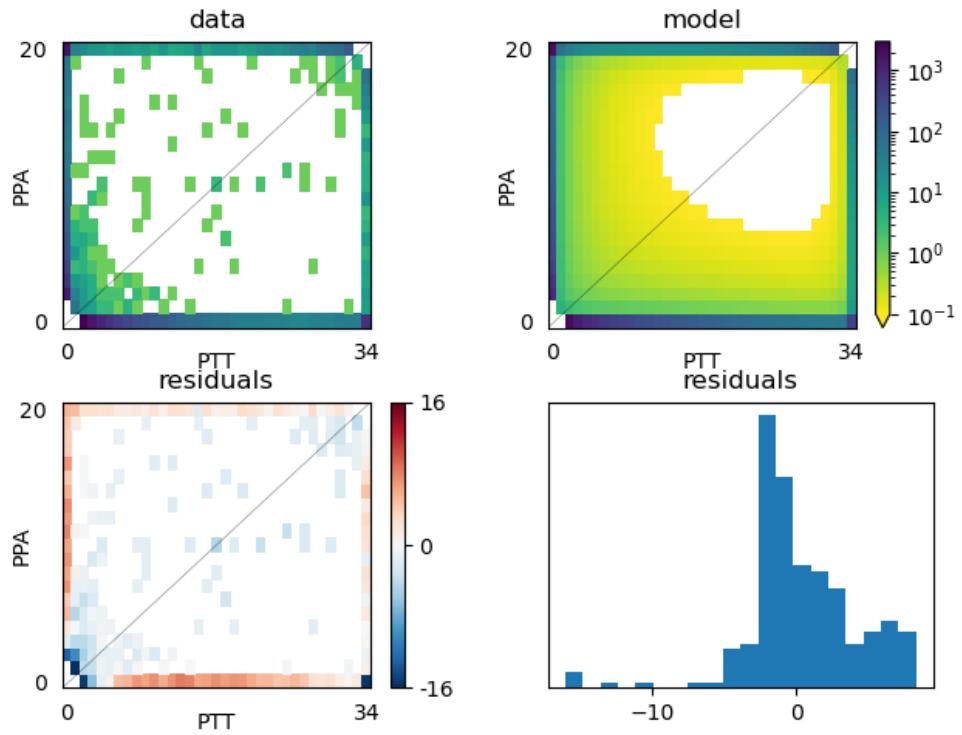

Fig. S90 Model fit to the joint AFS using non-synonymous SNPs from PPA and PTT. The upper left panel shows the observed joint AFS, the upper right panel shows the inferred AFS based on the maximum likelihood estimates in Fig. 3 and Additional File 2: Table S89, and the remaining panels show the residuals between the observed and model AFS.

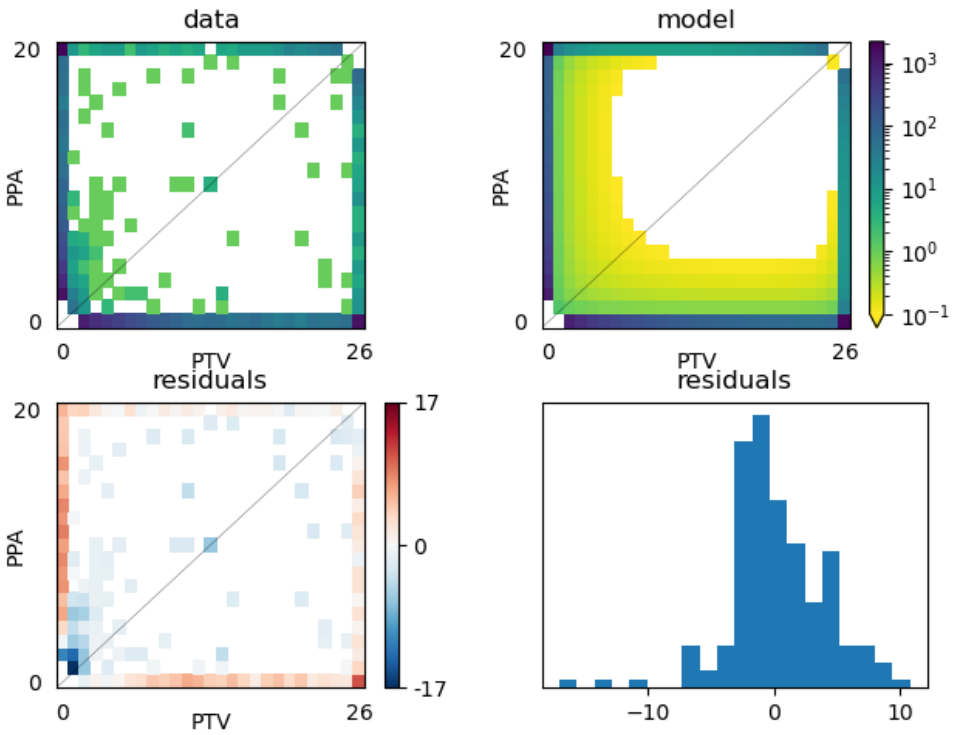

Fig. S91 Model fit to the joint AFS using non-synonymous SNPs from PPA and PTV. The upper left panel shows the observed joint AFS, the upper right panel shows the inferred AFS based on the maximum likelihood estimates in Fig. 3 and Additional File 2: Table S89, and the remaining panels show the residuals between the observed and model AFS.

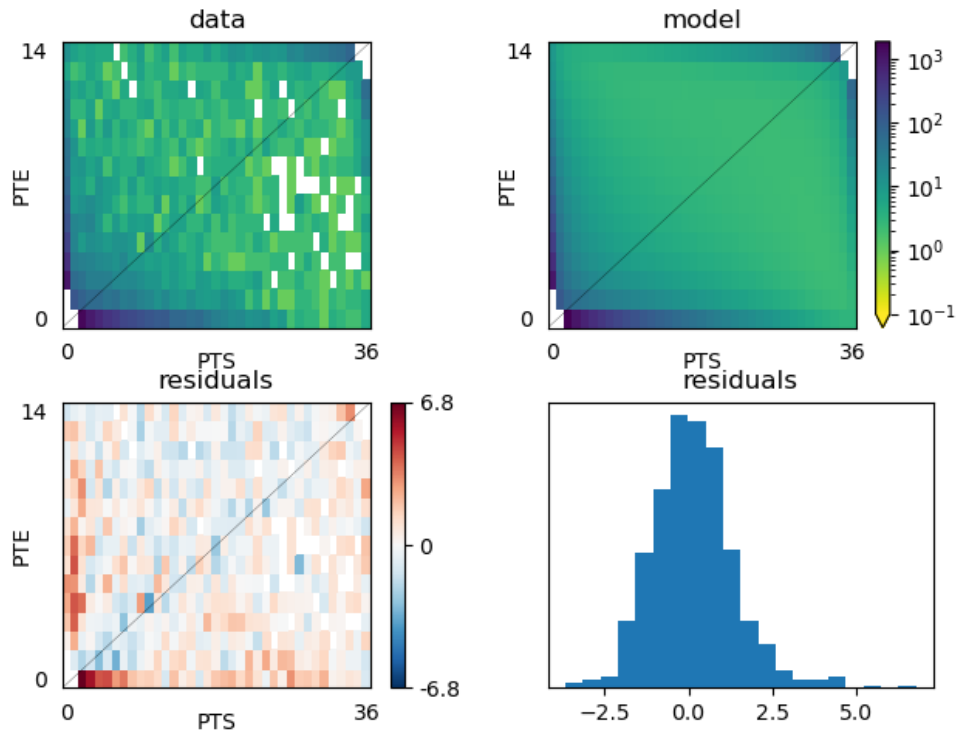

Fig. S92 Model fit to the joint AFS using non-synonymous SNPs from PTE and PTS. The upper left panel shows the observed joint AFS, the upper right panel shows the inferred AFS based on the maximum likelihood estimates in Fig. 3 and Additional File 2: Table S89, and the remaining panels show the residuals between the observed and model AFS.

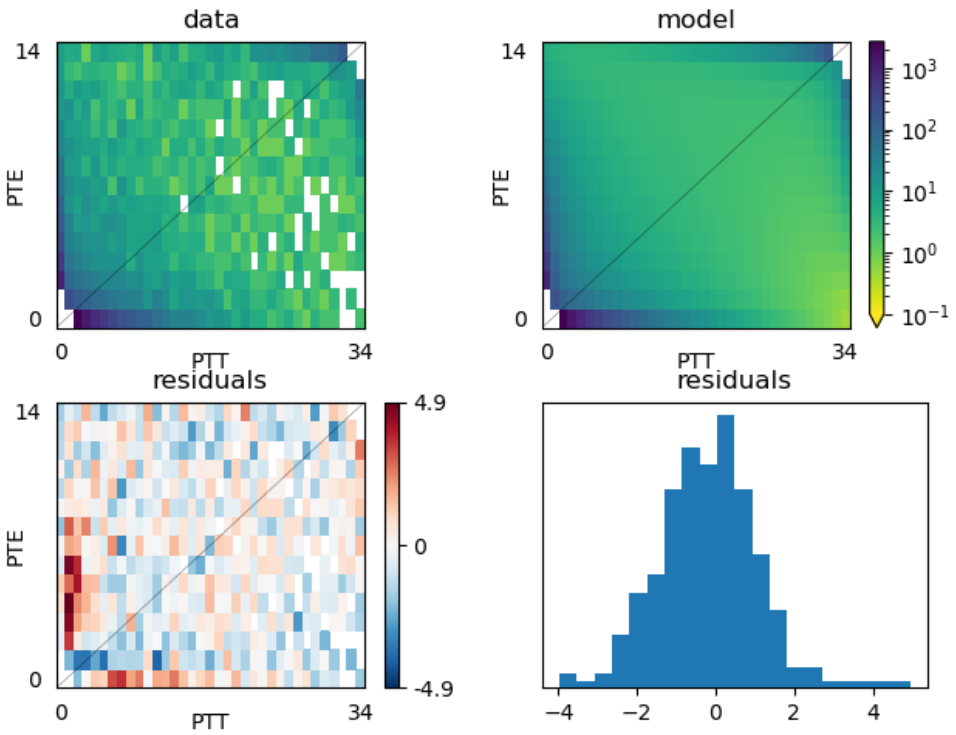

Fig. S93 Model fit to the joint AFS using non-synonymous SNPs from PTE and PTT. The upper left panel shows the observed joint AFS, the upper right panel shows the inferred AFS based on the maximum likelihood estimates in Fig. 3 and Additional File 2: Table S89, and the remaining panels show the residuals between the observed and model AFS.

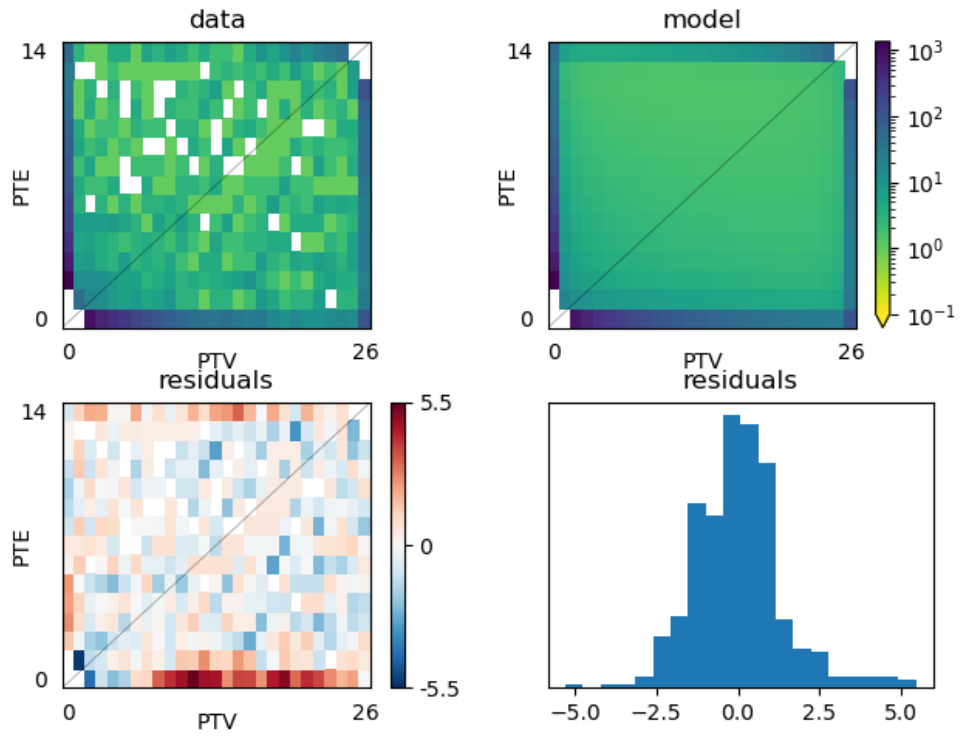

Fig. S94 Model fit to the joint AFS using non-synonymous SNPs from PTE and PTV. The upper left panel shows the observed joint AFS, the upper right panel shows the inferred AFS based on the maximum likelihood estimates in Fig. 3 and Additional File 2: Table S89, and the remaining panels show the residuals between the observed and model AFS.

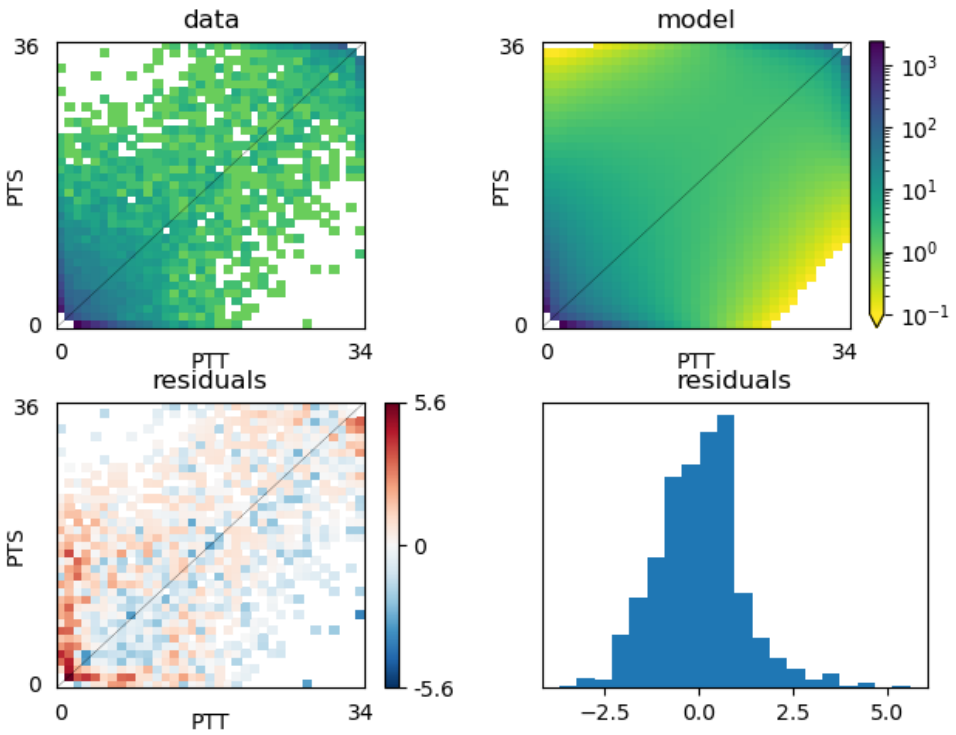

Fig. S95 Model fit to the joint AFS using non-synonymous SNPs from PTS and PTT. The upper left panel shows the observed joint AFS, the upper right panel shows the inferred AFS based on the maximum likelihood estimates in Fig. 3 and Additional File 2: Table S89, and the remaining panels show the residuals between the observed and model AFS.

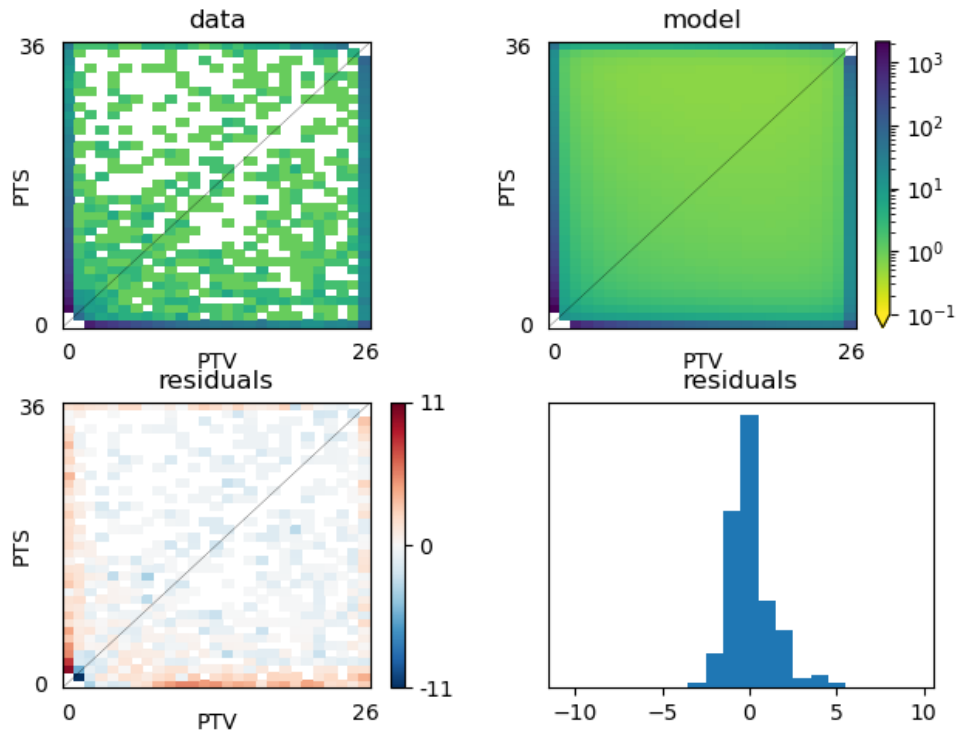

Fig. S96 Model fit to the joint AFS using non-synonymous SNPs from PTS and PTV. The upper left panel shows the observed joint AFS, the upper right panel shows the inferred AFS based on the maximum likelihood estimates in Fig. 3 and Additional File 2: Table S89, and the remaining panels show the residuals between the observed and model AFS.

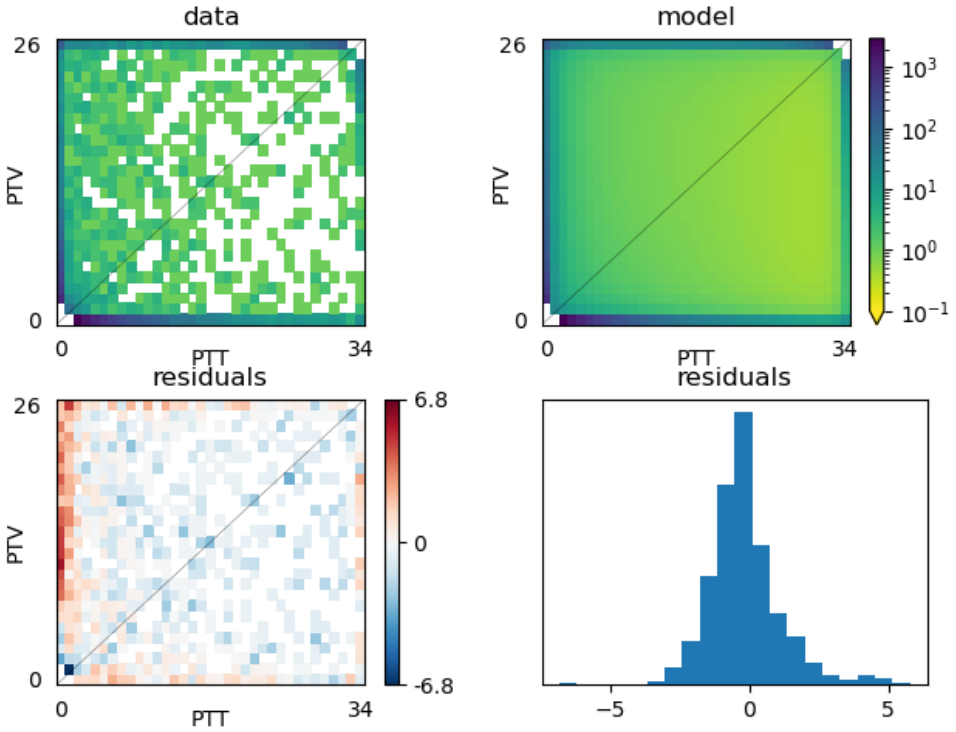

Fig. S97 Model fit to the joint AFS using non-synonymous SNPs from PTT and PTV. The upper left panel shows the observed joint AFS, the upper right panel shows the inferred AFS based on the maximum likelihood estimates in Fig. 3 and Additional File 2: Table S89, and the remaining panels show the residuals between the observed and model AFS.

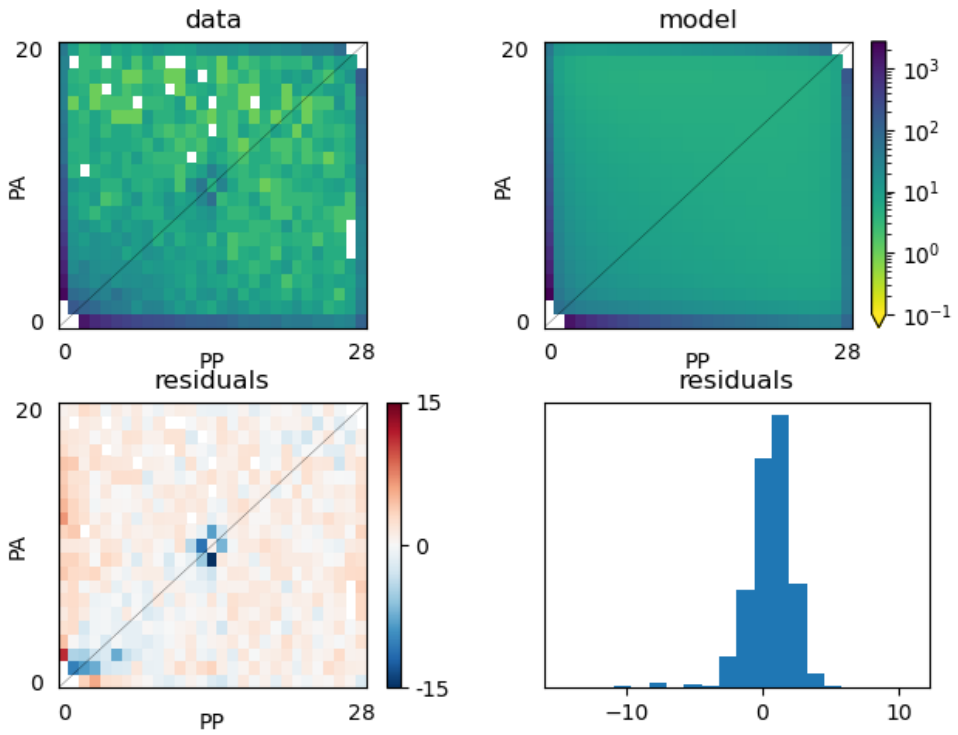

Fig. S98 Model fit to the joint AFS using non-synonymous SNPs from PA and PP. The upper left panel shows the observed joint AFS, the upper right panel shows the inferred AFS based on the maximum likelihood estimates in Fig. 3 and Additional File 2: Table S89, and the remaining panels show the residuals between the observed and model AFS.

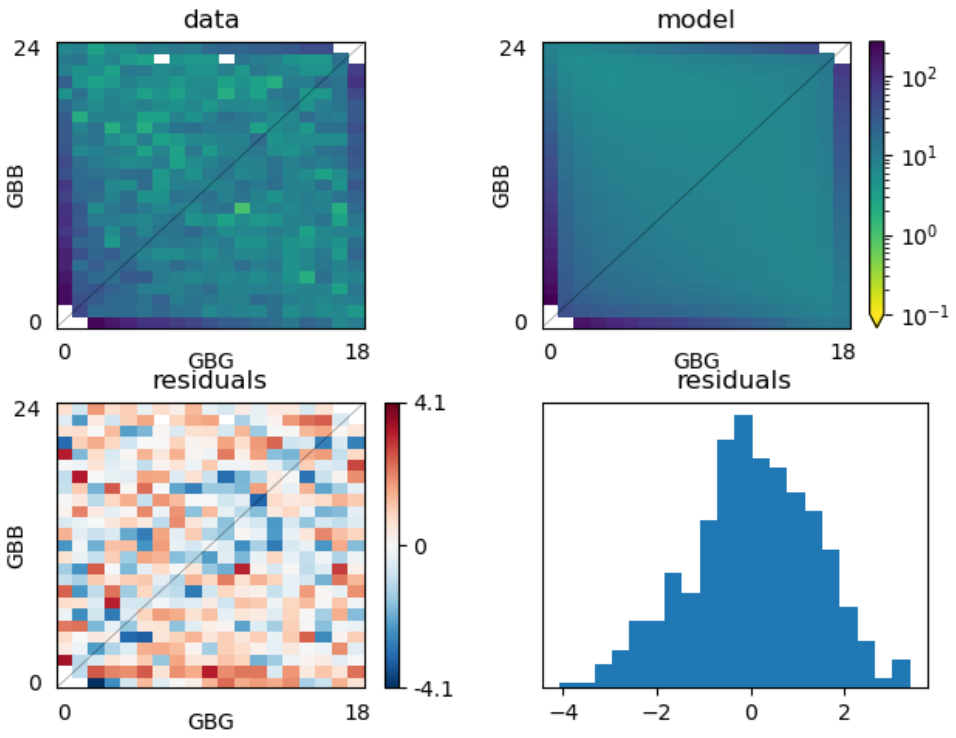

Fig. S99 Model fit to the joint AFS using non-synonymous SNPs from GBB and GBG. The upper left panel shows the observed joint AFS, the upper right panel shows the inferred AFS based on the maximum likelihood estimates in Fig. 3 and Additional File 2: Table S89, and the remaining panels show the residuals between the observed and model AFS.

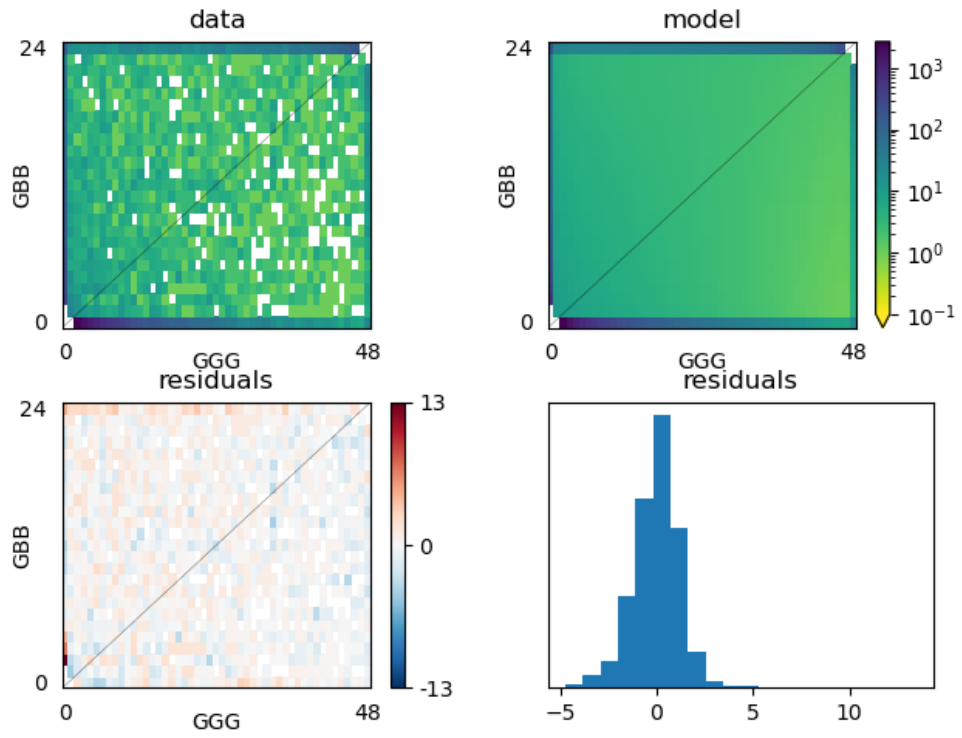

Fig. S100 Model fit to the joint AFS using non-synonymous SNPs from GBB and GBG. The upper left panel shows the observed joint AFS, the upper right panel shows the inferred AFS based on the maximum likelihood estimates in Fig. 3 and Additional File 2: Table S89, and the remaining panels show the residuals between the observed and model AFS.

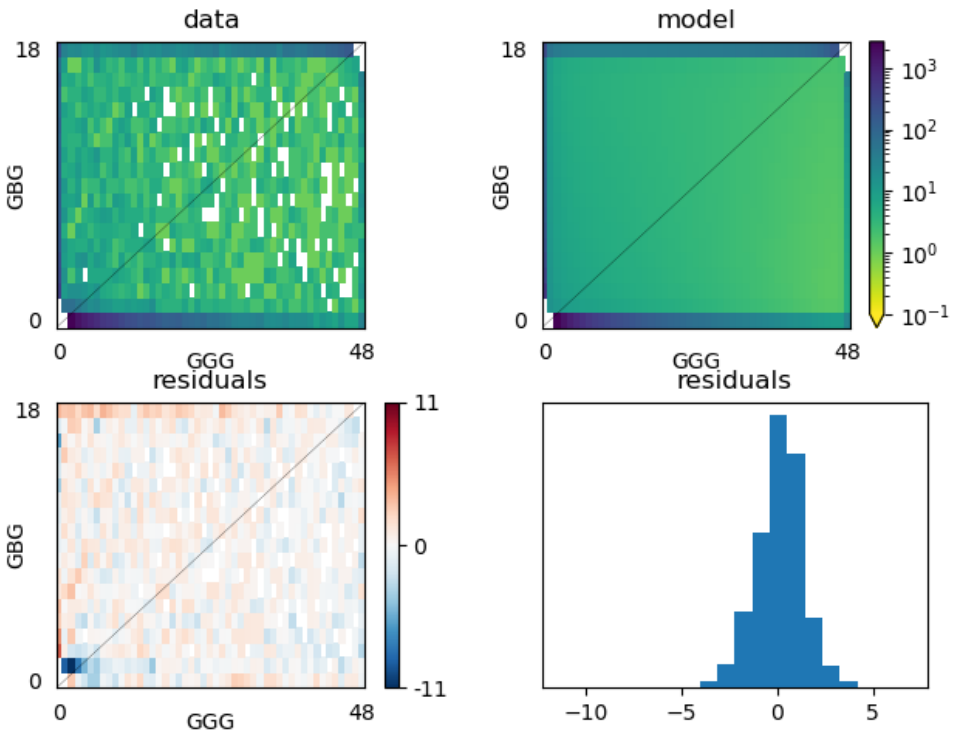

Fig. S101 Model fit to the joint AFS using non-synonymous SNPs from GBB and GBG. The upper left panel shows the observed joint AFS, the upper right panel shows the inferred AFS based on the maximum likelihood estimates in Fig. 3 and Additional File 2: Table S89, and the remaining panels show the residuals between the observed and model AFS.

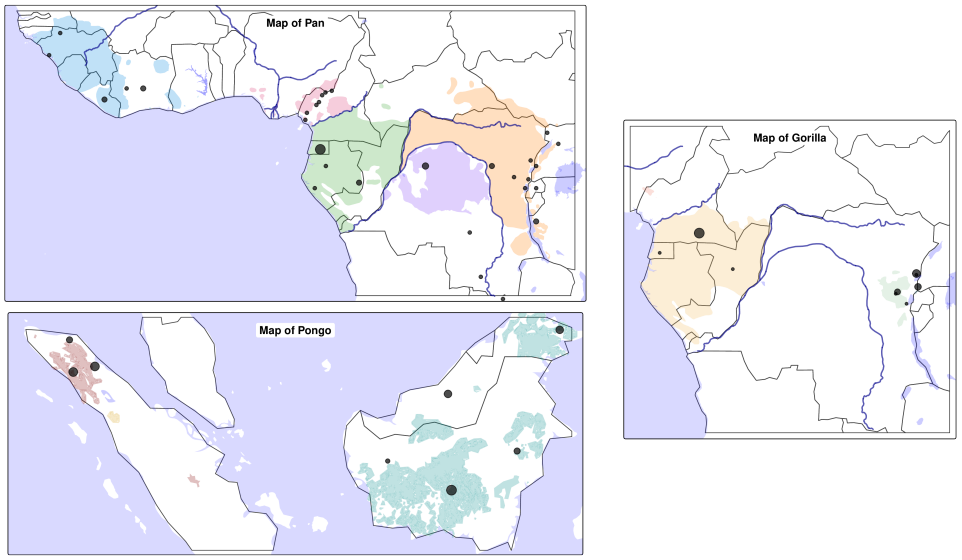

Fig. S102 Geographic origin of samples included in this study, as far as known from the original studies, stratified by *Pan*, *Gorilla* and *Pongo*. Spatial distribution ranges obtained from IUCN (International Union for Conservation of Nature). *Pan* populations: blue, western chimpanzee (PTV, *Pan troglodytes verus*); red, Nigeria-Cameroon chimpanzee (PTE, *Pan troglodytes ellioti*); green, central chimpanzee (PTT, *Pan troglodytes troglodytes*); orange, eastern chimpanzee (PTS, *Pan troglodytes schweinfurthii*); purple, bonobo (PPA, *Pan paniscus*). *Gorilla* populations: red, Cross-River gorilla (not included in this study, *Gorilla gorilla diehli*); yellow, western lowland gorilla (GGG, *Gorilla gorilla gorilla*); green, eastern lowland gorilla (GBG, *Gorilla beringei graueri*); blue, mountain gorilla (GBB, *Gorilla beringei beringei*). *Pongo* populations: red, Sumatran orangutan (PA, *Pongo abelii*); yellow, Tapanuli orangutan (not included in this study, *Pongo tapanuliensis*); turquoise, Bornean orangutan (PP, *Pongo pygmaeus*). Dot size corresponds to number of individuals at a given locality.